THE UNIVERSITY OF CALGARY

Glacial Isostatic Adjustment of Laterally Homogeneous vs. Heterogeneous Earth Models

by

Zhihong Ni

A DISSERTATION

SUBMITTED TO THE FACULTY OF GRADUATE STUDIES

IN PARTIAL FULFILMENT OF THE REQUIREMENTS FOR THE

DEGREE OF DOCTOR OF PHILOSOPHY

DEPARTMENT OF GEOLOGY AND GEOPHYSICS

CALGARY, ALBERTA

JANUARY, 1998

ABSTRACT

The effects on postglacial rebound due to lateral variations in lithospheric thickness, asthenospheric viscosity and thickness, density, and lower mantle viscosity have been evaluated for Maxwell viscoelastic flat-earth models using the finite element method. Vertical displacement relative to the present sea level, which is comparable to relative sea level data (RSL) for the last 8 thousand years, is computed for both axisymmetric and three dimensional non-axisymmetric earth models with disk loads. This is then extended to a realistic three dimensional earth model with a realistic deglaciation history for North America. Vertical velocity, gravity, horizontal displacement and velocity are also computed for some of the axisymmetric models.

The results show that lateral heterogeneities introduce additional spatial variations to postglacial uplift of a laterally homogeneous reference earth model. The variations can be detected by comparing RSL with predictions of a suite of reference models at sites across a large area, excluding the inner peripheral area of former glacier margin because vertical motion in the area is least sensitive to the earth properties whereas horizontal motion is relatively more sensitive there. The effects of lateral variations in the asthenosphere are more detectable than those in the lithosphere. The effects of the lower mantle heterogeneities are significant for large ice loads with size comparable to the Laurentide Ice Sheet, but negligible for small ice loads with size comparable to or smaller than the Fennoscandia Ice Sheet. The effects of a low density continental root on RSL and horizontal motions are small, but detectable with gravity. The lateral heterogeneities under a formerly glaciated area affect the postglacial rebound more than those outside the area.

In addition, a 3D spherical finite element model has been constructed and calibrated using the spherical spectral method. Analytical solutions of some simple layered spherical earth models, derived for the calibration also, demonstrate that (1) a density contrast between two solid layers introduces a buoyancy mode and a contrast in the ratio of viscosity/(shear modulus) introduces two insignificant transitional modes, (2) neglecting self-gravitation results in a little faster relaxation at small n harmonics, (3) the singularities in the numerical search for the relaxation modes can be avoided easily.

ACKNOWLEDGMENTS

I thank Dr. Patrick Wu for his academic guidance and financial supports from his research grants. His insightful help and patience are greatly appreciated.

I am also in debt to my wife Li and daughter Ming. This program has taken a considerable part of my life away from them.

Thanks to Mr. Bryan Gooding and Dr. Douglas S. Phillips of the University Computing Services at the University of Calgary for their friendly and professional supports, to Wayne Glover, David Lewis, Paul Jackson, Brian Straub, and Shell Canada Limited for their support at the final stage of my thesis completion.

Financial supports from the University of Calgary in terms of Teaching and Research assistantships are gratefully acknowledged.

Supercomputing of the project is provided through HIGH PERFORMANCE COMPUTING SCHOLARSHIPS from the High Performance Computing and Fujitsu Scientific Commission and the University of Calgary.

TABLE OF CONTENTS

LIST OF TABLE

LIST OF FIGURES

CHAPTER 1

INTRODUCTION

During the last glacial maximum eighteen thousand years ago, many parts of the world, including Canada and Fennoscandia, were covered by huge ice sheets that were as thick as two or three kilometers. The land was downwarped a few hundreds of meters by the weight of the ice. As the ice sheets retreated, the land uplifts, which is called postglacial rebound. The aim of this thesis is to investigate the effects of lateral heterogeneities of earth properties on postglacial rebound.

1.1 POSTGLACIAL REBOUND: OBSERVATIONS, SIGNIFICANCE, AND MODELING

In formerly glaciated areas, the rebound has been marked by elevated ancient beaches. Heights and radio-isotope dates of the beaches provide relative sea level (RSL) history data that can be grouped into four categories (Walcott, 1972): (1) the RSL curves at sites in formerly glaciated areas (for example, Hudson Bay and the Gulf of Bothnia) that are characterized by continuous land emergence (Fig. 1.1a); (2) near the edge of the ice sheets at glacial maximum, RSL histories are characterized by initial emergence followed by submergence after about 10 thousand years before present (ka BP) (Fig. 1.1b); (3) in the near field outside the edge of the former ice sheets, RSL curves are characterized by continuous land submergence (Fig. 1.1c); (4) in the far field outside the edge of a former ice sheet, RSL curves are characterized by initial submergence followed by land emergence or submergence with no consistent postglacial rebound signature among all sites (Fig. 1.1d). The errors in RSL data come from those in height measurement (including uncertainty in modern average sea-level) and those in radio C^{14} dating technique (Pirazzoli, 1991).

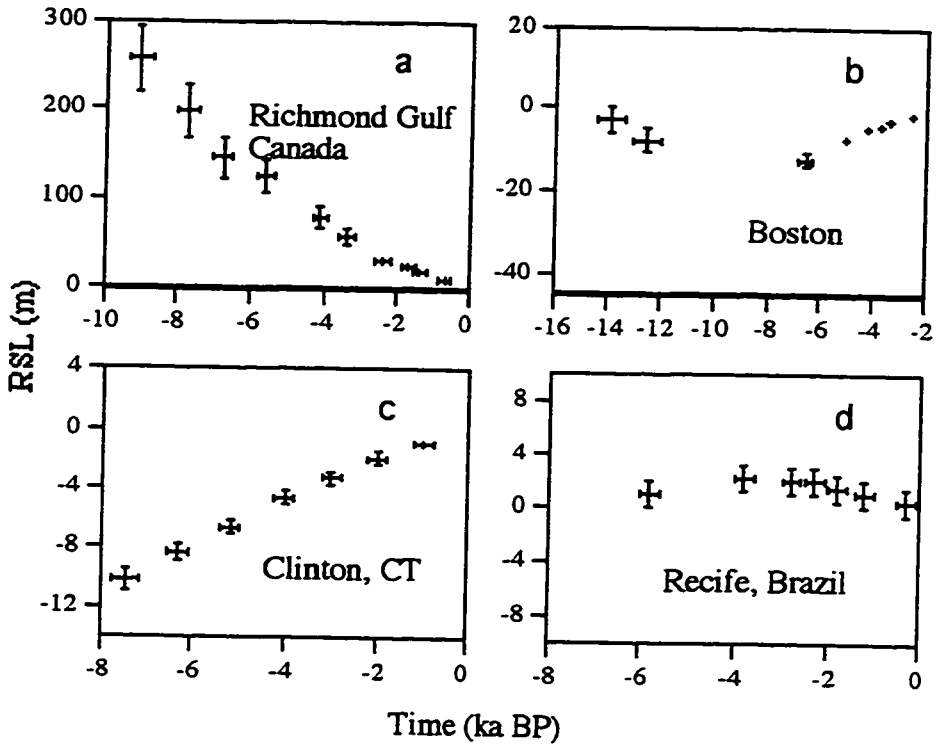

Figure 1.1 Examples of RSL data for each of the four categories. See text for detail. The crosses represent data with error bars.

In addition to land uplift, postglacial isostatic adjustment also affects the earth's shape, its gravity field, angular momentum, and stress field. The effects can contribute to measurements of VLBI (Mitrovica et al., 1993), gravity anomalies (Peltier & Wu, 1982; Wu & Peltier, 1983; Mitrovica & Peltier, 1989; Mitrovica & Peltier, 1991; Trupin et al., 1992; Wahr et al., 1993; Han & Wahr, 1995; Ekman & Mäkinen, 1996), secular variations in the earth's rotation rate and the position of the axis of rotation with respect to geography (Sabadini & Peltier, 1981; Sabadini et al., 1982; Peltier & Wu, 1983; Wu & Peltier, 1984; Peltier, 1988; Han & Wahr, 1989; Ricard et al., 1992; Trupin et al., 1992; Wahr et al., 1993; Trupin, 1993; Jiang & Peltier, 1994; Mitrovica & Forte, 1995; Mitrovica et al., 1997). High precision repeated gravity measurements, sea level records, and repeated leveling are used for monitoring current postglacial rebound in the formerly glaciated area (Ekman & Mäkinen, 1996). Tide gauge records of appropriately long duration can be used to extract current secular sea level trends (Peltier, 1988; Peltier & Tushingham, 1989; 1991; Trupin & Wahr, 1991; Mitrovica & Davis, 1995).

Observations of postglacial isostatic adjustment are often used to infer earth rheology as well as ice history. Earth rheological structure is critical for understanding mantle convection and plate tectonics. Ice history and sea level models provide boundary conditions for paleaoclimate and long-term environmental studies (Peltier & Tushingham, 1989; Peltier, 1988; 1994). Modeling glacial isostatic adjustment can also provide quantitative estimate of stress associated with the rebound that makes up an important part of the total stress in a formerly glaciated area. Knowledge of the stress can help us understand the causes of intraplate seismicity in deglaciated areas (Wu & Hasegawa, 1996a; b; Wu, 1997).

To model postglacial rebound, two inputs are needed - ice history and earth rheology. Usually, density and elastic properties of the earth models are taken from seismology (e.g. The Preliminary Reference Earth Model by Dziewonski & Anderson, 1981).

The first ice history model Ice-1 (Peltier & Andrews, 1976) was constructed with three kinds of data: ice margin history from radiocarbon dates of terminal moraines, ice profiles from equilibrium conditions of ice mass, and world sea-level changes which constrain the total ice volume change. The Ice-1 model gives ice thickness on a 5 by 5 degree grid for the Northern Hemisphere between 18 ka BP and 6 ka BP. A refined model (Ice-2 by Wu & Peltier, 1983) included the Antarctic ice component. This update also made use of RSL histories at 45 sites as well as the gravity anomaly. The use of more RSL data enhances knowledge of melting history of the ice sheets. The next ice model, Ice-3G, is further refined to approximately 2 by 2 degree resolution and in regions where RSL data is abundant to approximately 1 by 1 degree (Tushingham & Peltier, 1991) by using more RSL data. The most recent model Ice-4G includes the long sea level record in Barbados and allows the rising sea to transgress the continental margins (Peltier, 1994). Uncertainties in these ice models are due to (1) missing observations of ice limits in some areas (e.g. the Barents Sea) and (2) limited and unevenly distributed RSL observations, especially for the early stage of the deglaciation.

There are also uncertainties about earth rheology. It is not quite clear which creep mechanism is dominant in the mantle: Is it diffusion creep (Turcotte & Schubert, 1982; Ranalli & Fischer, 1984), dislocation creep (Minster & Anderson, 1981; Turcotte & Schubert, 1982; Poirier, 1985; Ranalli, 1987), or transient creep (Peltier et al. 1980; Sabadini et al., 1985; Peltier, 1986; Peltier et al, 1986; Yuen et al., 1986; Rümpker &

Wolf, 1996)? Some investigations have explored the effects of power-law rheology (Nakada, 1983; Post & Griggs, 1973; Karato & Wu, 1993; Wu, 1992a; 1993; 1995). Wu (1992a, 1993, 1995) and Karato & Wu (1993) have found that the rebound process basically 'sees' linear rheology in the mantle. Coincidentally, linear viscoelastic rheology has been used in most other studies on postglacial rebound due to its mathematical simplicity. Likewise, linear Maxwell rheology (Cathles, 1975) is adopted in this dissertation.

Earth models of linear rheology have evolved from simple non-self-gravitating, viscous, and flat earth models, such as thin channel models (Van Bemmelen & Berlage, 1935; Barrell, 1914) and the uniform halfspace model (Haskell, 1935), to more sophisticated self-gravitating, non-rotating, linear viscoelastic, and spherically layered earth models (e.g. O'Connell, 1971; Cathles, 1975; Peltier, 1974; 1976; Wu & Peltier, 1982; 1983; 1984; Wolf, 1987; Nakada & Lambeck, 1989; Lambeck et al., 1990; Tushingham & Peltier, 1991; Mitrovica & Peltier, 1993; Fjeldskaar, 1994). Recent models by Han & Wahr included effects of earth rotation (Han & Wahr, 1989; 1995) and anisotropy of mantle viscosity (Han & Wahr, 1997). However, all of these models ignored lateral heterogeneities by taking the earth as laterally homogenous which conflicts with recent seismic tomography results that reveal large scale lateral heterogeneities in the interior of the earth. Some recent studies on postglacial rebound began to explore the effects of lateral heterogeneities (Sabadini et. al, 1986; Gasperini & Sabadini, 1989; 1990; Gasperini et al., 1990; 1991; Kaufmann et al., 1997). In the following section, the evidences of lateral heterogeneities in earth properties and their implications on the earth's temperature and viscosity structure are briefly reviewed. This is then followed by a short survey on the studies of postglacial rebound with laterally heterogeneous earth models.

1.2 GEOPHYSICAL EVIDENCES FOR LATERAL HETEROGENEITIES

Topographic and geological contrasts, such as continents vs. oceans, orogenic belts vs. shields, and mid-ocean ridges vs. oceanic floors, clearly indicate lateral variations in earth properties. More importantly, these lateral contrasts are not just superficial, they are rooted deeply inside the earth as shown in global seismic tomography. The seismic velocity models from such inversions reveal three dimensional laterally heterogeneous structures of the earth's mantle with increasing spatial resolution.

The wavelength of lateral resolution of the earlier tomographic models (Dziewonski, 1984; Woodhouse & Dziewonski, 1984; Nataf et al., 1986; Tanimoto, 1986a; b) was around 5000 km, or equivalently, an angular order of six. Later models came with an improved lateral resolution of 1000 km (Wong, 1989; Zhang & Tanimoto, 1993) or included parameterization for anisotropy (Montagner & Tanimoto, 1990; 1991) or anelasticity (Romanowicz, 1990; Roult et al, 1990; Durek et al, 1993). Some of the recent models (Tanimoto, 1990a; b; Woodward & Masters, 1991a; b; Su & Dziewonski, 1991; 1992; Su et al., 1992) were inverted from SH body waves. Their radial resolution is more uniform than in previous models and their lateral resolution has also been improved - to about 3000 km, or to an angular degree of 12 (Su et al., 1994; Li & Romanowicz, 1996).

Most of these seismic velocity anomaly models, especially the recent ones agree with each other for the upper part of the mantle (down to 400 km depth) where they all correlate with surface tectonics: ridges are slow, shields are fast, and seismic velocities increase with the age of the seafloor. However, most of the anomalies decrease sharply as depth increases. Typically, the S wave velocity variation is about 4-5 % at shallow depth (100 - 200 km), and decreases to less than 1% at 440 km depth (Montagner & Tanimoto 1991). In the middle of the mantle between 400 and 1700 km, there is no clear pattern, and the power spectrum is almost flat. These lateral velocity variations can be due to lateral variations in temperature, thereby can be indicative of lateral variations in viscosity as estimated in the following subsections.

1.2.1 Estimation of Maximum Lateral Temperature Changes

Although seismic velocity anomalies can be due to variations in either or both of chemical composition and temperature, here we estimate the maximum temperature variation by ignoring changes in chemical composition. The maximum lateral temperature (T) variation implied by the velocity anomalies can then be estimated according to the following relationship (Estey & Douglas, 1986) for pyrolite:

$$\frac{1}{V_s}\left(\frac{\partial V_s}{\partial T}\right) = -7.5 \times 10^{-5} / {}^{\circ}C \qquad (1.1)$$

Thus, 1% variation in S wave velocity translates into a temperature variation of 133 $^{\circ}$K and 5% corresponds to 666 $^{\circ}$K.

Larger temperature contrasts have been estimated from regional temperature profiles by Tralli & Ita (1994). Since both P and S wave anomalies in the upper 400 km are consistent with surface geology, they established a characteristic seismic parameter profile for each of the seven geological regions: (1) Young oceans (<25 ma), (2) Intermediate-age oceans (25-100 ma), (3) Old oceans (>100 ma), (4) Active continental margins, (5) Platforms, (6) Shields, and (7) Trenches. The temperature profile for each of the regions has then been inverted by solving the differential relationship among seismic parameters ϕ, temperature T, bulk modulus K, and density ρ, iteratively:

$$\phi - \phi_0 = \frac{1}{\rho}\left(\frac{dK}{dT} - \phi_0 \frac{d\rho}{dT}\right)(T - T_0) \qquad (1.2).$$

Comparing their (Tralli & Ita, 1994) temperature profiles for intermediate-age oceans (analogy to North-Western Atlantic) and shields (analogy to Canadian shield) at depth interval between 270 to 370 km, the average difference is estimated to be about 900 °K (2300 - 1400 °K).

1.2.2 Estimation of Maximum Viscosity Change

Lateral temperature contrasts can result in lateral viscosity variations as viscosity is a strong function of temperature (T) (Karato & Wu, 1993):

$$v = A\exp\left(\frac{E_a + pV_a}{RT}\right) \qquad (1.3)$$

Here A is a coefficient which is a weak function of T (and can be regarded as independent from T); E_a is the activation energy; V_a is the activation volume; p is the pressure; and R is the gas constant. For dry olivine, E_a=300 KJ/mol and $V_a = 6\times10^{-6}$ m^3/mol (Karato & Wu, 1993). An estimate of p=9.4 GPa can be obtained from ρgh by taking ρ=3200 kg/m^3, g=9.8 m/s^2, and h=300 km. Since pV_a=56.4 kJ/mol is only about 19% of the value of E_a, variations of pressure can be neglected for simplicity. With these values, eq. 1.3 yields a mantle viscosity drop to about one fifth of that at 1500 °K for a 100°K increase. For a 600 degree increase from 1500 °K, the viscosity drops to about two ten-thousandth of that at 1500 °K.

For the average temperature contrast between the intermediate-age oceans (2300 °K) and shields (1400 °K) in depth interval between 270 to 370 km, as estimated from to the

temperature profiles inverted by Tralli & Ita (1994), the maximum viscosity contrast can reach 5 orders of magnitude.

1.3 PREVIOUS STUDIES ON THE EFFECTS OF LATERAL HETEROGENEITIES

The possibility of lateral variation of a few orders of magnitude in upper mantle viscosity raises two questions: (1) can such lateral heterogeneities be detected using postglacial rebound data? and (2) what are the effects of lateral heterogeneities on postglacial rebound? To detect lateral heterogeneities in the upper mantle under the continental margin in North Europe, a suite of laterally homogeneous earth models was used to predict and match RSL data at a series of localities near the formerly glaciated area (Breuer & Wolf, 1995; Kaufmann & Wolf, 1996). They found that RSL histories at different locations can be fitted by different laterally homogeneous earth models that have distinctly different upper mantle viscosity and/or lithospheric thickness.

Breuer & Wolf (1995) studied RSL data at a group of islands in Svalbard Archipelago near the northern European continental margin and concluded that lithospheric thickness and asthenospheric viscosity increase towards the Eurasian continent. This was later confirmed by Kaufmann & Wolf (1996) with land emergence data in the northern Barents Sea using the high-resolution ice model BARENTS-2 and the RSL observations from 25 locations. They claimed that postglacial land emergence can in fact resolve lateral variations in asthenospheric viscosity.

Nakada & Lambeck (1989) compared differential sea-levels with computed RSL for laterally homogeneous earth models along the shores of large gulfs and bays of Australia and islands in the Pacific ocean. They inferred that viscosity in the upper mantle increases towards the Australian continent.

However, the validity of using this comparative method to detect lateral heterogeneities is questioned by Kaufmann et al. (1997), who showed that laterally homogeneous models that fit RSL data at a given location may not always reflect the true rheology beneath the location for a laterally heterogeneous earth.

To address the second question regarding the effects of lateral heterogeneities, Sabadini et al. (1986) and Gasperini et al. (1990) used finite element computations to investigate the effects of a laterally heterogeneous upper mantle on postglacial rebound and found that displacements in the central area of an ice sheet are not influenced by lateral variations in lithospheric thickness and asthenospheric viscosity. On contrast, vertical displacement, and both vertical and horizontal displacement velocities near the edge of the ice load are sensitive to lateral heterogeneities in the upper mantle (Gasperini et al., 1990). Deformation around the peripheral bulge can still be affected by an asthenosphere twenty-five degrees away (Sabadini et al., 1986).

Effects of lateral viscosity variation in the whole mantle were also studied by Gasperini and Sabadini (1989, 1990) mainly from a spectral perspective, although the FE method was used. In their models, the logarithm of the viscosity, that reflects the exponential dependence of the viscosity on temperature, changes sinusoidally in the lateral direction. They concluded that postglacial rebound at the center of former ice sheet is sensitive to long wavelength change of viscosity while that at edge is sensitive to the short wavelength variations. However, this kind of spectral approach can be misleading because it tends to ignore effects of different spatial phase relationship between the ice sheet and the lateral heterogeneities which can be just as important as the wavelength.

Effects of deep continental roots, simulated with thick lithosphere sitting on high viscosity mantle, were modeled using the finite element method and were found to be significant (Gasperini & Sabadini, 1989; 1990; Gasperini et al., 1991): vertical displacement and velocity field can be affected by 30% in the center of deglaciated areas. Horizontal displacements, strain fields, and vertical velocity at the peripheral region are also very sensitive to the prescribed lateral heterogeneities.

Kaufmann et al. (1997) did more modeling on the effects of lateral heterogeneities in the upper mantle. They have shown that comparison of predictions of a set of laterally homogeneous models with RSL data can only establish lateral heterogeneities qualitatively for a known continental margin but does not necessarily produce correct values of lithospheric thickness or asthenospheric viscosity. They concluded that "lateral heterogeneities are most easily detected around the load margin and in the forebulge area" (p. 186, Kaufmann et al., 1997).

Nevertheless, the models that have been completed so far are preliminary. For example, only ice loads with sizes comparable to the Fennoscandian Ice Sheet have been considered, and most investigations focus on the effects of lateral heterogeneity in the upper 400 km of the mantle. The effects of lateral viscosity variations in the lower mantle need to be investigated with different size of loads. Further, the effects of lateral variations in density have never been explored. Density has been taken laterally homogeneous in most of the investigations. This needs to be justified in terms of effects of lateral density variations on postglacial rebound.

Furthermore, conclusions are typically based on very few earth models and simple Heaviside deglaciation histories which deglaciation is completed instantly, except Kaufmann et al.(1997). This presents a risk in generalization of the conclusions because validity of such forward modeling results is dependent on a large number and wide range of models. Results from the few models give little hints about non-uniqueness - that is whether different earth models may produce similar results. Besides, realistic ice history should be considered.

In fact, all of these models are based on axisymmetric geometry (Sabadini et. al, 1986; Gasperini & Sabadini, 1989; 1990; Gasperini et al., 1990; 1991; Kaufmann et al., 1997). In an axisymmetric earth model, both the ice sheet and earth properties have to be not only axisymmetric but also positioned concentrically. This imposes a strong constraint on the models and as a result, conclusions on the effects of lateral heterogeneities may be limited by what the axisymmetric models can offer. For instance, effects of lateral heterogeneities in an axisymmetric model are often overwhelmed by effects of lateral termination of the ice sheet. It is difficult to isolate and recognize spatial patterns of postglacial rebound due to lateral heterogeneities.

1.4 OBJECTIVES AND ACHIEVEMENTS

The main aim of this dissertation is to investigate the effects of lateral heterogeneities in earth properties on postglacial rebound. Specifically, I wish to:

(1) test the validity of using the finite element method in modeling postglacial rebound (chapter two);

(2) investigate the effects of lateral heterogeneities in asthenosphere and lithosphere on postglacial rebound observations, such as relative sea-level, land uplift rates, horizontal motions and gravity anomalies (chapter three);

(3) explore the effects of lateral viscosity variations in the lower mantle and the effects of lateral density variations on postglacial rebound (chapter four);

(4) evaluate the effects for three dimensional non-axisymmetric models with a realistic ice load as well as a hypothetical disk load (chapter five);

(5) apply the finite element method to a spherical earth model (chapter seven).

To calibrate the finite element model for a spherical earth, analytical solutions for postglacial rebound of some simple laterally homogeneous spherical earth models have been derived using the spectral method. Consequently, some important issues on postglacial rebound of spherically stratified earth are investigated, such as effects of neglecting self-gravitation, the singularity problem in numerical search for eigenvalues of gravitational relaxation modes, and relationships between gravitational relaxation modes and physical property contrasts of the layers (chapter six).

As an introduction, table 1.1 is a short list of achievements of this dissertation in comparison with previous investigations. Detail is given in the rest chapters.

Table 1.1 Previous Investigations and this Dissertation Achievements

Previous Investigations	This Investigation
On postglacial rebound of laterally heterogeneous earth models	
Used axisymmetric earth models.	Expanded to 3D non-axisymmetric models.
Ignored lateral density variations.	Evaluated the effects of lateral density variations.
Mostly focused on lateral heterogeneity in the upper 400 km of the earth.	Considered lateral heterogeneity in the lower mantle.
Used only one size of ice loads (comparable to the Fennoscandian Ice Sheet).	Considered two sizes of ice loads (comparable to the Fennoscandian and Laurentide Ice Sheets, respectively).
Used only simple Heaviside deglaciation and sawtooth ice histories.	Considered realistic ice history.
Used flat earth finite element models.	Applied the finite element method to a 3D spherical earth model and calibrated the model with the spherical spectral method.
On postglacial rebound of laterally homogeneous earth models	
Numerically inferred that a density contrast between two solid layers introduces a buoyancy mode and a contrast in either of viscosity or shear modulus introduces two insignificant transitional modes .	Analytically demonstrated that a density contrast between two solid layers introduces a buoyancy mode and a contrast in the ratio of viscosity/(shear modulus) introduces two insignificant transitional modes.
Re-invented an integral transformation to replace the Laplace transformation to avoid the singularities in the numerical search for the relaxation modes.	Found a normalized determinant function that is singularity free for numerical search for the relaxation modes.

1.5 METHODS

There are two methods that are used for modeling postglacial rebound: the spectral method and the finite element method.

The spectral method computes postglacial rebound in wavelength and Laplace transform domain, then inverts back to the spatial and time domain (Peltier, 1974; Wu & Peltier, 1982). It is used and detailed in chapter six for computing spherically stratified earth models. This method is mainly suitable for laterally homogeneous earth models.

For a laterally heterogeneous earth model, using the spectral method can be complicated because of cross-coupling among the harmonics: A harmonic load may excite more than that one harmonic deformation in a laterally heterogeneous earth whereas one harmonic load only excites the same harmonic deformation for a laterally homogeneous earth model. However, for lateral variations of viscosity within one order of magnitude, the spectral method can still be applied. For example, Richards and Hager (1989) considered flat earth models with long wavelength lateral variations of viscosity that are spatially in phase with the forcing load distribution. Another example is an axisymmetric craton whose viscosity is five times that of the background and located right beneath an axisymmetric load (D'Agostino et al., 1997).

However, if the viscosity varies laterally by a few orders of magnitude and if the lateral variation is not spatially in phase with the load, then the finite element method is more useful. That is why most published papers use it to model postglacial rebound of a laterally heterogeneous earth.

In this dissertation, a commercial finite element package, called Abaqus (1996), is used extensively for modeling laterally homogenous and heterogeneous models. The finite element method, its optimization, and verification are discussed in the next chapter.

CHAPTER 2

USING THE FINITE ELEMENT METHOD TO MODEL POSTGLACIAL REBOUND

In this chapter, the finite element method is briefly reviewed. This is then followed by a discussion on grid optimization and verification. The chapter also introduces the different kinds of finite element models that are used to explore the effects of lateral heterogeneities in the next three chapters: namely axisymmetric flat-earth models and three dimensional non-axisymmetric flat-earth models.

Flat earth models have been demonstrated to be adequate in describing the postglacial rebound process for a load with size smaller than or comparable to the Fennoscandian ice sheet (Wolf, 1984). For ice sheets with size comparable to the Laurentide ice sheet, Amelung & Wolf (1994) showed that one may still use flat earth models with constant gravity because effects due to curvature of the earth and perturbation potential of gravity tend to cancel out each other. Recently, Wu and Johnston (1998) demonstrated that finite element flat-earth models are adequate for modeling RSL in North America.

2.1 THE FINITE ELEMENT METHOD

The finite element method is well known for approximating deformation problems of all kinds. The basic principles and computational implementation can be found in many textbooks (e.g. Zienkiewicz & Taylor, 1989). Here, the method is only briefly summarized in an intuitive way. The emphasis is on its application to modeling postglacial rebound.

For the deformation of a non-self-gravitating half-space under a surface load, the equation of equilibrium for the incompressible and prestressed earth is (Cathles, 1975):

$$\nabla \cdot \boldsymbol{\tau} - \rho_o \nabla(g_o \mu) = 0 \qquad (2.1)$$

where ρ_o and g_o are the undisturbed density and gravity, respectively; and τ and u are perturbations in stress and vertical displacement, respectively. The term $-\rho_o \nabla(g_o u)$ represents the advection of prestress.

The finite element method finds a numerical approximation to the true solution of eq. 2.1. While the true solution is defined on a continuum of half-space, the approximate solution is defined on a limited number of closely packed finite elements. Within each element, material properties are assumed to be homogeneous and spatial variation of displacement can be interpolated from nodal displacement using simple shaping functions. An intuitive way of formulating and solving the problem is through the use of the principle of virtual work.

Supposing there were an arbitrarily small virtual displacement in the system, the principle of virtual work states that the virtual work done by external forces equals to the virtual work done by internal stress. Because the variations of displacement within each element are given by the shaping functions, the application of the principle yields a system of linear equations in terms of displacements at the nodes (**U**), nodal forces (**F**), and stiffness matrix (**K**):

$$\mathbf{KU} = \mathbf{F} \qquad (2.2).$$

The nodal forces are dependent on external forces and element geometry, and can be expressed by the integral of the forces over the elements. The stiffness matrix is dependent on and computed with element geometry, material properties, and the finite element shaping functions. The shaping functions used in this thesis are usually linear functions, except for chapter 7 where second order polynomials are used for spherical models. At some nodes, displacements are constrained by the boundary conditions while at other nodes the nodal forces are constrained. The solution of eq. 2.2 yields displacements at all the nodes. The displacement at any arbitrary location can then be obtained by interpolation using the shaping functions.

The key to obtaining a good result from a finite element computation is discretization. To approximate a viscoelastic half-space, the spatial extent of the finite element grid should be large enough so that any boundary condition will not affect the results very much. This is particularly important for viscoelastic material because its elastic displacement does not decay very fast with increasing distance from the load center. The dimensions of elements should be small enough so that displacements inside each element can be adequately

approximated with the shaping functions. However, it is computationally expensive to fill the whole model with small elements. The elements should be fine at places where large variations of deformation are expected and coarse at other places.

2.2 THE 2D FINITE ELEMENT GRID OPTIMIZATION

Extensive tests have been done for optimizing the finite element grids. Factors that have to be taken into consideration are types and number of elements, lateral and vertical extent of a grid, aspect ratio of an element, vertical and horizontal variation of element size, and boundary conditions. In the following, a viscoelastic half-space is taken as an example to illustrate the grid optimization and verification. Viscosity, shear modulus, Poisson's ratio, and density of the half-space are 10^{21} Pa-s, 1.45×10^{11} Pa, 0.5, and 3380 kg/m3, respectively. A circular disk load with uniform ice thickness of 2500 m and radius of 800 km is left on the surface of the halfspace at time t = 0. (This kind of loading history is referred as the Heaviside loading event). A cylindrical coordinate system with 4-node cylindrical finite elements are used. A element is a circular ring with a rectangular cross section whose four corners are defined by the four nodes on a vertical plane. The horizontal displacements along the axis of symmetry are constrained to be zero. Computationally, this kind of models is treated as 2D finite element models . For this reason they will be referred to as the 2D models to differentiate from other 3D models. The 2D model uses much less computer resources than a normal 3D finite element model covering a similar area, so it is economic to run and yet still a special kind of three dimensional model.

2.2.1 Effects of Radial Extent and Dimensions of Elements

Because the only variation in the model is the horizontal termination of the load, it is expected that radial dimension of each element and total radial extent of the elements are more critical than those in the vertical direction. Four kinds of finite element grids are tested for optimization of radial grid: (1) grid with small radial extent and elements with small radial dimension, (2) grid with large radial extent and elements with large radial dimension, (3) grid with large radial extent and elements with varying radial dimension, (4) grid as described in case (3) plus additional infinite boundary elements. All grids share the same number of regular elements in both radial (40) and vertical direction (15 elements

extending from the surface to 5500 km depth). For verification, vertical displacements computed with these grids are compared to those computed by the spectral method using Hankel transformation. The test results, as detailed in the following paragraphs, show that grid (4) is the optimal one whose results best agree with the spectral method.

The first grid tested has a uniform fine radial resolution of 50 km and small radial extent from r=0 to r=2000 km, or 2.5 times the load radius. The nodes at the bottom of the grid are fixed in space, and those at r=2000 km are fixed in the radial direction but free to move vertically. This latter boundary condition is known to give better approximation to the infinite halfspace than a fixed boundary condition there. The vertical displacements computed by the finite element model are plotted in figure 2.1a (symbols) and are compared with those computed by the spectral method (lines) for time t=0 (elastic deformation), 2 ka, 4 ka, and 8 ka after loading. The comparison shows that the results of this finite element model (symbols) are quite different from that of the spectral method (lines). The amplitude of displacement computed by the finite element model is smaller than those by the spectral method inside the load area, but is larger outside the load area. As we shall see, this is due to the fact that the finite element model does not extend far enough in the radial direction.

Next, we increase the radial extent to 8000 km by increasing the radial dimension of each element to 200 km while maintaining the same number of grid points. The result of this coarse grid (symbols in Fig. 2.1b) are much closer to those by the spectral method (lines). But, within and around the load area, the grid is a little too coarse to capture the curvature of the displacement curves. Conversely, in the far field where displacement curves are almost flat, there is no need to have so many elements. A better way is to use a non-uniform grid that is finer inside and near the load area, and coarser in far field (farther than r = 1700 km). The results of such a non-uniform grid mimic the results of the spectral method beautifully as shown in Fig. 2.1c, except for one minor detail. The amplitude of displacement computed by this finite element model is slightly smaller than that by the spectral method inside the load area, and is slightly larger outside the load area. This is similar to that in panel a, though with much reduced magnitude, which suggests that 8000 km is still not far enough. The finite element model

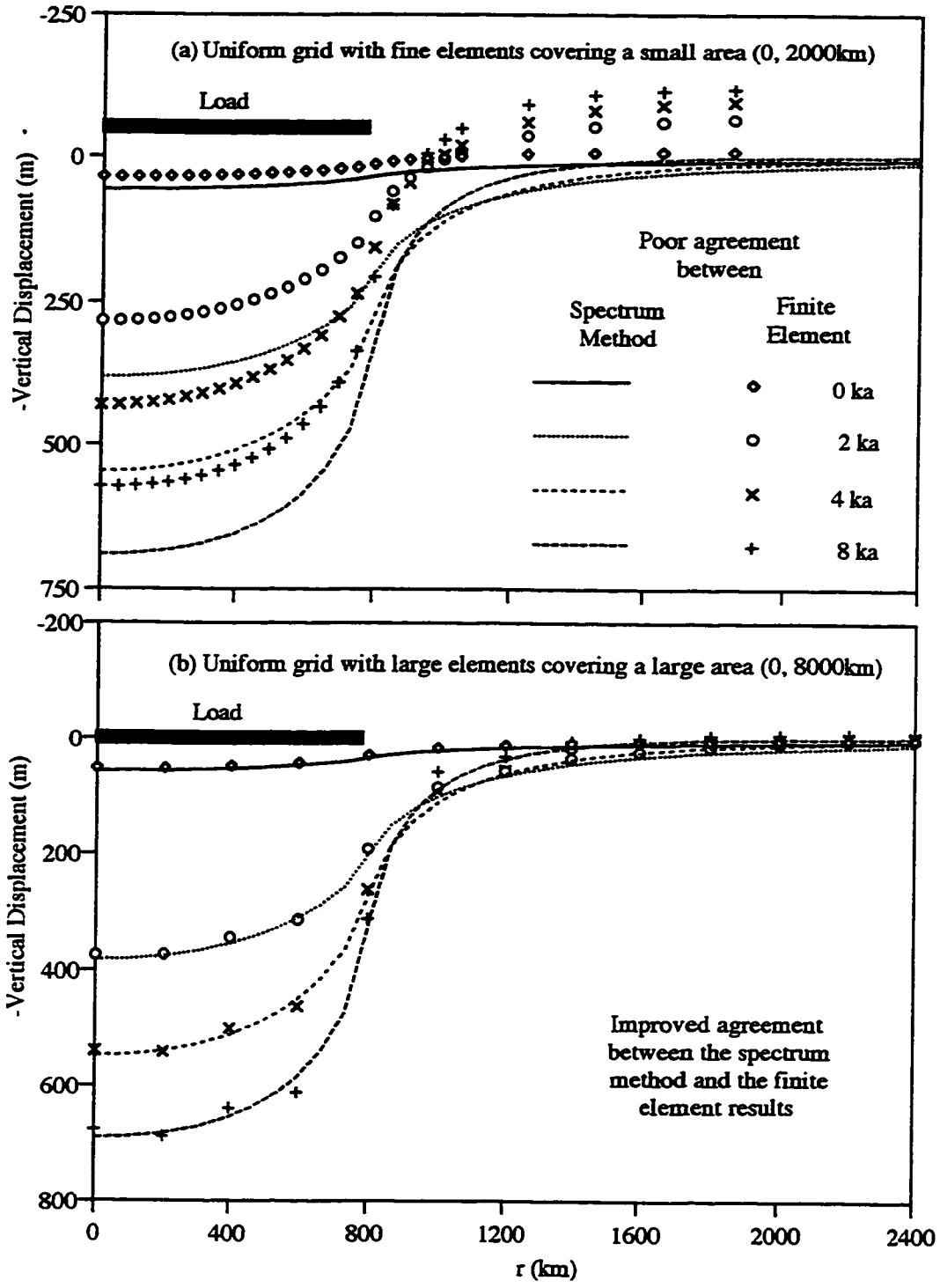

Figure 2.1 Comparison of vertical displacements at 0, 2, 4, and 8 ka after a Heaviside loading event computed by the spectrum method (lines) and the finite element method (symbols) for a Maxwell half-space model. The load is a straight edge disk of ice with 800 km radius and 2500 m thickness. The finite element results in different panels are computed with different grids. Continued on next page.

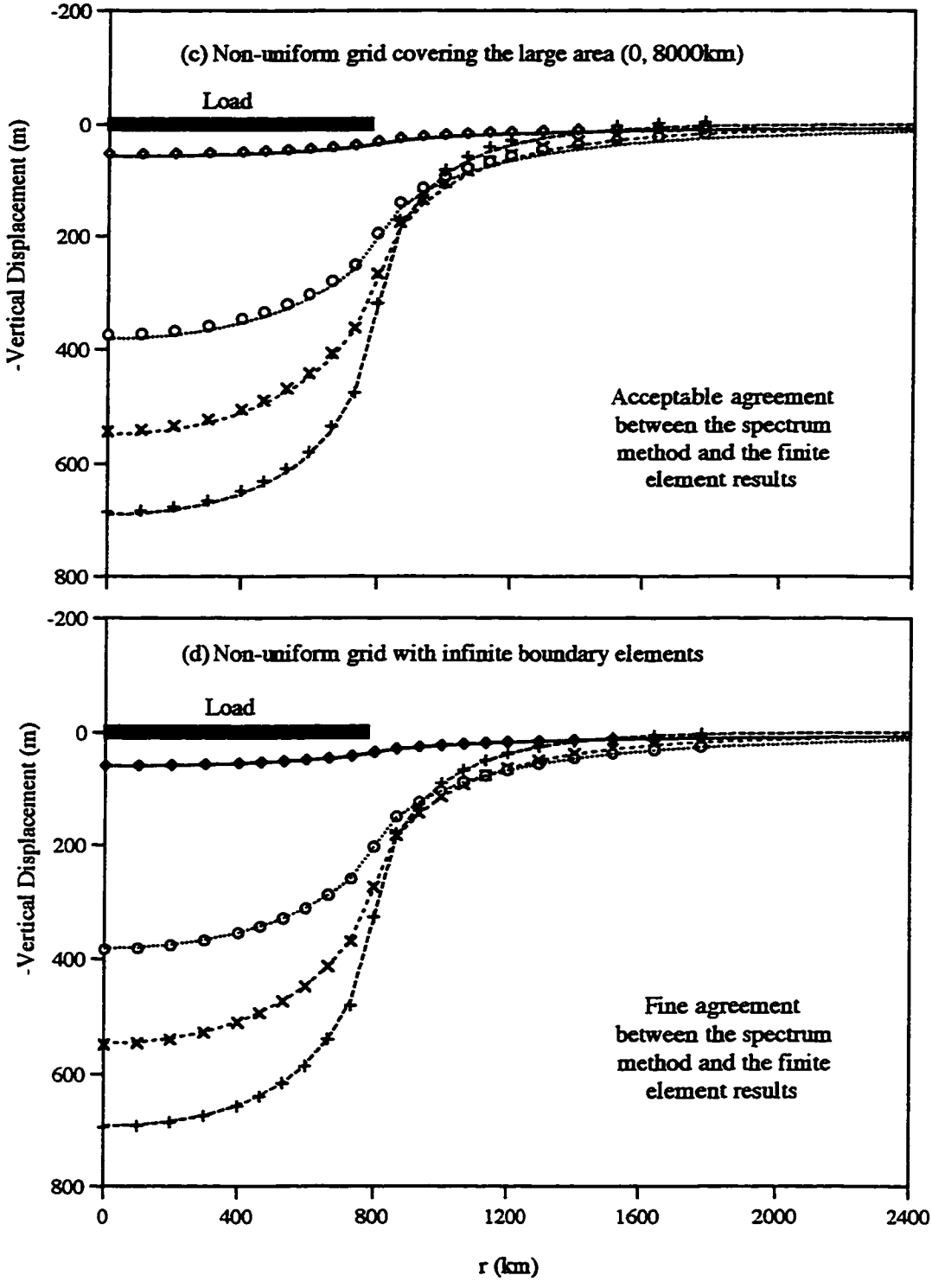

Figure 2.1 Continued.

should extend even farther in the radial direction to model the infinite extent of the half-space.

In Fig. 2.1d, one more element is appended to each layer, and one more layer of elements to the bottom of the model. These additional elements are different from the others in the model. They are infinite boundary elements that are specially designed for modeling an infinite system, such as the half-space. Their aspect ratios can be extreme. With the infinite elements, results of the finite element model are now in an excellent agreement with the results of the spectral method (Fig. 2.1d). The differences are within 0.3% underneath the load. Therefore, the grid with large radial extent, elements of varying radial dimension, and infinite boundary elements is the optimal one to use.

2.2.2 Vertical Resolution

Consider a stratified half-space which contains a horizontal layer with material properties that are different from other part of the model, we wish to find out how many layers of elements are needed to resolve this material layer. Model LV1 has a 200 km thick asthenosphere lying beneath a lithosphere and over a uniform viscoelastic half-space (Fig. 3.3). The viscosity in the asthenosphere is laterally heterogeneous, and is generally less than that underneath. A complete description of the model can be found in the next chapter where it is used to model effects of lateral heterogeneities in asthenospheric viscosity.

Figure 2.2 compares vertical displacements for model LV1 computed using one, two and four layers of elements within the low viscosity asthenosphere. The results show that the solutions converge as the number of layers in the asthenosphere is two or greater. The one layer results are poor and deviate significantly from the others because the solution within the uniform asthenosphere has the form of cosh and sinh functions (Cathles, 1975) and one layer with two nodes to interpolate with a linear shaping function is a poor approximation to these functions. Therefore, one grid is not enough to resolve a distinct material layer. On the other hand, the results computed with four layers are almost same as that with two layers, hence two layers are enough and four layers may be excessive. This conclusion is also confirmed by similar tests for the lithosphere. Thus two layers of elements will be used within each material layer for the rest of the dissertation.

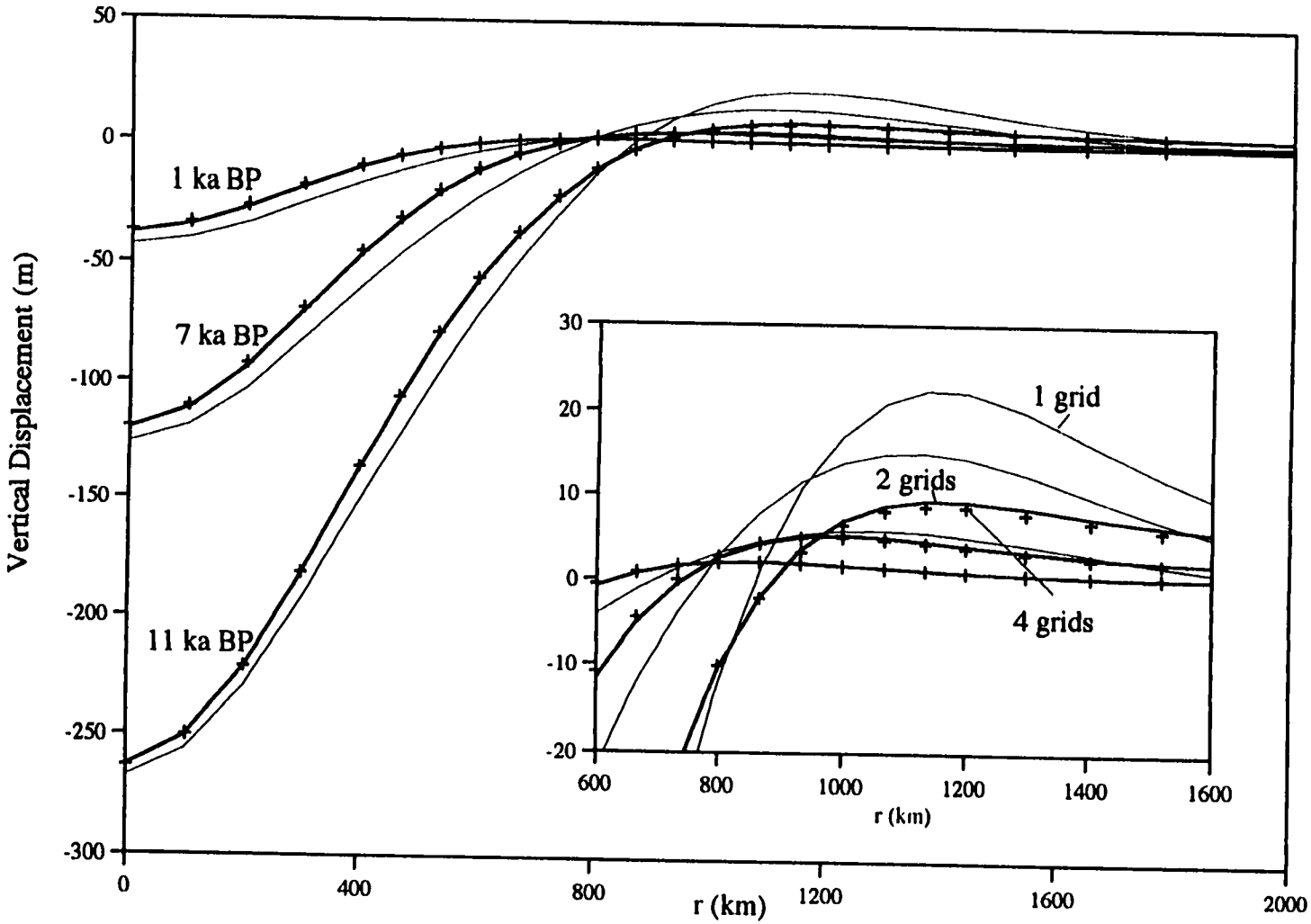

Figure 2.2 Comparison of different number of vertical grids representing the asthenosphere. The displacements are computed for model LV1 using 1 grid (hair line), 2 grids (solid line), and 4 grids (cross), respectively. The load is the disk with the sawtooth history (Fig. 3.1). The insert is a enlarged view around the prebulge area.

2.2.3 The 2D Grid

In summary, the 2D finite element grid that is used in the next two chapters to represent a stratified half-space comprises of 16 grid layers extending from the surface to 11000 km depth. Each layer consists of 40 regular elements and one infinite boundary element, covering an area from r=0 to 16,000 km for most models or from r=0 to 32,000 km for some models in section 4.1. Among the horizontal elements, 10 are within the load area. Elements around the ice edge are refined whereas the elements beyond the load edge are coarser with increasing distance from the center of the ice. Furthermore, our experiments show that the results are not very sensitive to element aspect ratio and any value between 0.05 to 20 can yield satisfactory results. With the infinite boundary elements, there is no need to explicitly prescribe the boundary condition at the bottom and the outer boundary. Nodes at the surface are only constrained by an ice load.

2.3 THE 3D FLAT-EARTH FINITE ELEMENT GRIDS AND THEIR VALIDITY

To evaluate non-axisymmetric 3D models we need truly 3D finite element grids. There are two types of 3D grids that are used in this dissertation. Both are composed of 3D solid elements of rectangular parallelepipeds in Cartesian coordinate systems. One grid is used for an approximate disk load while another is for a realistic ice load in North America. In the following, we first demonstrate the validity of the 3D results for the disk load by comparing them with the 2D results. Then, we shall show the comparison of results between the 3D finite element flat-earth model with the spectral results for a self-gravitating spherical earth for a realistic ice load.

2.3.1 Validity of the 3D Grid for the Disk Load

To demonstrate the validity of the 3D model, we consider a disc load and compare the results with that of the axisymmetric 2D model. Since the shape of the 3D elements at the surface are squares, the disk load is not exactly circular but is approximated by an assemblage of squares shown in Fig. 3.2. The load (pressure) on each square is assigned

to be the ice weight of the portion of the exact disk on the square multiplied by the percentage of the square covered by the load.

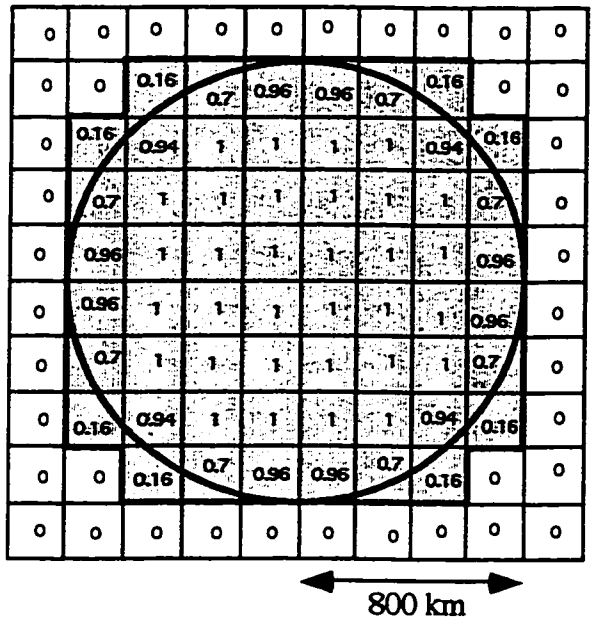

Figure 2.3 Finite element grids lying in the center at the top of the 3D finite element mesh are shown with their weighing factors. The shaded grids are actively loaded to approximate a disk load.

The 3D grid for the disk load has 10 layers of elements from the surface down to 2886 km deep. Each layer consists of 34 by 34 8-node 3D solid elements, covering an area of 240,000 km by 240,000 km. However, only results in the central region are intended to be useful. The grid there is the densest and includes 14 by 14 elements, each with horizontal dimensions of 200 km by 200 km. The horizontal dimensions of the elements outside the central region increase with increasing distance from the center. These coarse elements are used to extend boundaries of the grid far enough so that results in the central region can be free from any boundary contamination. The horizontal displacements at the lateral boundaries are constrained to be zero. Across horizontal material boundaries with density discontinuities (e.g. core-mantle boundary), appropriate buoyancy forces are applied.

To evaluate the validity of the 3D grid, vertical displacements and relative vertical displacement (RVD) are computed with the 3D grid and compared to the 2D results for laterally homogeneous models. The relative vertical displacement is obtained by subtracting present displacement from the previous ones and can be regarded as a first order approximation to relative sea level changes for sites in categories 1, 2, and 3 during the last 7 ka. according to Wu & Peltier (1983).

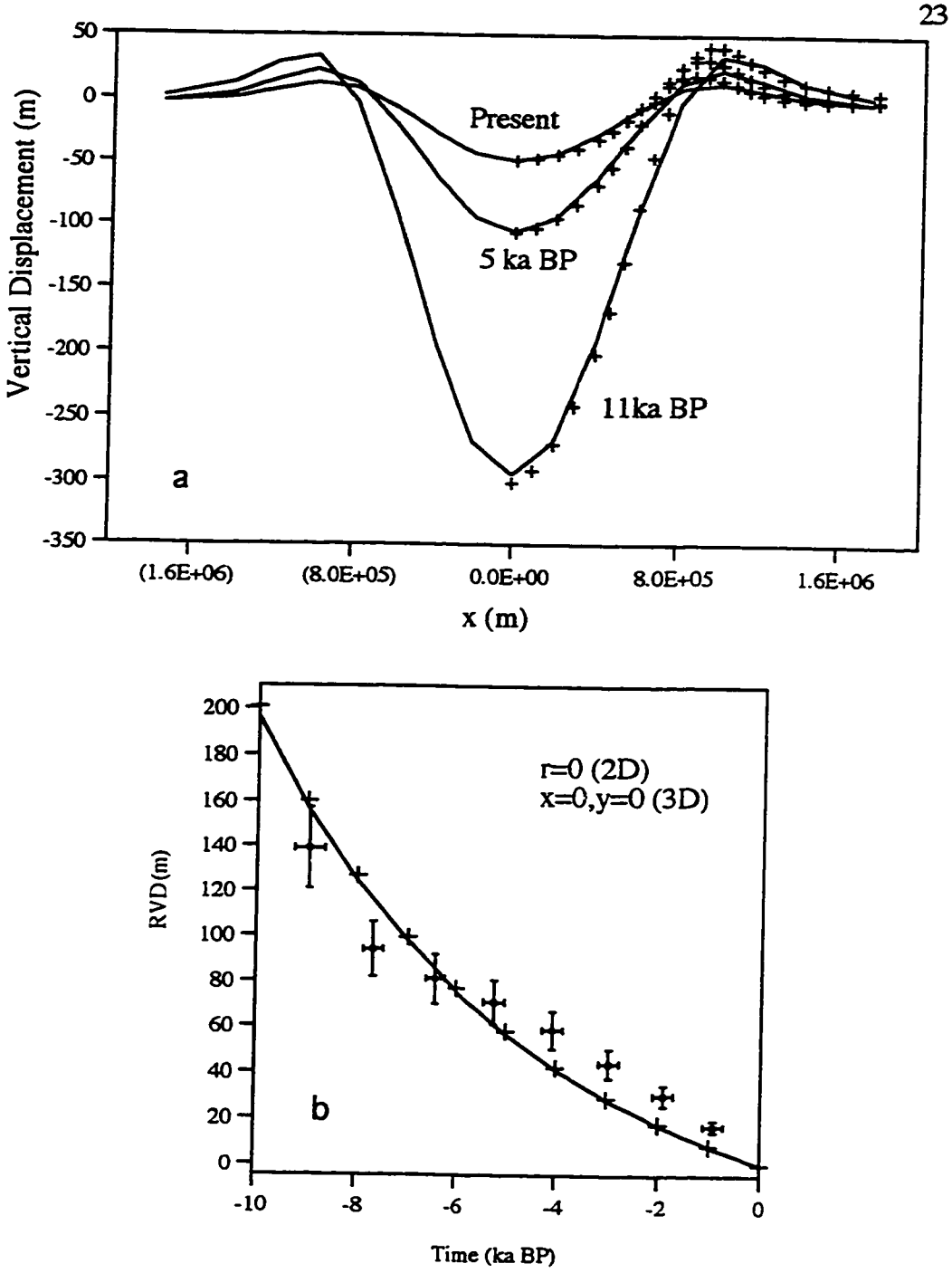

Figure 2.4 Comparison between 2D (cross) and 3D (line) finite element results. Panel A shows vertical displacements at 3 different times while panel B shows RVD histories at the center. The models are R50/21 (2 D) and LITH_50 (3D). Dots with error bars are RSL data at Kristiinankaupunki in Fennoscandian region which show resolving capability of the data.

Fig. 2.4a shows the comparison of vertical displacements between models R50/21 (2D) and LITH_50 (3D). Both earth models are physically the same and composed of a homogeneous lithosphere of 50 km over a viscoelastic half-space of 10^{21} Pa-s. The two models are incompressible and with same density and shear modulus as models in the next chapter. The load history is also described in the next chapter. The vertical displacements for the two models are quite close inside the load area. The difference at the center is about 2.2%. Around the load edge, the comparison is not as good. The peak of the forebulge is missed by the 3D results. This is due to the coarse grid used in the 3D model which cannot accurately represent a circular disk near the edge, nor capture sharp lateral gradients of the deformation. In general, the comparison of the displacement between the 3D and the 2D results is not as good as the comparison between the 2D and spectral method in Fig. 2.1. However, the comparison (Fig. 2.4b) of relative vertical displacement (RVD) at the center appears good because the differences are much smaller than the error in RSL data. Therefore, the 3D finite element model is still usable for tests of sensitivity of RVD to the earth properties. This is to be further demonstrated for a similar 3D grid in the next subsection.

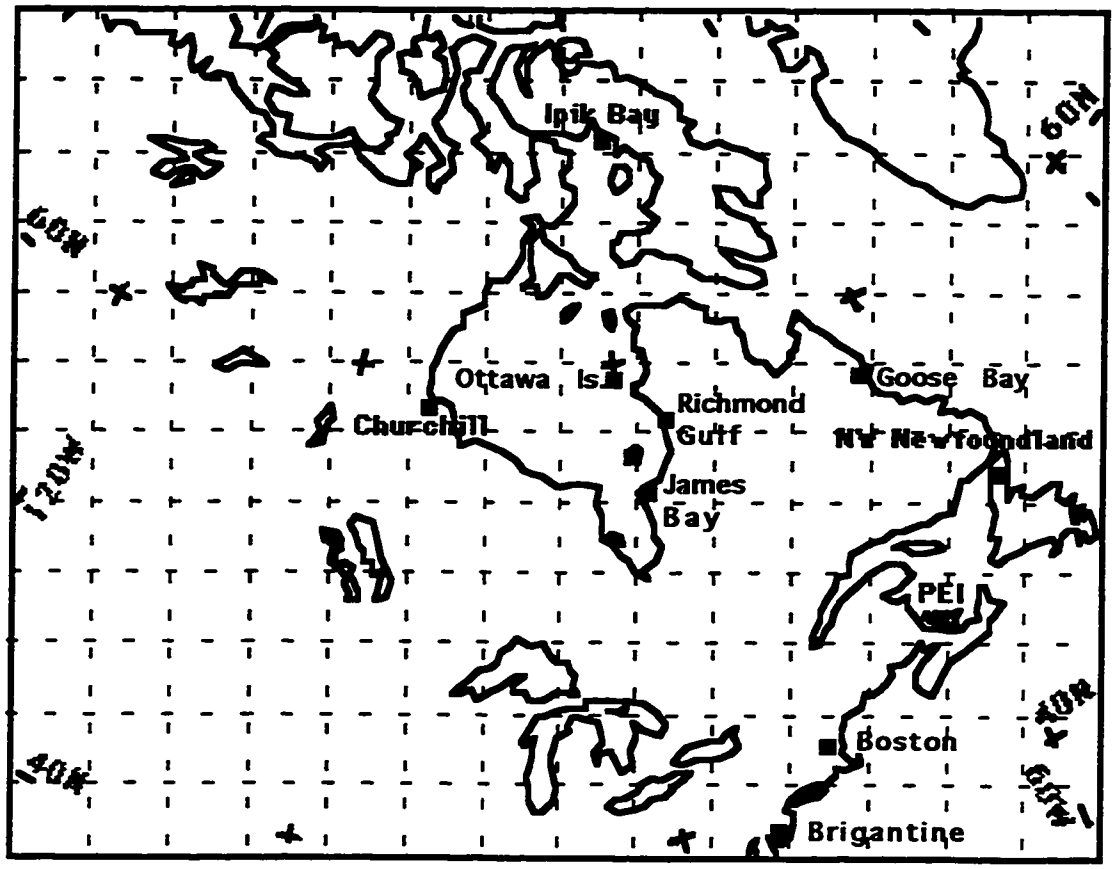

Figure 2.5 Some RSL sites in Hudson Bay and surrounding area overlay the 14 x 12 finite elements of the top layer in the central region.

2.3.2 Validity of the 3D Grid for the Realistic Ice Load

Next, we use a 3D finite element grid for computing the response to a realistic ice load (ICE-3G) in North America. The grid is similar to the previous one with slight differences. It still has 10 layers of elements extending to 2886 km depth. The z-coordinates of the 11 nodal points in depth are 0, -25, -50, -100, -150, -200, -420, -670, -1220, -1770, -2886 km. Each layer has 34 x 32 3D solid elements covering an area of 240,000 km x 193,800 km. The horizontal dimensions of each of the 14 x 12 elements in the central region are 340 km x 323 km as shown in Fig. 2.5. Also shown in Fig. 2.5 are locations of some RSL observation sites that are used in the dissertations. The load area covers 16 x 14 elements at

center of the top layer of elements. The earth model consists of a 150 km lithosphere overlying a uniform 10^{21} Pa-s half-space.

The RVD of this non-self-gravitating flat-earth is compared with that computed using the spectral method for a self-gravitating spherical earth model of similar vertical structure by Wu and Johnston (1998). Their comparison shows that the difference between the results of the two models are small and cannot be resolved by the uncertainties of RSL data for sites near the center of rebound (Fig. 2.6) and for peripheral sites such as NW Newfoundland and Boston (Fig. 2.7). The discrepancies between the two results are large at Prince Edward Island (PEI) which can be explained as a result of inadequate spatial resolution in the finite element model that can not honor the original ice model precisely. For sites further away from the glaciated area, the differences become larger and is due to the difference between the flat earth and the spherical surface. Hence, even for the load size in North America, the flat earth model can adequately describe the postglacial rebound process at sites in categories 1, 2, and 3. However, the accuracy is dependent on the spatial resolution of the finite element model (Fig. 2.4a & the relevant text) which, in turn, is constrained by the computing resources.

From the 2D grid to the 3D grid, there are some gains and some losses. The major gain is flexibility and capability to accommodate a wide range of model geometry besides the axial-symmetric ones. The three dimensional models can expand our understanding of the effects of lateral heterogeneities by allowing a wide range of load and heterogeneities that can be hypothetical for testing ideas as well as realistic for fitting observational data and inferring 3 dimensional rheological structure of the earth. However, this advantage can be compromised by a loss of spatial resolution due to a limitation of computing resources because a 3D model is much more expensive to compute than a 2D model. A typical run of a 3D laterally heterogeneous model with a variation in viscosity can take as long as 12 days on an IBM RS6000 server at the University of Calgary. In comparison, a similar 2D cylindrical model takes only about 10 minutes. Consequently, only a very limited number of 3D models can be run.

In summary, we have presented the finite element models and demonstrated their validity. The next three chapters will use these models to study the effect of lateral heterogeneity on postglacial rebound.

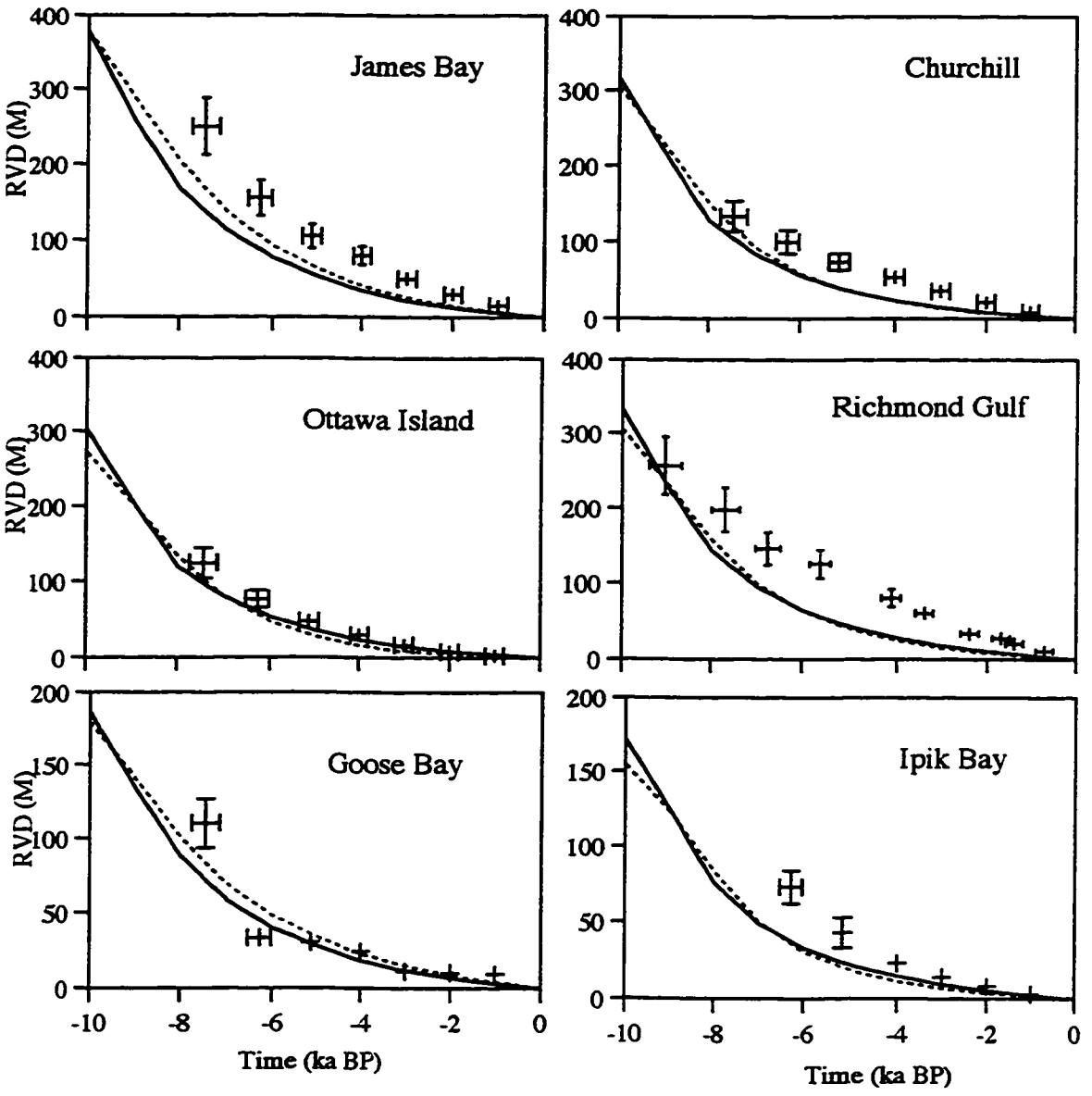

Figure 2.6 Comparison of relative vertical displacements between the spherical spectral model (dot line) and flat-earth finite element model (sold line) for some sites in eastern Canada (from Wu & Johnston, 1998, used with permission).

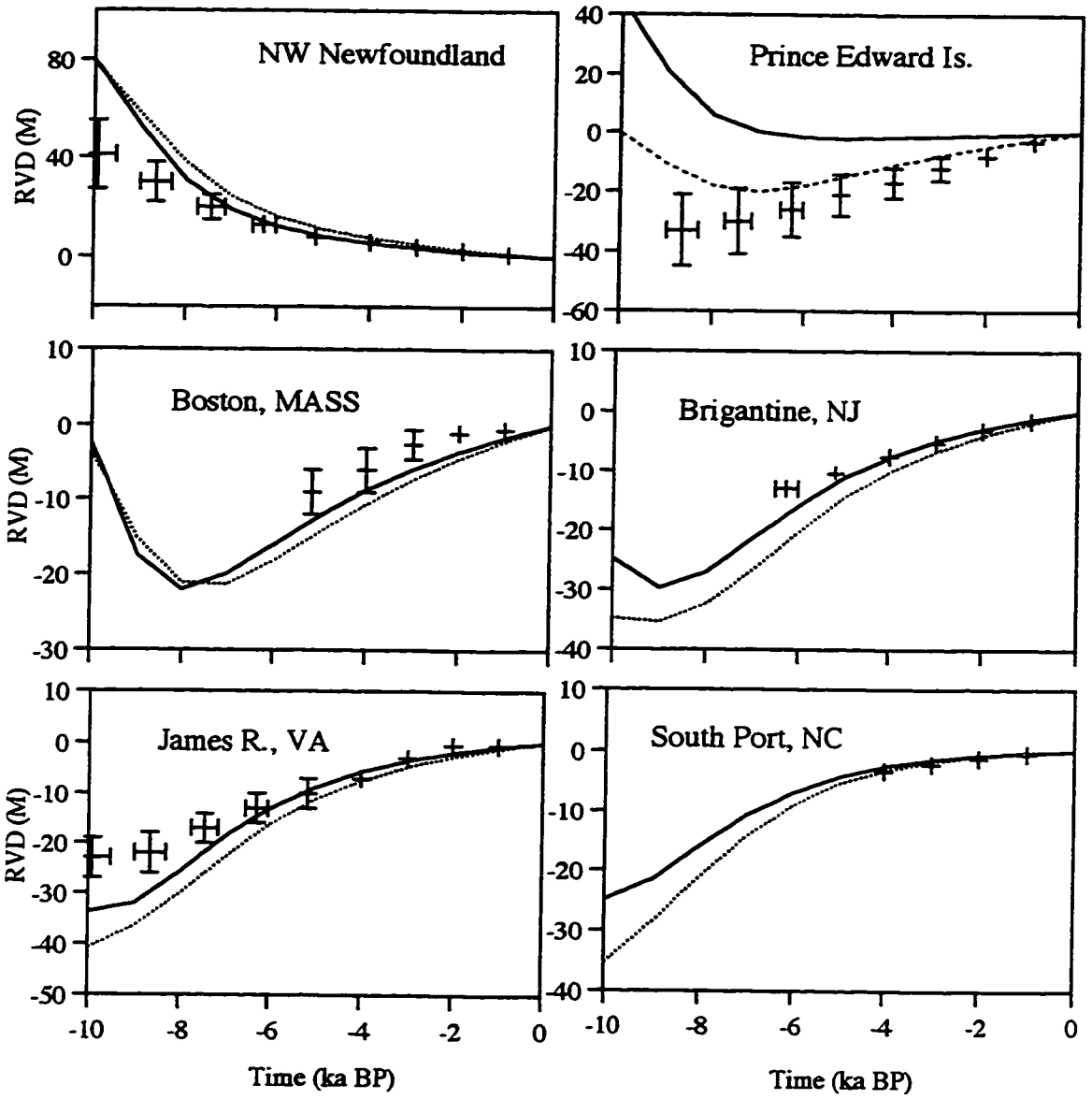

Figure 2.7 Same as in Fig. 2.6, except that the sites are along the east coast of Canada and the USA (from Wu & Johnston, 1998, used with permission).

CHAPTER 3

TWO DIMENSIONAL FINITE ELEMENT RESULTS PART 1: EFFECTS OF LATERAL HETEROGENEITIES IN THE ASTHENOSPHERE AND LITHOSPHERE ON POSTGLACIAL REBOUND

In this chapter, the effects of lateral variations in asthenospheric viscosity or thickness and lithospheric thickness on postglacial rebound are evaluated using the 2D cylindrical finite element grid described in the previous chapter. The earth models are taken as incompressible with a uniform density of 3380 kg/m^3, shear modulus of 0.67x10^{11} Pa for the lithosphere and 1.45x10^{11} Pa for the material beneath it.

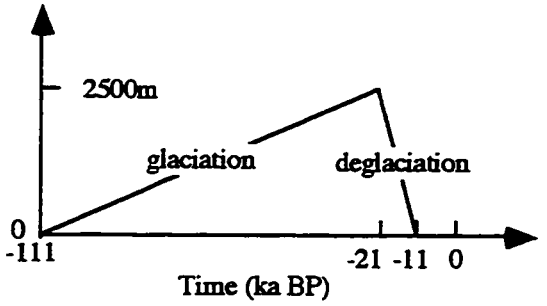

Figure 3.1 Sketch of the ice history of the sawtooth loading cycle. The vertical axis is the maximum thickness of the disk load.

The loading history (Fig. 3.1) considered is a simple approximation of the Late Pleistocene glacial cycle based on global ice volume history from deep sea core data (Peltier, 1986). It has a growth of the ice over 90 ka reaching its maximum thickness at 21 ka BP which is followed by a rapid deglaciation of 10 ka (Peltier, 1994). The deglaciation was completed at 11 ka BP. Unless otherwise stated, the ice model has a parabolic cross section (Paterson, 1981) with a maximum height of 2500 m in the load center, a radius of 800 km, and a density of 1000 kg/m^3. Thus, its dimensions are comparable to the Late Pleistocene ice sheets over Fennoscandia or the Barents Sea.

The effects of lateral heterogeneity on RVD are first investigated in detail. Then, the effects on other geodetic quantities including vertical uplift rate, gravity anomaly, horizontal displacements and velocities are also predicted.

3.1 EFFECTS ON RELATIVE VERTICAL DISPLACEMENT

To study the effects of the lateral heterogeneities, we follow Kaufmann et al. (1997) and compare predicted vertical displacements and relative vertical displacement for laterally heterogeneous models with those for laterally homogeneous reference models. Throughout this section, the effects of lateral heterogeneities are considered to be significant if differences in RVD between the laterally homogenous and heterogeneous models are larger than the observational uncertainties of RSL. Thus, RSL data with error bars from the Fennoscandian region (see Fig. 3.2 for site locations) have been included in the diagrams for comparison. The validity of using a suite of laterally homogeneous models to detect the presence of lateral heterogeneities is also examined.

As discussed in chapter one, seismic tomography shows that the continents are anomalously fast and cold when compared with the nearby region beneath the oceans. This can mean relatively higher asthenospheric viscosity or/and thinner asthenosphere under the continental shield than under young oceanic lithosphere. The effects of these two kinds of lateral heterogeneities are evaluated respectively in the following two subsections.

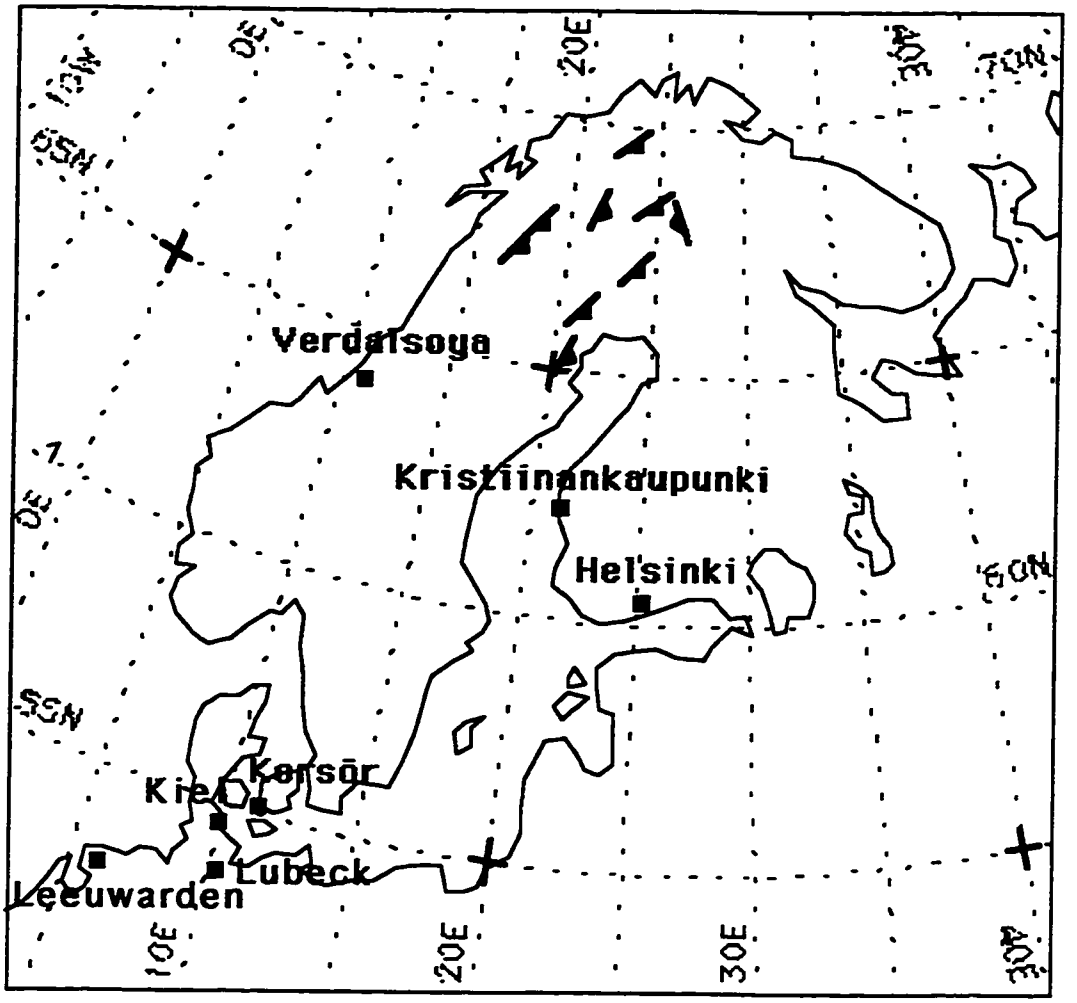

Figure 3.2 Location map showing the RSL observation sites in Fennoscandian region that are used in this dissertation.

3.1.1 Effects of Lateral Variations in Asthenospheric Viscosity

First, let us consider the effects of lateral viscosity variations in an asthenosphere with constant thickness. In the laterally heterogeneous model LV1, asthenospheric viscosity decreases stepwise every 400 km from 10^{21} Pa-s under the load to 10^{18} Pa-s outside the load while asthenospheric thickness is kept constant at 200 km (see Fig. 3.3). Above the asthenosphere is a uniform 110 km thick elastic lithosphere and below the asthenosphere lies a uniform 10^{21} Pa-s viscoelastic half-space. The choices of lithospherical thickness here and in the subsequent sections are mostly based on lithospherical flexure studies by

Walcott (1970a & b). Reference models used are R110/21, R110/20, R110/19, and R110/18 where R stands for reference model and the two numbers indicate lithospheric thickness in kilometers and the exponent of asthenospheric viscosity respectively. For example, model R110/19 has a 110 km thick lithosphere and a 10^{19} Pa-s asthenosphere. Thus, all reference models have a 110 km thick lithosphere and they only differ from model LV1 by having a homogenous asthenosphere.

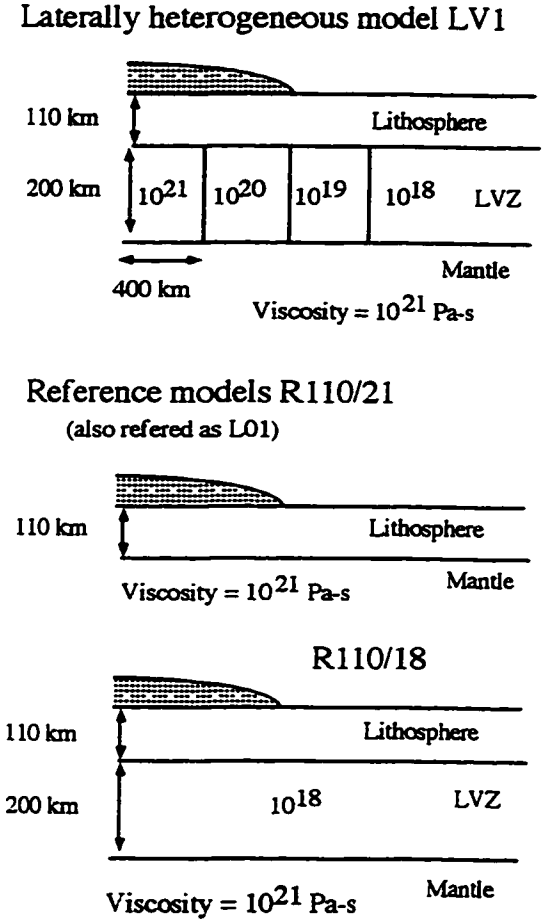

Figure 3.3 Sketches of laterally heterogeneous earth model LV1 and two reference models R110/21 and R110/18. Two other reference models R110/19 and R110/20 are not shown here and they differ from R18 only by different viscosity value in the lower viscous zone (LVZ).

The RVD history curves at selected sites of different distance (r) from the center of the load are plotted in Fig. 3.4 while Fig. 3.5 shows the RVD profiles at two discrete times, 5 and 10 ka BP. Fig. 3.4 shows that the effects of lateral heterogeneities cannot be clearly seen at any single site because RVD history curves for model LV1 display no recognizable characteristics that can set it apart from those for the laterally homogeneous models. In fact, lateral heterogeneities can only be detected by fitting a suite of laterally homogenous earth models to the observations at different sites.

Suppose the earth is laterally heterogeneous with properties given by model LV1, thus the observed sea levels at different sites are given by the LV1 curves (solid lines) in Fig. 3.4. If we use the suite of laterally homogenous models to compare with the observations, then we will find that different reference models will fit the observations at different sites. Fig. 3.4 shows that the curve LV1 is close to the curve R110/21 at r=0 km, and moves towards the curve R110/20 at r=200 km and 300 km (Fig. 3.4). At r=400 km, the curve LV1 is almost the same as the curve R110/20. The curve LV1 then moves towards the curve R110/19 at

r=600 km. This "migration" of the curve LV1 among the reference curves can be interpreted as due to lateral heterogeneities if the load model is well determined. The effects are significant if the difference is detectable by the uncertainties of the RSL data. However, if we try to determine the value of the viscosity beneath the site from the asthenospheric viscosity of the reference model that lies closest to the LV1 curve, a lower viscosity value is obtained. For example, at r=600 km (Fig. 3.4), the curve LV1 is closest to the curve R110/19 whereas the actual viscosity underneath is 10^{20} Pa-s.

Furthermore, the comparison of the curve LV1 with the reference curves is not diagnostic for sites at r = 667, 734, and 800 km, in the inner peripheral area (Fig. 3.4). This is because the relative positions of the reference curves in the panels do not show simple correlation with the viscosity as they do in panels for sites at r < 600 km. For example at r=734, the curve R110/21 lies between the curves R110/19 and R110/18 (Fig. 3.4). This can be explained by crossings among the RVD profiles (Fig. 3.5A & B) around at these sites.

Another contributing factor to the anomalous sequences is that model R110/18 has a short relaxation time due to its low viscosity channel. By the time 8 ka BP, its relaxation is almost finished and its RVD curves are almost flat and close to zero from that time on (Fig. 3.4). On the other hand, the other curves at these inner peripheral sites are still not flat due to the migration of their forebulges.

If we disqualify the curve R110/18 as a reference for time after 8 ka BP, the rest of the sequences of reference curves at sites r=867, 1000, 1200, 1400 km are consistently reversed from that for sites with $r \leq 600km$ and the curve LV1 is consistently moving towards R110/19 (Fig. 3.4). The comparison of the curves works again but the inferred asthenospheric viscosity is larger than the actual value. For example, at the site r=1400 (Fig. 3.4), the curve LV1 lies between the curves R110/19 and R110/20 with closer proximity to the curve R110/19. However, the actual asthenospheric viscosity is 10^{18} Pa-s underneath the site. On the other hand, comparing the position of LV1 relative to the reference curves at these sites correctly suggests that asthenospheric viscosity decreases with distance from the ice margin.

Because this method of comparison underestimates the viscosity inside the load but overestimates it outside, the method cannot be used at peripheral sites across the load margin for detecting the lateral heterogeneities. For example, comparing the two sites

r=600 km and 867 km (Fig. 3.4) may lead to the wrong conclusion that lateral asthenospheric viscosity increases from r=600 km to 867 km. Therefore, comparison of peripheral sites across the load margin should be avoided. On the other hand, comparing between sites r = 0 km and r = 1400 km can certainly establish existence of the lateral variations. Hence, the spatial trend of lateral variation in land uplift inferred by the comparison method well inside the load area or the forebulge area can reflect the spatial trend of lateral heterogeneities of the earth, but not in a small area around the load edge.

The behavior of the RVD curves at peripheral sites (Fig. 3.4) is closely related to the characteristics of the forebulge. This has been discussed by Kaufmann et al. (1997) and can be seen in Fig. 3.5C. For the deep flow model R110/21, the forebulge is prominent and migrates inwards with time whereas for the channel flow model R110/19, the forebulge is less pronounced and migrates outwards (e.g. Wu, 1993). The forebulge for model LV1 displays characteristics of both deep and channel flows. The height of the bulge is reduced to about two-third relative to that for model R110/21 while the bulge is still migrating inwards. So, there may be a mixed flow in the laterally heterogeneous model LV1, with deep flow underneath the load and channel flow further outside.

In summary, the effects of lateral asthenospheric viscosity variation in model LV1 can be detected by comparing RVD curves for LV1 at different localities with the reference curves. However, the inferred viscosity is lower for sites well inside the load area and higher in the forebulge area than the actual values, and the method cannot be used at peripheral sites across the load margin for detecting lateral heterogeneities. Therefore, this comparative method can be used for sites well inside the load area or the forebulge area but not in a small area around the load edge. Furthermore, the least viscous part (10^{18} Pa-s) of the asthenosphere in model LV1 cannot be inferred from the comparison with reference models. This may imply that viscosity not higher than 10^{18} Pa-s can not be 'seen' in the time window of the last 8 ka.

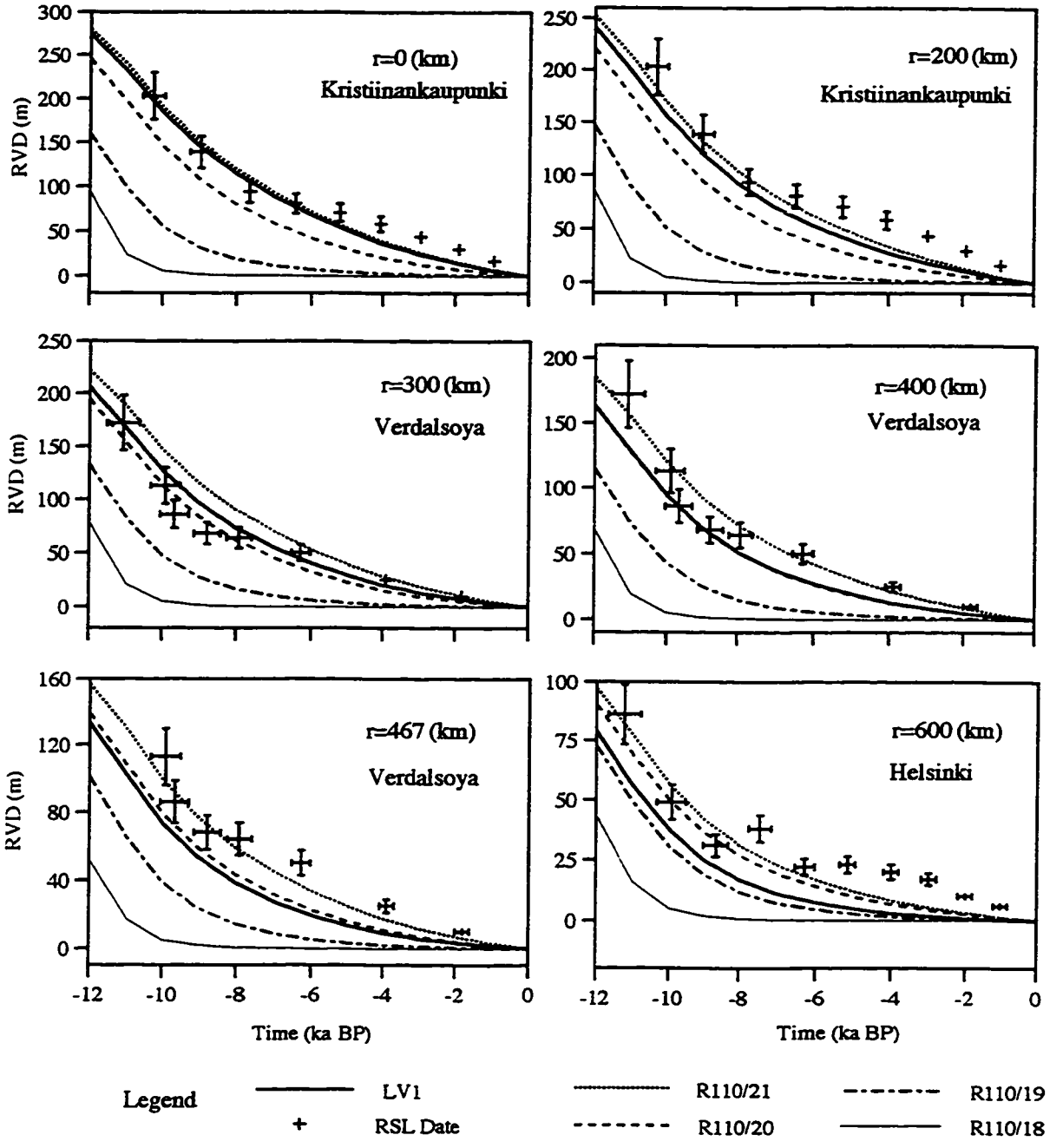

Figure 3.4 Computed RVD time histories for model LV1 and reference models R110/21, R110/20, R110/19, and R110/18 with the sawtooth loading cycle ended at 11 ka BP. Each panel is labeled with distance (r) of the site from the center of the disk load and locality of RSL data from Fennoscandian region. The RSL data are plotted with error bars as reference to how large a difference among the computed curves can be resolved by observation. Continued on next page.

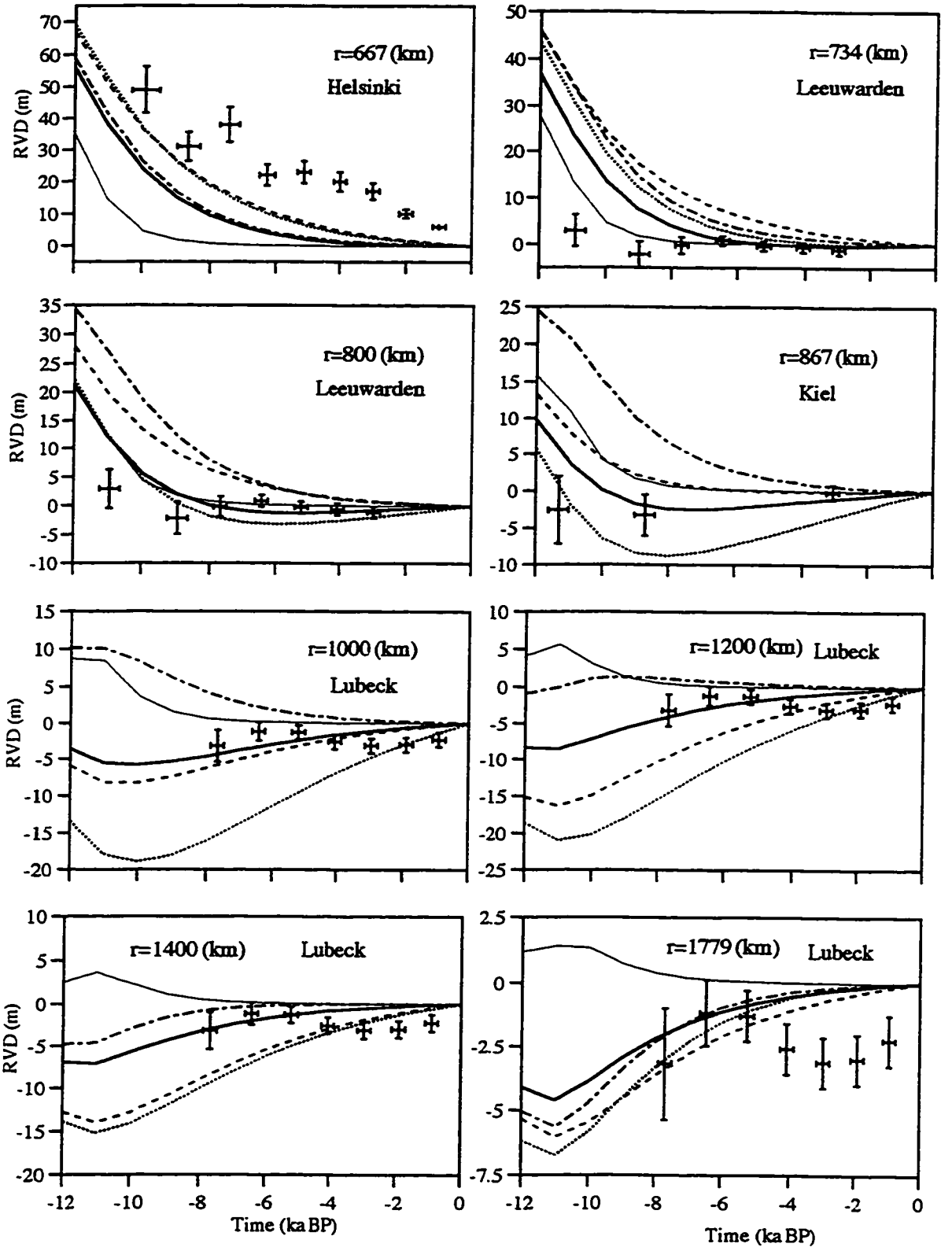

Figure 3.4 Continued.

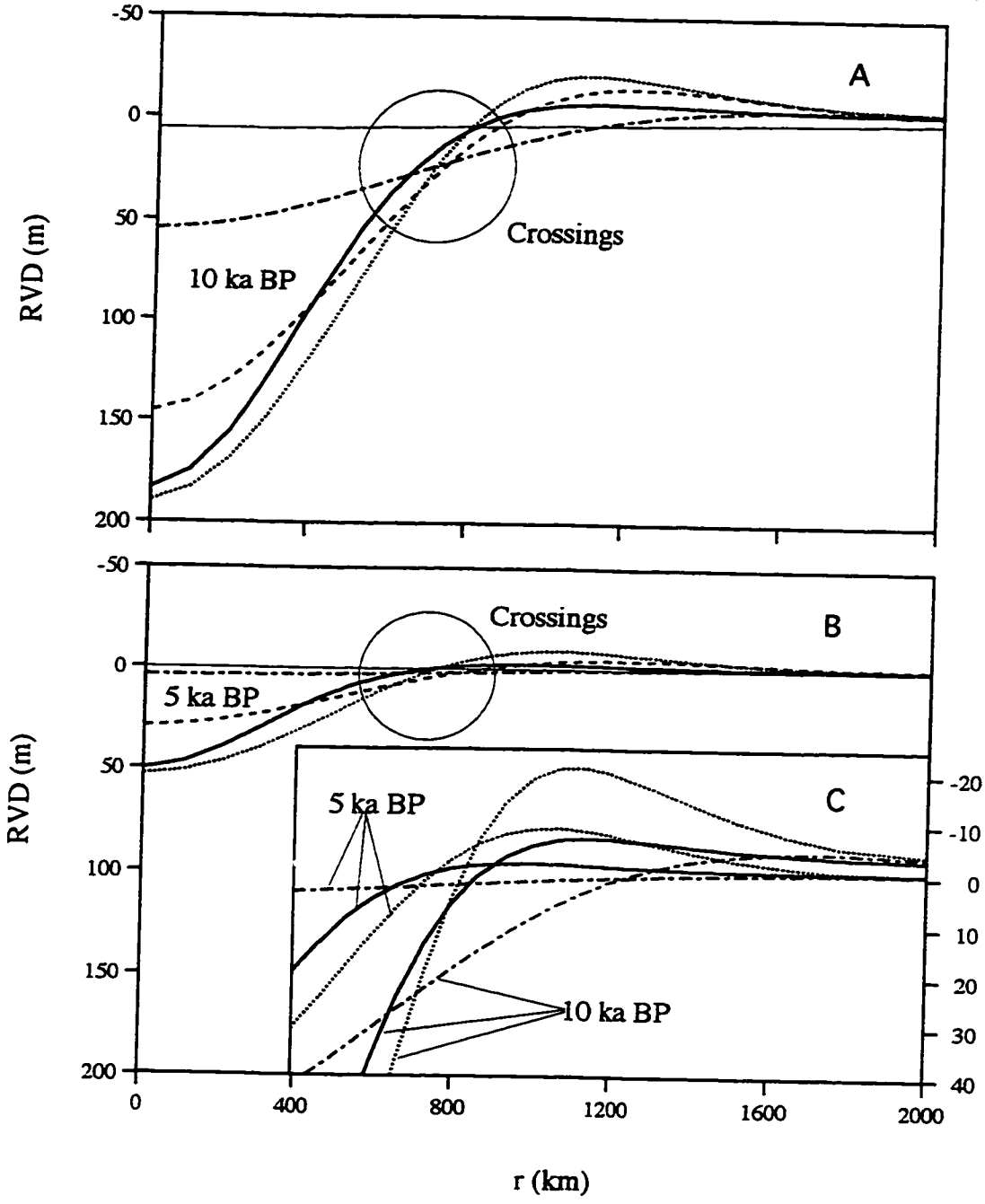

Figure 3.5 Computed RVD profiles for lateral heterogeneous model LV1 (solid line), and reference models R110/21 (dot line), R110/20 (dash line), R110/19 (chain line), and R110/18 (hair line) at 10 ka BP (Panel A) and 5 ka BP (Panel B). The insert (Panel C) inside Panel B shows the migration of the forebulges for models LV1, R110/21, and R110/19 in a larger vertical scale.

3.1.2 Effects of Lateral Variations in Asthenospheric Thickness

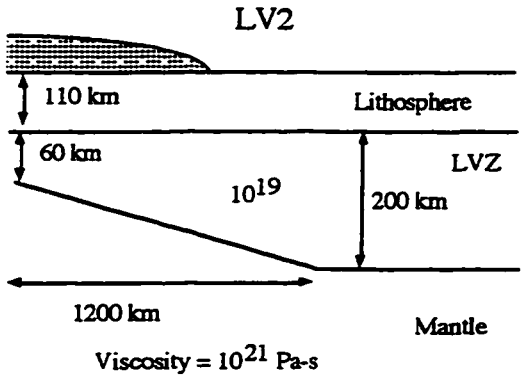

Figure 3.6 Sketch of model LV2 whose thickness of the lower viscous zone varies.

Here we consider the viscosity to be constant but the asthenospheric thickness decreases from under the oceanic area to under the continental area. In model LV2, the asthenospheric thickness decreases linearly from 200 km at r=1200 km and beyond to 60 km at r=0 km while the viscosity is 10^{19} Pa-s (Fig. 3.6). Other aspects of the model are the same as that for model LV1.

Fig. 3.7 shows the computed RVD time histories for model LV2 and the reference models R110/19, R110/20, and R110/21 at selected sites. Again, no characteristic effects of lateral heterogeneities on RVD history curves can be found at any single site but the "migration" of the curve LV2 among the reference curves from site to site reveals the lateral heterogeneities in the asthenosphere.

The effects of lateral thickness variations in the asthenosphere shown in Fig. 3.7 are very similar to that due to lateral viscosity variations in the previous model LV1, with thinner asthenosphere producing similar effects as higher asthenospheric viscosity. At the center where the asthenosphere is the thinnest, RVD curves for model LV2 lie very close to that for model R110/20 (Fig. 3.7). When the asthenospheric thickness increases with increasing distance from the center, the curves for model LV2 move away from that for model R110/20 and towards that for model R110/19 until r = 600 km (Fig. 3.7). Beyond this point in the peripheral area, the curves for most of the models cross, so that relative positions of the curves can not be used for simple interpretation of the asthenospheric thickness.

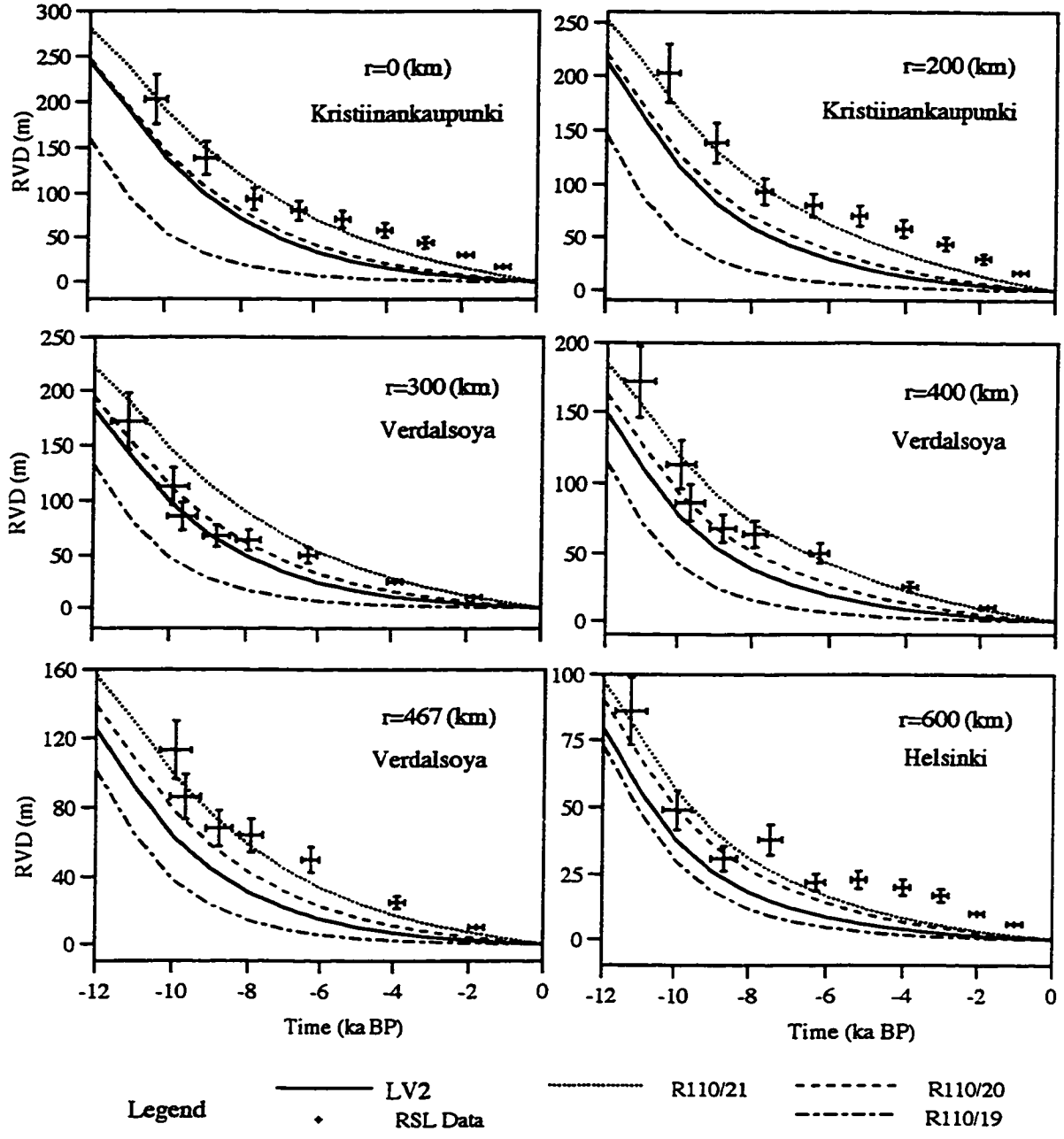

Figure 3.7 Similar to Fig. 3.4 except for model LV2 and reference models R110/21, R110/20, and R110/19. Continued on next page.

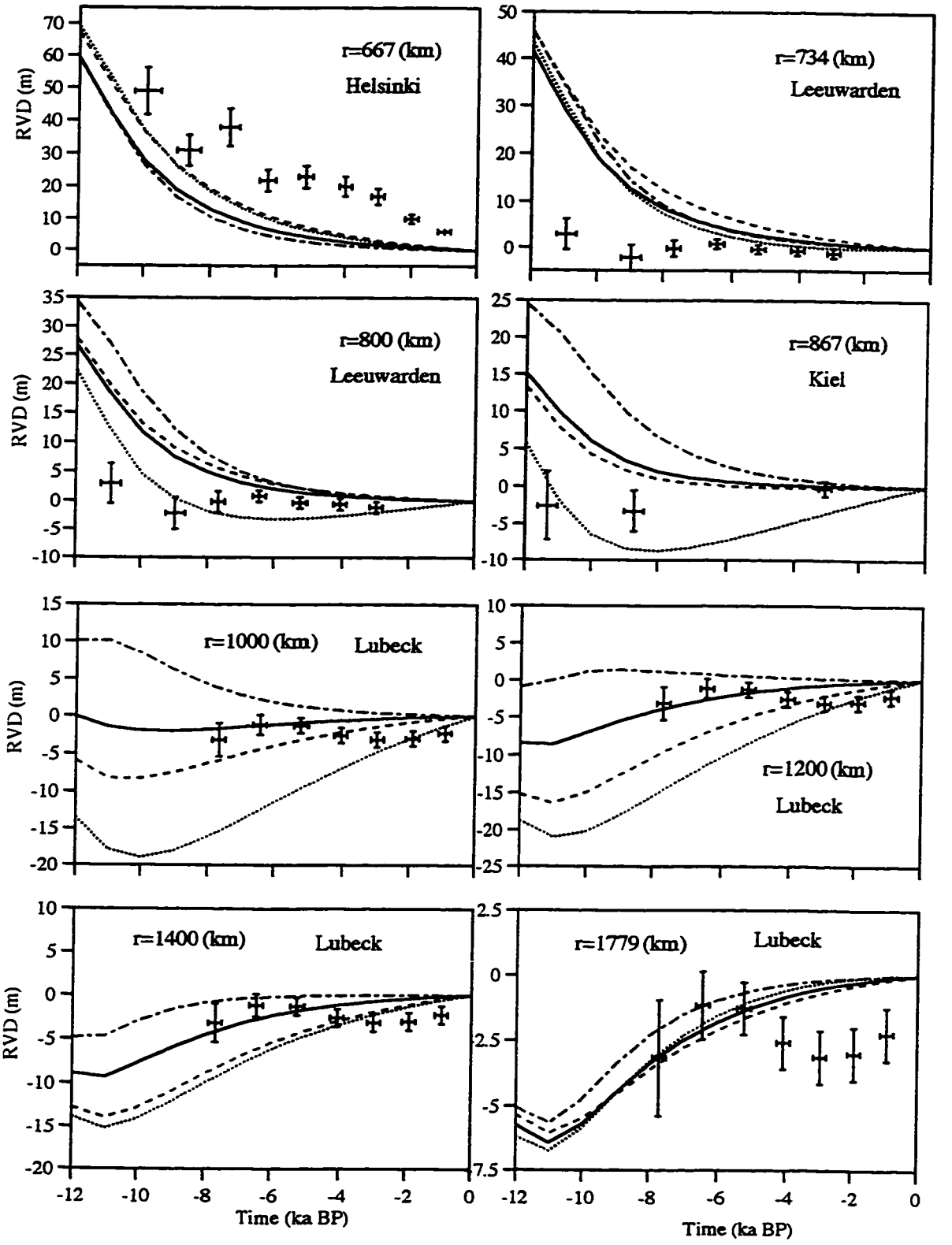

Figure 3.7 Continued.

3.1.3 Effects of Lateral Variations in Lithospheric Thickness

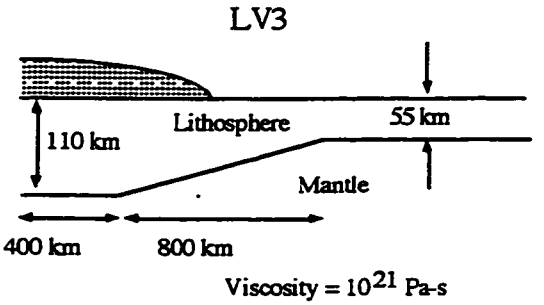

Figure 3.8 Sketch of model LV3 whose lithospheric thickness varies gradually.

Here, we consider the effects of lateral variations in lithospheric thickness. In model LV3, the lithospheric thickness changes gradually from 110 km for $r \le 400 km$ to 55 km for $r \ge 1200 km$ (Fig. 3.8). Beneath the lithosphere is a viscoelastic halfspace of 10^{21} Pa-s. Model LV3's results will be compared with those for reference models R110/21, R90/21, R70/21, and R55/21. The reference models have different lithosphere thicknesses overlying a viscoelastic half-space of 10^{21} Pa-s as indicated in their names. Thus all models including model LV3 have a 10^{21} Pa-s mantle but without an asthenosphere.

The vertical displacements are plotted in Fig. 3.9 while the RVD histories are in Fig. 3.10. Note that the difference between the RVD history curves for model LV3 and the reference models are very small for sites from r=0 to 667 km (Fig. 3.10) and can not be resolved by the uncertainties of the RSL observations. The sequence of the curves can only be recognized in the enlarged portions of the curves (inserts in Fig. 3.10). However, on the edge at r = 800 km, the differences among the models become marginally detectable.

The displacement curves (Fig. 3.9) for the reference models cross in a narrow inner peripheral area, thus the comparative method of using the reference curves works in larger areas. Local thickness of the lithosphere in model LV3 can be inferred by comparing the curves for model LV3 with those for the reference models at most sites (Figs. 3.9 & 3.10). For instance, the displacement (Fig. 3.9a) and RVD curves (Fig. 3.10) for model LV3 are very close to that for R110/21 at the center; and at a distance greater than 1500 km, the displacement is close to that for model R55/21 (Fig. 3.9b), so is the RVD curve at the site r=1400 km (Fig. 3.10); in between, the displacement curves for model LV3 meander through those for models R90/21 and R70/21, so do the RVD curves (Fig. 3.10) at sites

r=800 km and 867 km (close to the curve R90/21) and r=1000 km (close to the curve R70/21).

In comparison with the effects of lateral asthenospheric heterogeneities in the previous models LV1 and LV2, lithospheric thickening reduces the amplitude of RVD within the load while increasing asthenospheric viscosity or decreasing asthenospheric thickness increases the amplitude. However, the effects of lateral variations in lithospheric thickness are generally smaller than that of the asthenosphere.

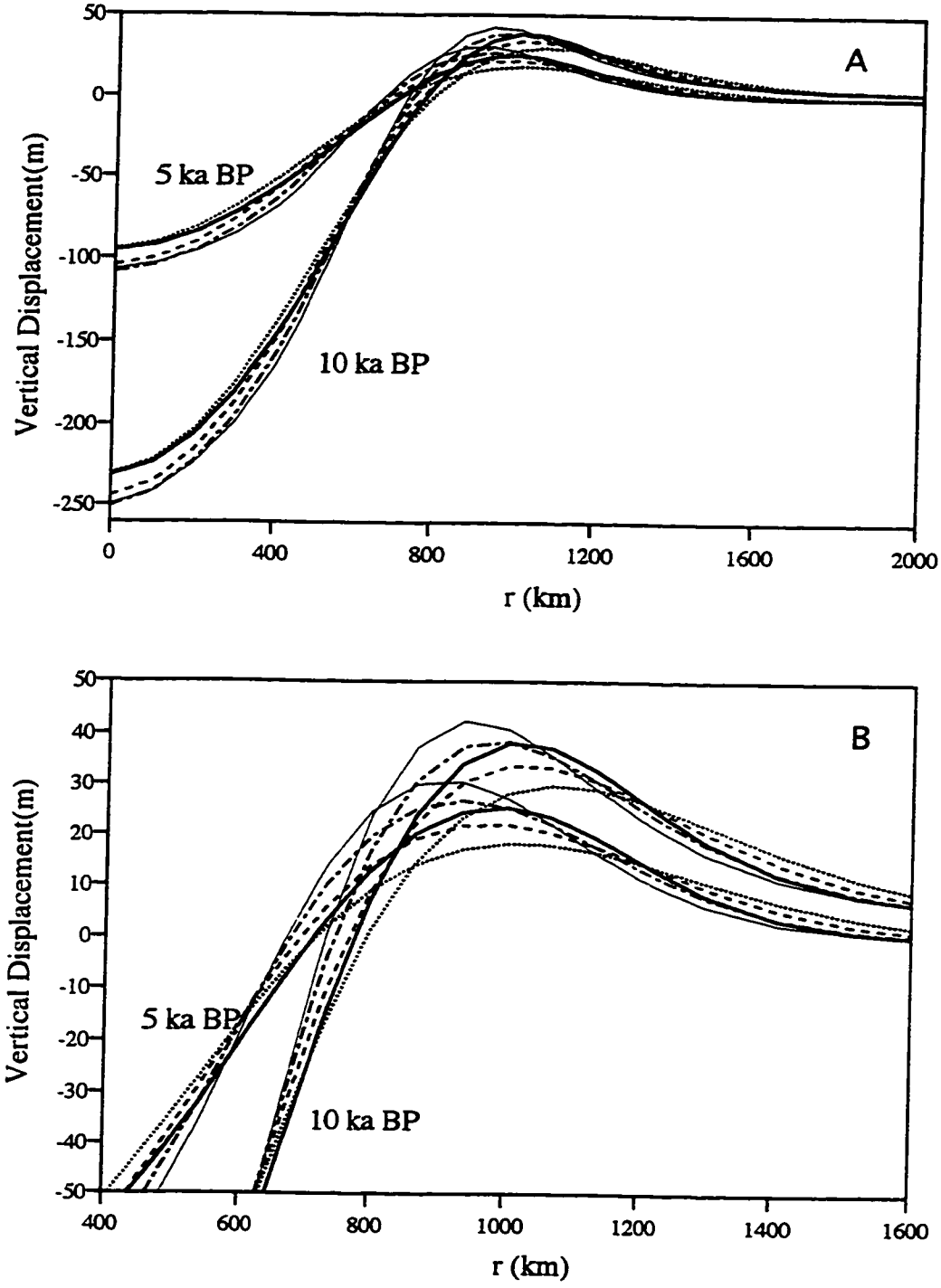

Figure 3.9 Computed vertical displacement for lateral heterogeneous model LV3 (solid line), and reference models R110/21 (dot line), R90/21 (dash line), R70/21 (chain line), and R55/21 (hair line) at 5 ka BP and 10 ka BP. Panel B displays an enlarged portion of panel A.

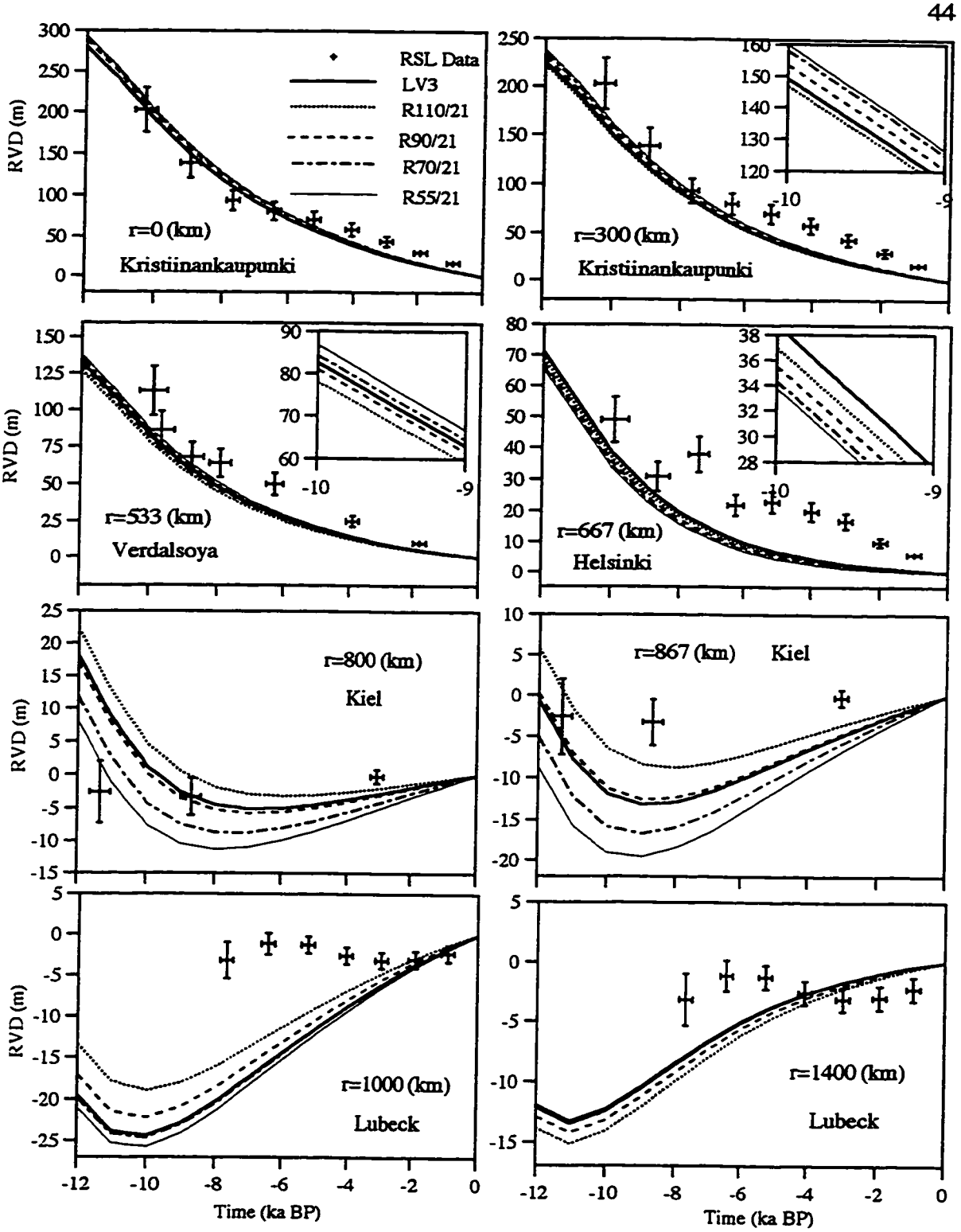

Figure 3.10 Similar to Fig. 3.4 except for model LV3 and reference models R110/21, R90/21, R70/21, and R55/21. Inserts in some panels display portions of the curves in larger scales to reveal sequence of the curves.

3.1.4 Effects of Lateral Variations in both Asthenospheric Viscosity and Lithospheric Thickness

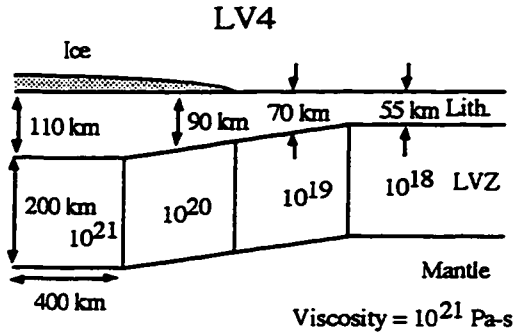

Figure 3.11 Sketch of model LV4 whose lithospheric thickness and LVZ viscosity vary laterally.

In this section, lateral variations of asthenosphere viscosity and lithosphere thickness are considered together. Model LV4 (Fig. 3.11) incorporates models LV1 and LV3 together, therefore contains lateral variations in both lithospheric thickness and asthenospheric viscosity. The variations in asthenospheric thickness (like that in model LV2) are not included in model LV4 because its effects are similar to that of variations in asthenospheric viscosity. The reference models are R110/21, R90/20, R70/19 and R55/18. As before, the mantle below the asthenosphere is considered a viscoelastic half-space.

The computed RVD histories for model LV4 and the reference models are plotted in Fig. 3.12. The curves LV4 and its reference curves in Fig. 3.12 look very similar to the curves LV1 and its reference curves in Fig. 3.4. There are only slight differences between the two figures, such as the RVD curves in the early stage of rebound are less separated in Fig. 3.12 than that in Fig. 3.4. This may be due to lithospheric thinning in LV4 and thinner lithospheres in some of the LV4's reference models. Overall, the effects of lateral variations in model LV4 (Fig. 3.12) are similar to those in model LV1 (Fig. 3.4). Hence, RSL data is able to detect lateral variations in asthenosphere more than in lithosphere. This is especially true for the central area of the load.

In summary, the effects of lateral heterogeneities in asthenospheric properties and lithosphere thickness on postglacial rebound can be detected by comparing RSL observations with predictions from a suite of laterally homogeneous reference models at different locations. However, the inferred asthenospheric viscosity from the comparison may be lower for sites inside the load area and higher outside. False lateral viscosity variations could be obtained if one compares peripheral sites across the load margin. For

the laterally heterogeneous asthenospheric models, there is also a trade-off between the thickness and viscosity which can not be uniquely resolved. In the presence of both lateral lithospheric and asthenospheric heterogeneities, effects of the asthenosphere are larger than that of the lithosphere.

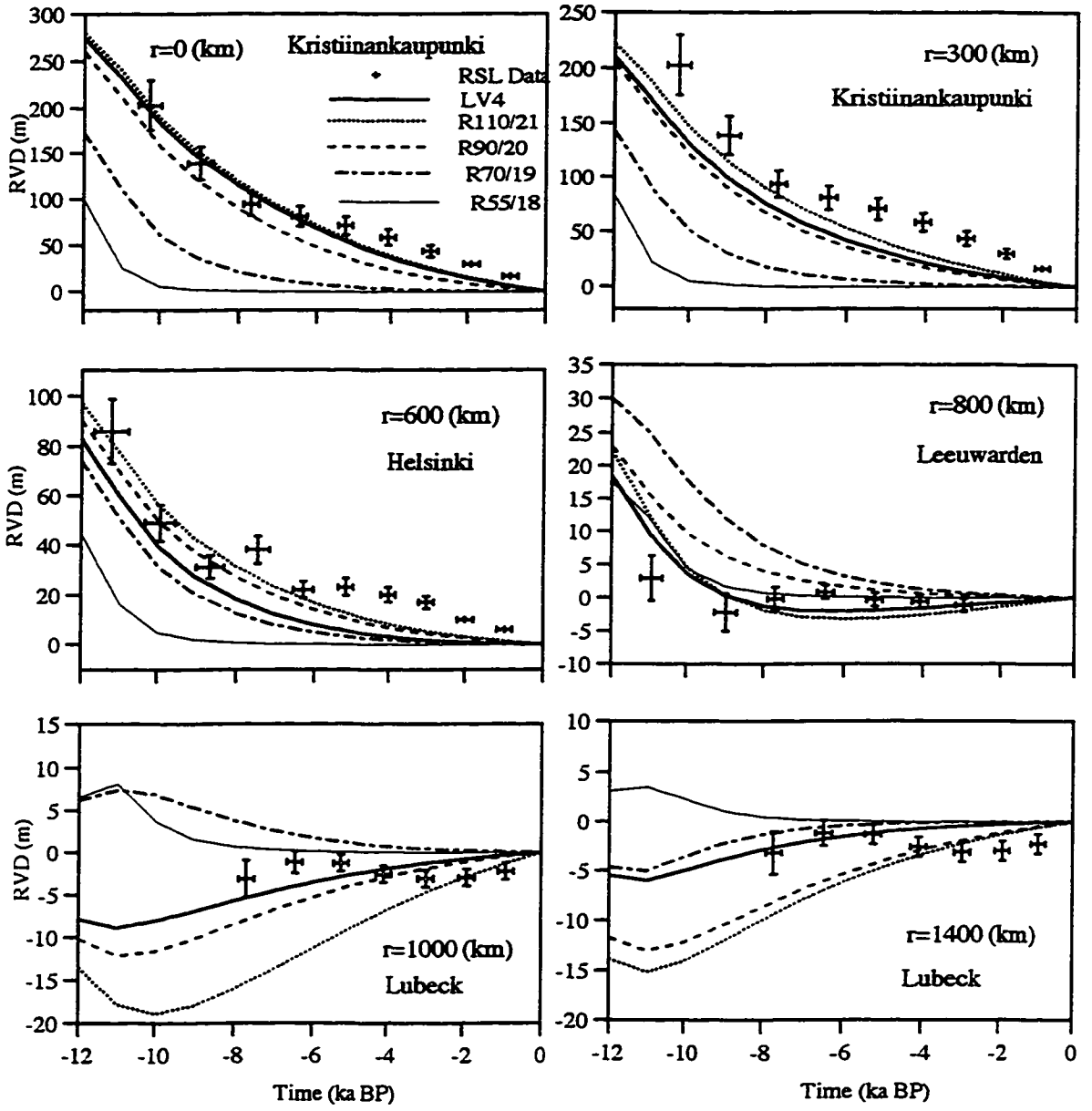

Figure 3.12 Similar to Fig. 3.4 except for model LV4 and reference models R110/21, R90/20, R70/19, and R55/18.

3.2 EFFECTS ON UPLIFT RATE, HORIZONTAL DISPLACEMENT AND VELOCITY, AND GRAVITY

Here, we exam the effects of lateral heterogeneities on other geodetic quantities. Throughout this section, the effects are considered to be significant if differences in the geodetic quantities are larger than the observational uncertainties. We adopt conservative error bounds of 5 m for horizontal displacements during the last 12 ka, 1 mm/a for vertical and horizontal velocities, and 1 mGal for gravity anomalies.

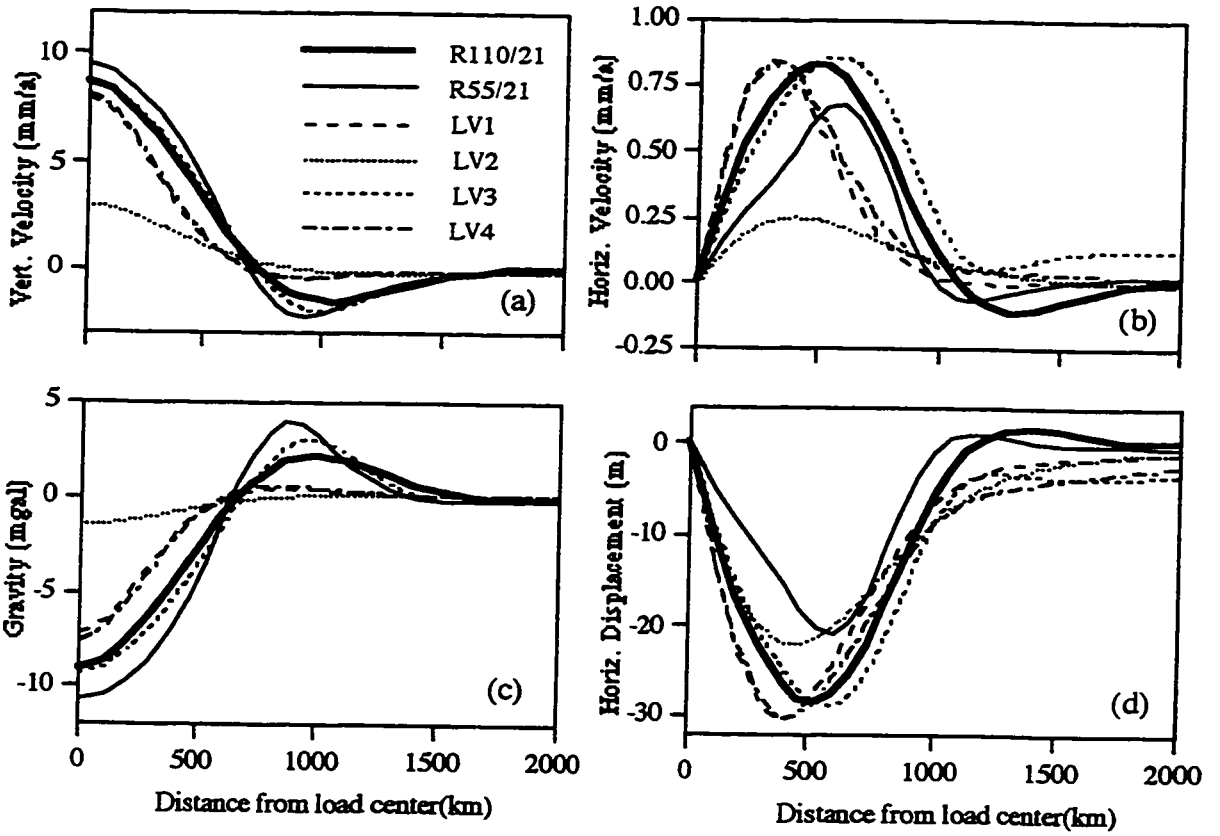

Figure 3.13 Present-day vertical (a) and horizontal (b) velocities, gravity anomalies (c) and horizontal displacements (d) at 10 ka BP as a function of distance from the load center.

Profiles of present-day vertical (a) and horizontal (b) velocities, gravity anomalies (c), and horizontal displacement at 10 ka BP (d) for all the laterally heterogeneous models LV1, 2,

3, and 4 and two reference models R110/21 and R55/21 are plotted in Fig. 3.13. These geodetic quantities complement the RVD curves on characterizing postglacial deformation. In previous investigations, the emphasis was on the relative vertical displacement (with respect to the present-day displacement) rather than on the absolute vertical displacement. This is because RVD is comparable with RSL observations while the absolute vertical displacement is not. Here, gravity anomaly is derived from the vertical displacement by simply multiplying the presently remaining uplift (i.e. present-day displacement) with a constant 0.19 mGal/m (Gasperini et al., 1991). Since RSL data reflect the amount of vertical displacement that has taken place and gravity anomalies measures the amount of displacement that will occur in the future, they complement each other. The present-day vertical velocity also complements the RVD by providing its observable time derivative.

Inspection of Fig. 3.13a & c confirms results of the previous section: for the laterally heterogeneous lithospheric model (LV3), the vertical velocity and gravity curves are closer to those for the reference model R110/21 underneath the load but are closer to model R55/21 for distances greater than 1000 km from the load center (Fig. 3.13a & c). This confirms that postglacial deformation at a site is sensitive to the local thickness of the lithosphere. The differences between models LV1 and LV4 are also small (Fig. 3.13), but both models differ significantly from models R110/21 and LV3. This confirms that lateral asthenospheric variations are more important than lateral lithospheric variations.

The vertical velocity and gravity curves for model LV2 are widely separated from those for models LV1 and LV4 at the center where they have different asthenospheric viscosity underneath (10^{19} Pa-s in LV2 vs. 10^{21} Pa-s in LV1 and 4) and come together at around r=1000 where they have the same asthenospheric viscosity underneath (Fig. 3.13a & c). This confirms that postglacial deformation at a site is sensitive to local asthenospheric viscosity and the rebound curves change laterally according to the lateral variations in the models' properties.

Besides confirming what have been learned, Fig. 3.13 a and c also show that the vertical velocity and gravity at the center of the load, for the laterally heterogeneous models LV1 and LV4, are clearly distinct from those for reference models R110/21 and R55/21. This, however, is not the case for the RVD curves. Hence, the gravity (or vertical displacement) at the center is affected by the low-viscosity part of the asthenosphere outside the center

area for models LV1 and LV4 while the RVD is only affected by the viscosity right beneath the center.

The horizontal displacements at 10 ka BP experience a minimum at around 500-600 km for both reference models (Fig. 3.13d). However, the amplitude of the oceanic reference model R55/21 is reduced by about 30 per cent. Thus, a thinner lithosphere generally results in a smaller horizontal displacement. Comparing to model R110/21, the minimum in horizontal displacement for model LV1 shifts about 150 km towards the load center and has a slightly increased amplitude. The differences between the horizontal displacements of models R110/21 and LV1 are generally larger than 5 m and thus detectable. For model LV2 with lower asthenospheric viscosity beneath the center of the load, amplitude of the minimum decreases to two-third of that for model LV1. Also, the response for model LV3 inside the load is in close agreement with that for the reference model R110/21 since both models share the same thick lithosphere near the center.

Similar observations can also be made for horizontal velocities (Fig. 3.13b): Here, the reference model with thin lithosphere (model R55/21) experiences smaller horizontal velocities than the thick continental reference model. Both laterally heterogeneous models LV2 and LV3 have a similar response and a shifted pattern in horizontal velocity compared to models R110/21 and R55/21.

Comparing to the vertical responses that are least sensitive to the models' properties in the inner peripheral area around r=700 km (see curve crossings in Figs. 3.12 a & c, Figs. 3.4 & 3.8), the horizontal quantities appear to be most sensitive in the area around r=500 km (Fig. 3.13 b & d). Although amplitudes of these horizontal quantities are only about one tenth of their vertical counterparts (comparing Fig. 3.13 b with a and Fig. 3.13 d with Fig. 3.5 or 3.8), with the trend of increasing precision from VLBI and GPS observations, horizontal motions of the postglacial adjustment process will become useful in resolving lateral heterogeneities in the future.

Summarizing the effects of lateral variations in the lithosphere and asthenosphere, which can be regarded as simple approximations to the rheological variation across a continental margin, we conclude that:

(1) Lateral heterogeneities can significantly influence the predicted RSL, velocities, horizontal displacement, and gravity inside and around former glaciated areas.

(2) Measurements of vertical motion of postglacial rebound (RSL, gravity, and vertical velocity) in the inner peripheral area of former glaciers are least sensitive to lateral heterogeneities whereas measurements of horizontal motion (horizontal displacement and velocity) are most sensitive there.

(3) Lateral heterogeneities can be resolved from spatial-time patterns of RSL and other geodetic signatures.

(4) Lateral variations in the asthenosphere have much more significant effects on geodetic signatures than lateral lithospheric thickness variations.

CHAPTER 4

TWO DIMENSIONAL FINITE ELEMENT RESULTS PART 2: EFFECTS OF LATERAL HETEROGENEITIES IN LOWER MANTLE AND DENSITY ON POSTGLACIAL REBOUND

In this chapter, we explore the effects of lateral viscosity variations in the lower mantle and the effects of lateral density variations on postglacial rebound observations. The same cylindrical finite element grid and the disc load model are used as in the previous chapter, except where stated otherwise.

4.1 EFFECTS OF LATERAL VISCOSITY VARIATIONS IN THE LOWER MANTLE

Seismic tomography shows that lateral heterogeneities in the upmost 400 km are large and there is general agreement among different studies on the magnitude and location of the structures. However, lateral variations in the lower mantle are generally small except near the core-mantle boundary (Su et al., 1994), and there is a lack of consensus on structures beneath 400 km. This may be partly due to the difference in resolving power of the various studies at such great depth. In the following, we would like to investigate if lateral viscosity variations in the lower mantle can have measurable effects on postglacial rebound. If the answer turns out to be positive, then the postglacial rebound observations may be useful for constraining the lateral variations in the lower mantle in future study.

In the following experiments, the effects of lateral heterogeneity in the lower mantle have been tested for the ice loads with sizes comparable to the Fennoscandia Ice Sheet (disc radius = 800 km) and the Laurentide Ice Sheet (disc radius = 1600 km), respectively.

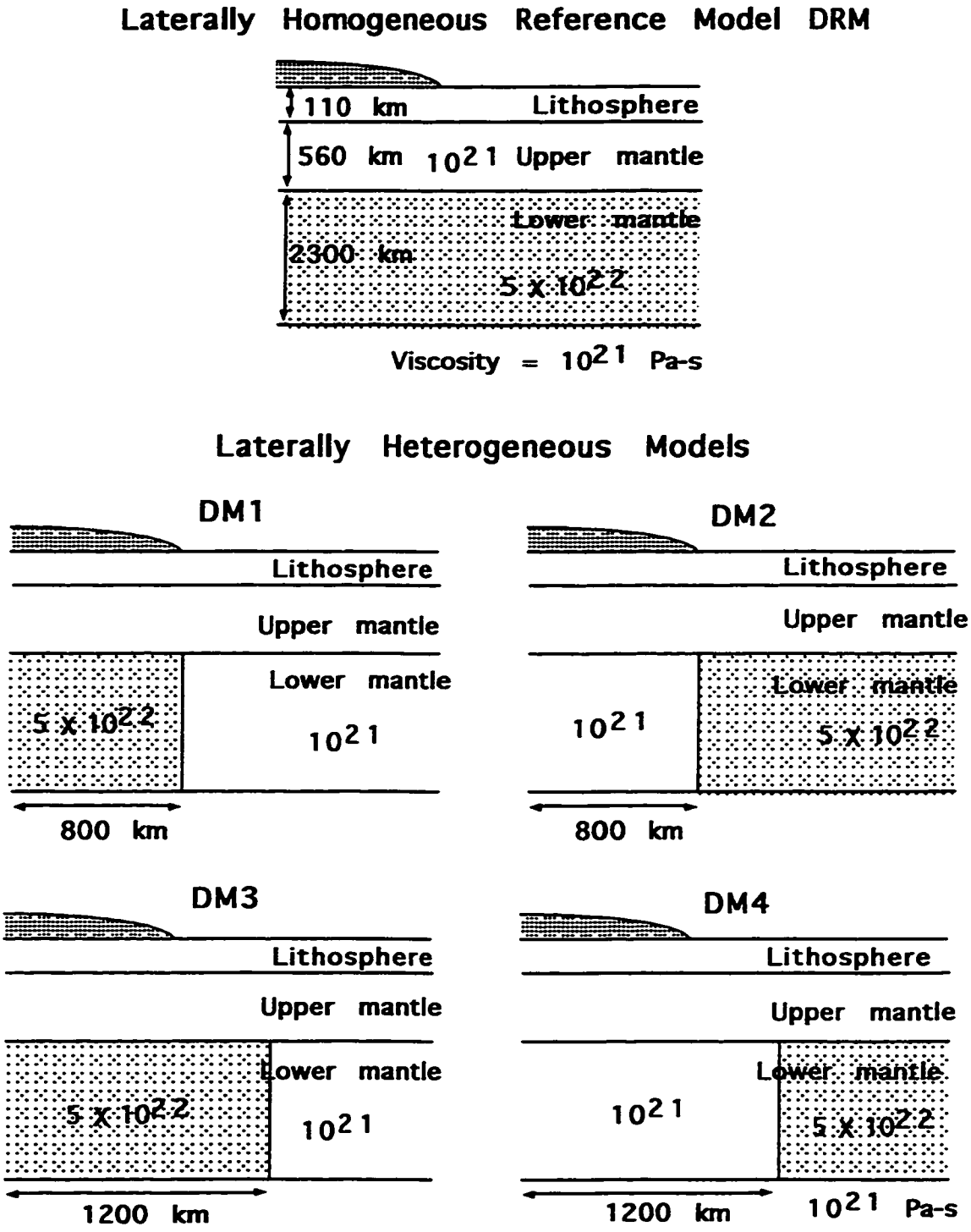

Figure 4.1 Sketches of laterally homogeneous reference models R110/21 and DRM and earth models with laterally heterogeneous lower mantle DM1, 2, 3, and 4.

First let us consider the smaller ice load which is the same as the one used in the previous chapter. All the earth models (sketched in Fig. 4.1) have a 110 km thick lithosphere overlying a 10^{21} Pa-s upper mantle. One laterally homogenous reference model is the R110/21 while the other is model DRM that has a $5x10^{22}$ Pa-s lower mantle. In the lower mantle of the four laterally heterogeneous models DM1, DM2, DM3 and DM4, the viscosity is assumed to be depth independent and varies laterally across one vertical boundary only. Models DM1 and DM3 have a high viscosity ($5x10^{22}$ Pa-s) lower mantle under the load, while DM2 and DM4 have a $1x10^{21}$ Pa-s lower mantle beneath the load. The difference between DM1 and DM3 is the location of the viscosity contrast. The viscosity contrasts for models DM1 and DM2 are at r = 800 km (under the load margin) and at r = 1200 km for models DM3 and DM4. The elastic parameters and density of these models are same as those for model R110/21.

RVD histories at a number of locations are plotted in Fig. 4.2. For sites within r = 600 km, the curves of all heterogeneous models first follow those for model R110/21 and then approach those for model DRM. Therefore, the deformations of the laterally heterogeneous models are firstly dominated by relaxation of the less viscous part of the mantle, then taken over by the relaxation of the more viscous part of the mantle. However, the differences among RVD curves for the laterally heterogeneous models are small and are not resolvable by the uncertainties of the RSL data.

The effect of the lateral extent of the higher viscosity region under the load is small and hardly detectable (DM1 vs. DM3 in Fig. 4.2). But, the effect of the lateral extent of the low viscosity region under the load is large enough to be detected at r = 800 km (DM2 vs. DM4 in Fig. 4.2) in early stage of the postglacial rebound (before 7 ka BP). In general, the effects of the lateral variations of viscosity in the lower mantle may not be detectable by RSL data in Fennoscandia or where the size of the ice load was smaller than 800 km in radius. This confirms that such loads have little resolving power to the lower mantle (Mitrovica, 1996).

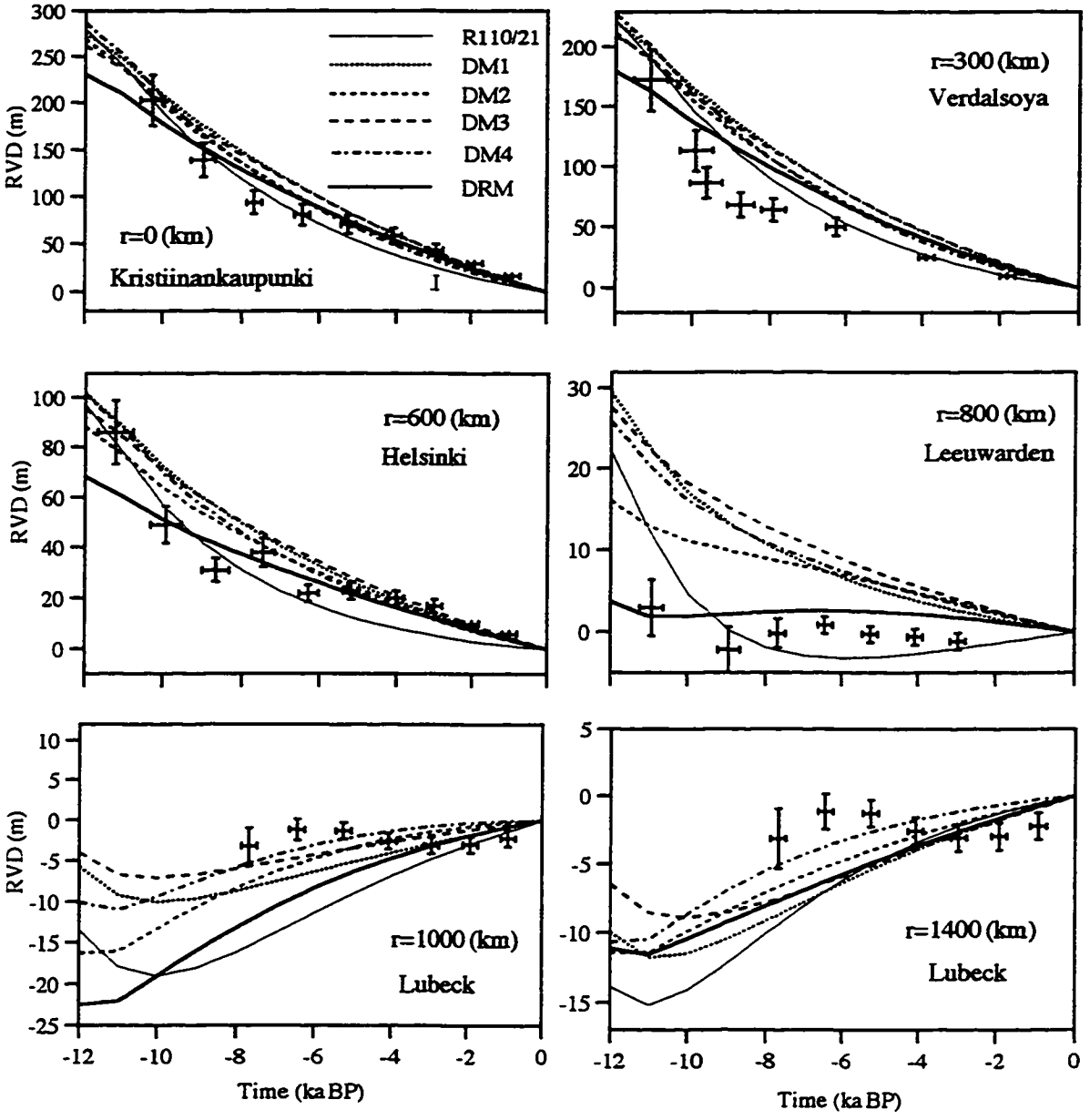

Figure 4.2 Similar to Fig. 3.4 except for models DM1, DM2, DM3, and DM4, and reference models DRM and R110/21.

Next, we consider the larger ice load with size comparable to the Laurentide Ice Sheet. The radius and maximum height of the parabolic disc load are increased to 1600 km and 3500 meters, respectively, while the glacial history remains the same as before (Fig. 2.1). Radial dimension of the earth models is also increased proportionally to form new models: R110/21L, DML1, DML2, DML3, DML4, and DRML. They are named after their predecessors with the suffix "L" to indicate the larger dimension of the ice load. The locations of the viscosity contrasts are at r=1600 km for models DML1 and DML2 and at r=2400 km for models DML3 and DML4.

RVD history curves for the new models (Fig. 4.3) show much more separation than that for the previous ones. For sites inside the load area (r =0, 800, 1200 km), the RVD curves also show decreasing curvatures as the low viscosity regions ($1x10^{21}$ Pa-s) beneath the load in model R110/21L gets progressively replaced by regions of higher viscosity (DML4 to DML2) or as the regions of high viscosity beneath the load get larger (from DML1 to DML3 and finally to DRML). Comparing the difference between these RVD curves and the uncertainties of the data near the center of rebound in Fig. 4.3, we see that lateral viscosity variations at r=1600 km affect postglacial rebound at r=0 km more than that at r=2400 km.

At marginal site r=1600, the RVD curves are also very sensitive to lateral viscosity variations in the lower mantle. As the high viscosity region beneath the load in model DRML becomes progressively replaced by the region of lower viscosity that comes closer and closer to the center of rebound (DML3 to DML1), prediction of land submergence changes to land emergence and then to submergence again at r=1600 km. As the region of low viscosity gets broader (from DML2 to DML4 and finally to R110/21L), land emergence again changes to land submergence. Thus, RSL curves at r=1600 km are sensitive to the presence of a lateral viscosity contrast more than 800 km away. At r=2400 km and 2800 km, the RVD curves between most of the different viscosity variations in the lower mantle can also be resolved by the observations.

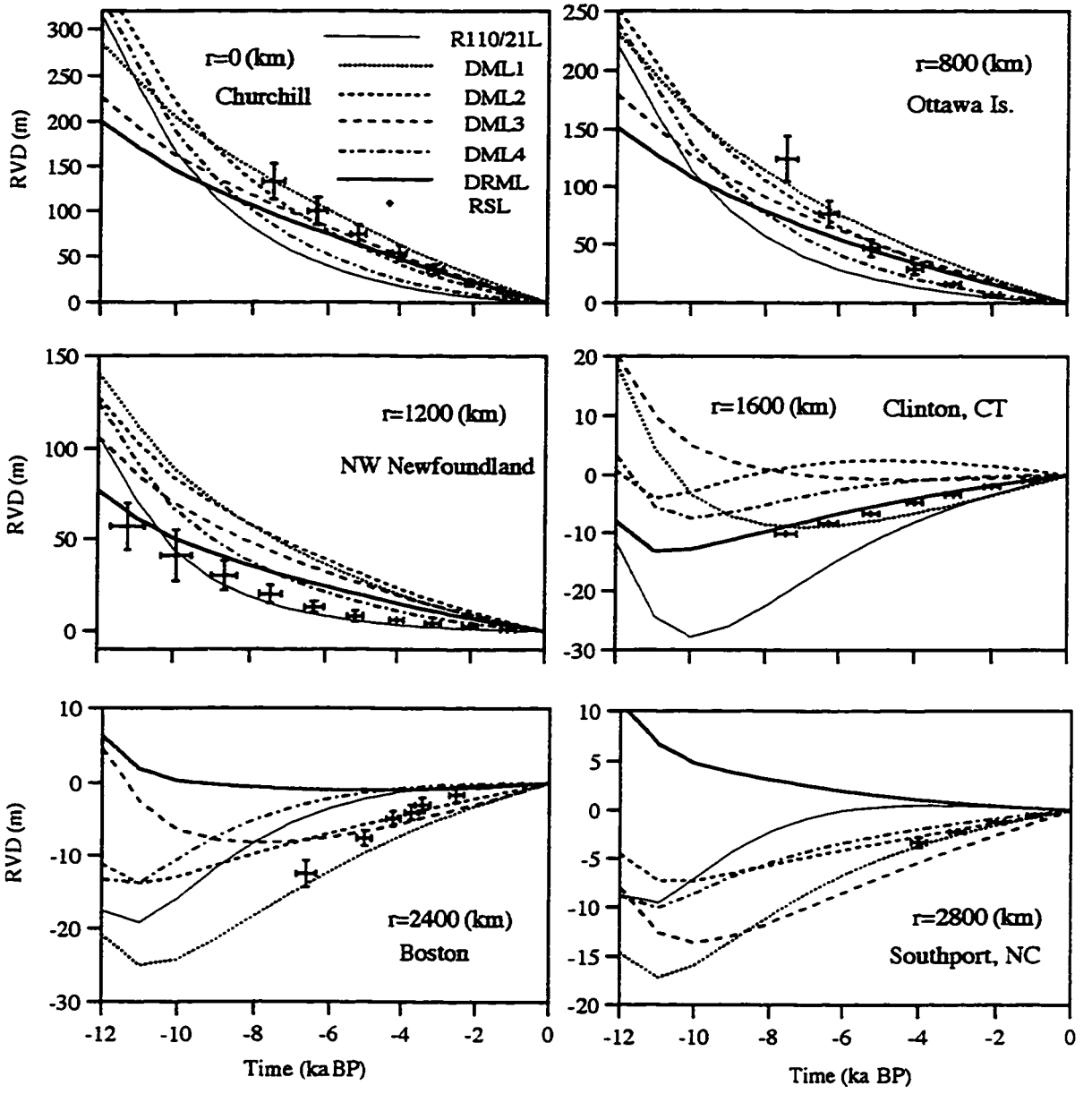

Figure 4.3 Similar to Fig. 3.4 except for models DML1, DML2, DML3, and DML4, and reference modelsDRML and R110/21L. RSL data are at sites in North America.

In summary, the effects of lateral viscosity variations in the lower mantle for an ice load with size comparable to the Laurentide Ice Sheet are large and resolvable by spatial variation of the RSL observations for sites from the center to outer peripheral area. However, the effects of lateral heterogeneity in the lower mantle can be neglected for an ice load with size comparable to or smaller than the Fennoscandia Ice Sheet.

4.2 EFFECTS OF LATERAL DENSITY VARIATIONS

Although postglacial rebound is driven by buoyancy force (and impeded by viscosity), only lateral viscosity variations have been considered so far. Density is usually assumed to be laterally homogeneous although lateral density variations are likely as significant as viscosity.

Lateral density variations can arise from thermal effects, chemical composition, or both. For example, the effect of temperature on density for olivine at a constant pressure can be estimated from the volume expansivity of α given by (Anderson, 1989):

$$\frac{1}{\rho}\left(\frac{\partial \rho}{\partial T}\right)_p = -\frac{1}{V}\left(\frac{\partial V}{\partial T}\right)_p = -\alpha = -5.2 \times 10^{-5} / {}^{\circ}K \qquad (4.2.1)$$

A temperature difference of 600 °K can decrease density by about 3%. On the other hand, it is well known that densities in the continental crust are significantly different than those in the oceanic crust due to differences in composition. For example, granitic and granodioritic rocks in the continental crust have average densities of 2640 and 2730 kg/m^3, respectively, whereas basalts and lherzolites (Oxburgh, 1980) beneath the oceans have average densities close to 3000 and 3360 kg/m^3, respectively. This represents a lateral density variation of more than 10%.

Further, both the relaxation time and the amplitude of rebound depend on the buoyancy force or the density contrasts (e.g. Wu & Ni, 1996; Appendix of Wu, 1993). For example, the characteristic relaxation time (T) for a self-gravitating and homogeneous Maxwell sphere at an angular order n is a function of density ρ, viscosity ν, rigidity μ, gravity g, and earth radius a:

$$T = \frac{\nu}{\mu} + \frac{2n^2 + 4n + 3}{na\rho g}\nu \qquad (4.2.2).$$

In this equation, T is made of two parts. The first part (ν / μ) is the Maxwell time and the second part ($\frac{2n^2 + 4n + 3}{na\rho g}\nu$) represents the ratio of viscosity over the buoyancy force. This latter part reflects the balance between the impeding force and the driving force in postglacial rebound. Thus, an increase in density results in an increase in the buoyancy force which speeds up the rebound process. (In fact, the second part of the T is inversely proportional to the square of density because of the gravity g.) The strength of excitation of the uniform sphere is also dependent on density as shown in the following expression ($\frac{r^h}{s}$):

$$\frac{r^h}{s} = \frac{1}{3}\frac{(2n+1)}{1 + \frac{na\rho g_o}{(2n^2 + 4n + 3)\mu}} \qquad (4.2.3)$$

Furthermore, for a spherically stratified viscoelastic earth model, a discontinuity in density introduces a major gravitational relaxation mode (except when associated with an elastic lithosphere) while a discontinuity in the Maxwell time $\frac{\nu}{\mu}$ only adds two transitional modes whose contribution to the total rebound is usually small (see chapter 6).

Thus, we wish to quantify the effect of lateral density variations for an earth model with a thick low density continental root .

The earth models used to study the effect of lateral density variations are shown in Fig. 4.4. Models LV5 and LV6 have the same viscosity and elastic structure as reference model R110/21. The difference is that in model R110/21 the density is constant, while model LV5 has a 420 km thick low density root beneath the load and model LV6 has an infinitely thick low density root. The viscosity structure of model LV7 is the same as that in model LV4, however the density structure in model LV7 varies both vertically and laterally in the continental root and neighboring areas whereas the density in model LV4 is constant. The ice model is the same as that in the previous chapter.

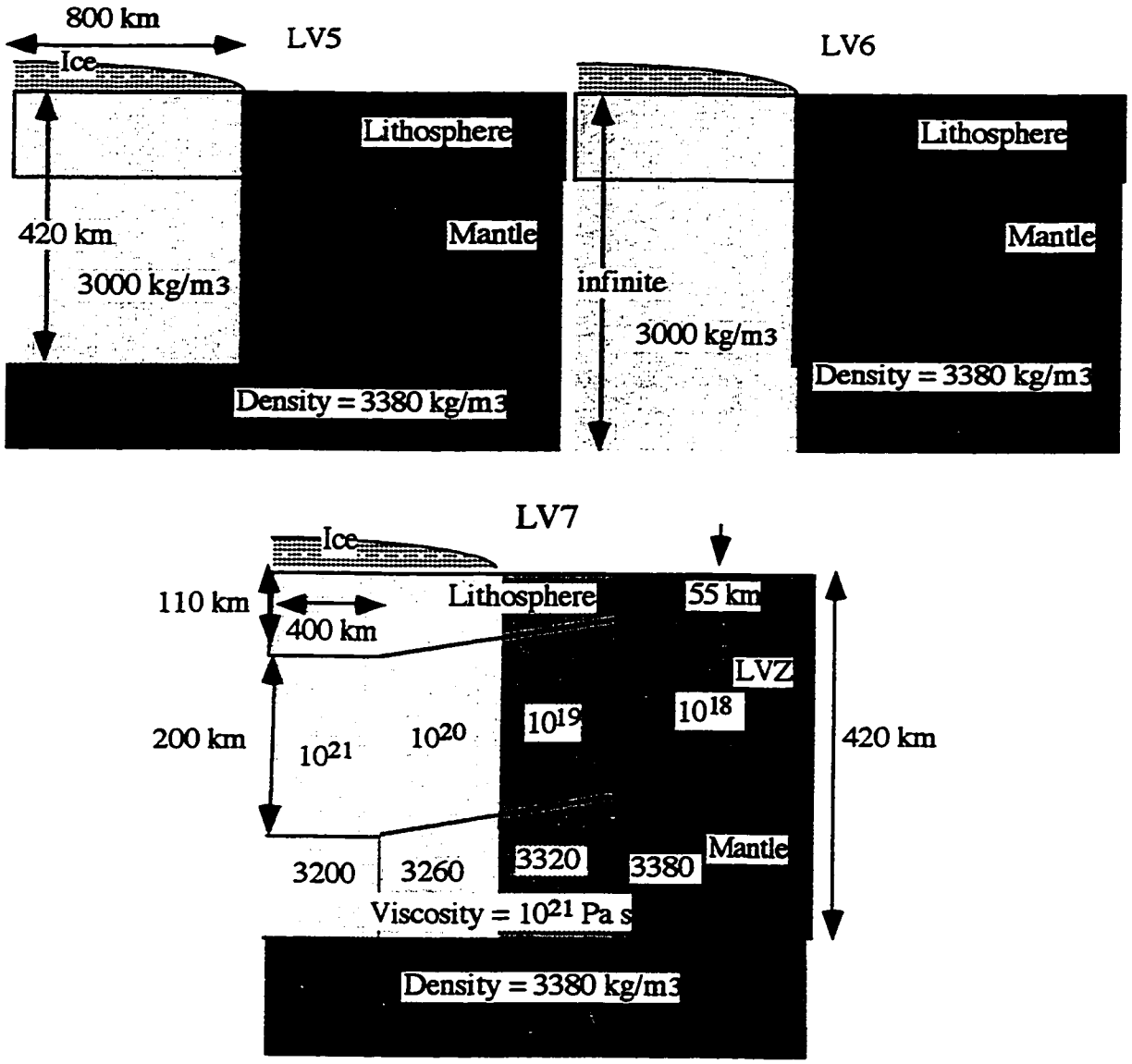

Figure 4.4 Sketches of earth models with lateral density variations.

RVD curves for models LV5, LV6, LV7, R110/21 and LV4 are compared in Fig. 4.5 while the other geodetic signatures are compared in Fig. 4.6. Here, a low density root as proposed by models LV5 and LV6 generally results in larger RVD predictions and longer relaxation times due to the smaller buoyancy force underneath the load when compared to the reference model R110/21. However, differences in RVD predictions are too small to

be resolved by observations. The same conclusion can be drawn from a comparison of models LV4 and LV7, here the additional low-density root in model LV7 results only in small differences in RVD predictions, especially at r=1000 km (Fig. 4.5d).

A comparison of horizontal displacements and velocities for models R110/21, LV5, and LV6 (Fig. 4.6) reveals that the effects of a 420 km thick low density root is too small to be resolved by the data. Although an infinitely thick low density root gives larger differences in horizontal displacements and velocities, model LV6 is still not resolvable from model R110/21. Figs. 4.6a & c show that larger differences are predicted for the vertical uplift rate and gravity anomalies. Thus, assuming that the observational uncertainties of vertical velocity and gravity anomalies are 1 mm/s and 1 mGal respectively, a 420 km thick low density root has observable effects on these data.

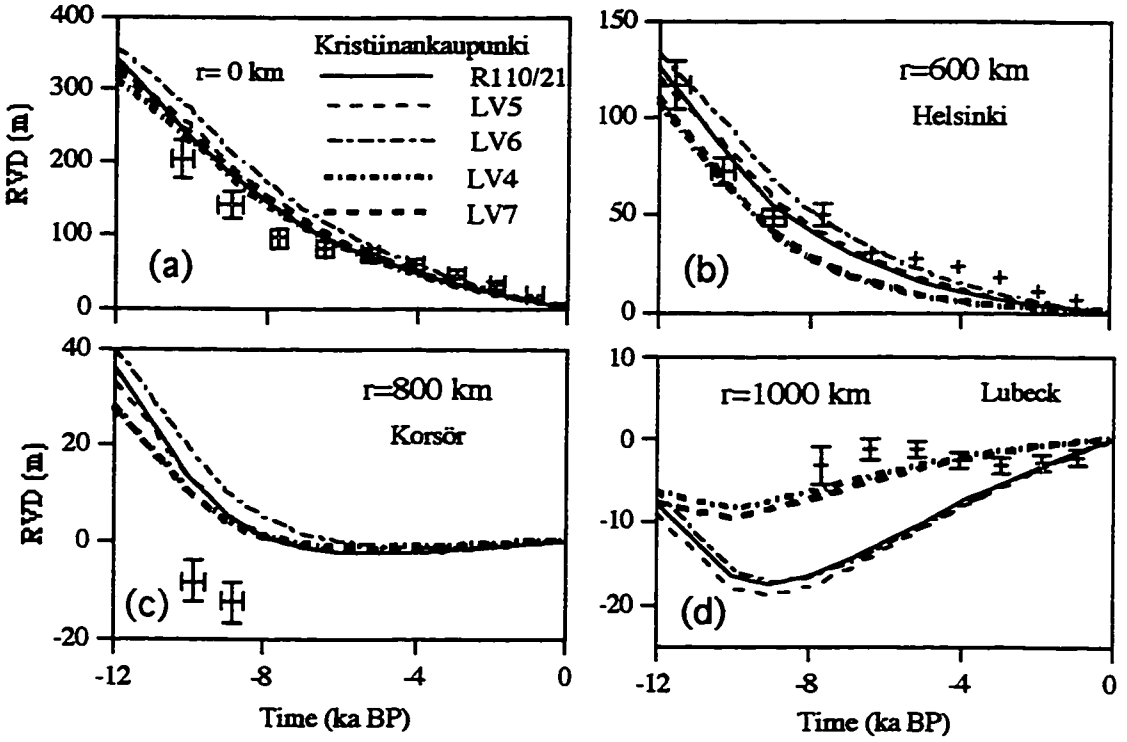

Figure 4.5 Similar to Fig. 3.4 except for models LV5, LV6, LV4, and LV7 and reference model R110/21.

Similar conclusions can be drawn from a comparison of the responses of models LV4 and LV7. Figs. 4.6b & d show that horizontal displacements and velocities for these models almost lie on top of each other but the difference in gravity anomaly (Fig. 4.6c) is large

enough to be resolved. However, Fig. 4.6a shows that the difference in the vertical velocities predicted by LV4 & LV7 are less than 1 mm/a and thus not resolvable.

In summary, we have shown that a low density continental root generally has little effect on RVD and horizontal motions, however its effect on gravity is detectable given that the Pleistocene ice history is known.

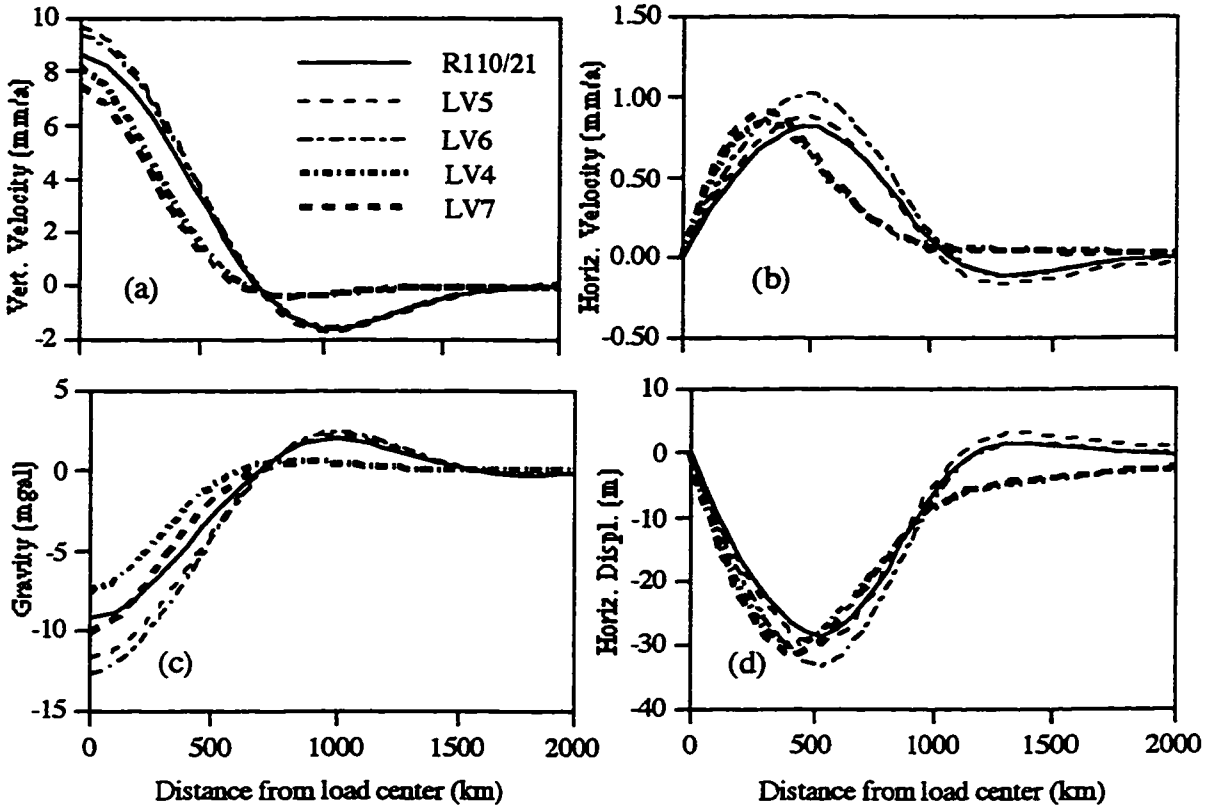

Figure 4.6 Present-day vertical (a) and horizontal (b) velocities, gravity anomalies (c) and horizontal displacements at 10 ka BP as a function of distance from the load center for models LV5, LV6, LV4, and LV7 and reference model R110/21.

CHAPTER 5

THREE DIMENSIONAL FINITE ELEMENT RESULTS

All previous laterally heterogeneous earth models were axisymmetric. However, it is not clear whether (1) axisymmetry constitutes a favorable condition for the effects of lateral heterogeneities; (2) what the effects of non-axisymmetric lateral heterogeneities on postglacial rebound are; and (3) how applicable simple earth models are to interpretation of RSL data in terms of lateral heterogeneity. Questions 1 and 2 are explored in sections 5.1 and 5.2 respectively, using the 3D finite element grid and the approximate disk load described in the chapter two. Question 3 is dealt with in section 5.3, using a more realistic laterally heterogeneous earth model with a realistic ice history - the Ice-3G model of Tushingham and Peltier (1991). Lateral heterogeneities considered here are limited in lithosphere or/and asthenosphere overlying a uniform Maxwell halfspace of 10^{21} Pa-s. Density and elastic parameters of most of the models are the same as that of model R110/21, except where stated otherwise.

5.1 AXISYMMETRY VS. NON-AXISYMMETRY

The reason for asking question 1 is that there is a previous example shows that different model geometry may result in different conclusions: In computing deformation for channel models with power-law rheology, Wu (1992a) found no RSL-transition zone if the 2D load has the third dimension extending to infinity but a prominent RSL-transition zone if the 2D load is axially symmetric (Wu, 1993).

Here, our concern is illustrated in map views of models LITH_CS and LITH_AE in Fig. 5.1. Each of the two models has laterally heterogeneous lithosphere overlying on a uniform Maxwell halfspace with a mantle viscosity of 10^{21} Pa-s (also see cross-sections and 3D views in Fig. 5.2). Model LITH_CS is a typical axisymmetric one whose lithospheric thickness under the disk load is 150 km in contrast to 50 km under area outside

the load. On the other hand, model LITH_AE is not axisymmetric and its lithosphere is divided into two parts by a straight line which represents a vertical plane in 3D. Each part has a different thickness (either 150 km or 50 km) with the disk load sitting on the thicker part of the lithosphere. Our concern is whether the deformation along the line OB in model LITH_CS is much different from that in model LITH_AE.

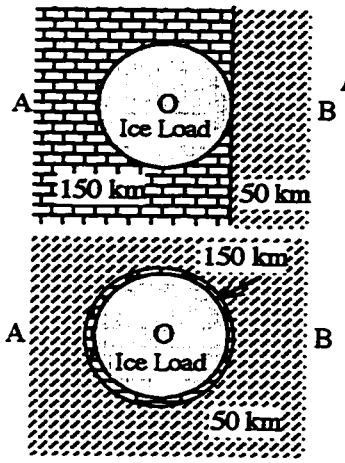

Figure 5.1 Map views of central portions of models LITH_CS and LITH_AE. Both models are laterally heterogeneous with a change in lithospheric thickness from 150 km to 50 km. See Fig. 5.2 for their 3D views and cross-sections.

Two time sanp shots of vertical displacement profiles at present and 10 ka BP are shown in Fig. 5.3 for the models LITH_CS and LITH_AE (along with models LITH_AM, LITH_150, and LITH_50 that will be discussed later). The profiles go from point A where x is negative, through the centre of the load O (where x=0), to point B where x is positive. Predicted RVD curves at selected localities x=0 km, $\pm 600km$, $\pm 800km$, and $\pm 1000km$ are plotted in Fig. 5.4. Comparing models LITH_CS (chain line) and LITH_AE (dash line) along the line OB in Figs. 5.3 and 5.4, their displacement profiles are close together (Fig. 5.3), so are their RVD curves (Fig. 5.4) at sites with ($x \geq 0$). The differences between RVD of the two models are not resolvable by uncertainties of the RSL data. Therefore, the effect of axisymmetry is small in this case.

We shall see this is also true for lateral variations in asthenospheric viscosity. In map view, models ASTH_CS and ASTH_AE (Fig. 5.5) look similar to their lithospheric counterparts LITH_CS and LITH_AE (Fig. 5.1), except the lateral variations are in asthenospheric viscosity. Models ASTH_CS and ASTH_AE (Fig. 5.5) have a high viscosity asthenospheric zone (10^{21} Pa-s) in contrast to a low viscosity asthenospheric zone (10^{20} Pa-s), with the disk load sitting above the high viscosity zone. The low viscosity zone (LVZ) is 200 km thick. Above and beneath the asthenosphere are a uniform 110 km thick lithosphere and a Maxwell halfspace of 10^{21} Pa-s, respectively. Comparison of displacements (Fig. 5.6) and RVD (Fig. 5.7) between models ASTH_CS (chain line) and

ASTH_AE (dash line) along the line OB confirms that the effects of axisymmetry are small. Hence, the axisymmetry does not constitutes a favorable condition for the effects of the lateral heterogeneities.

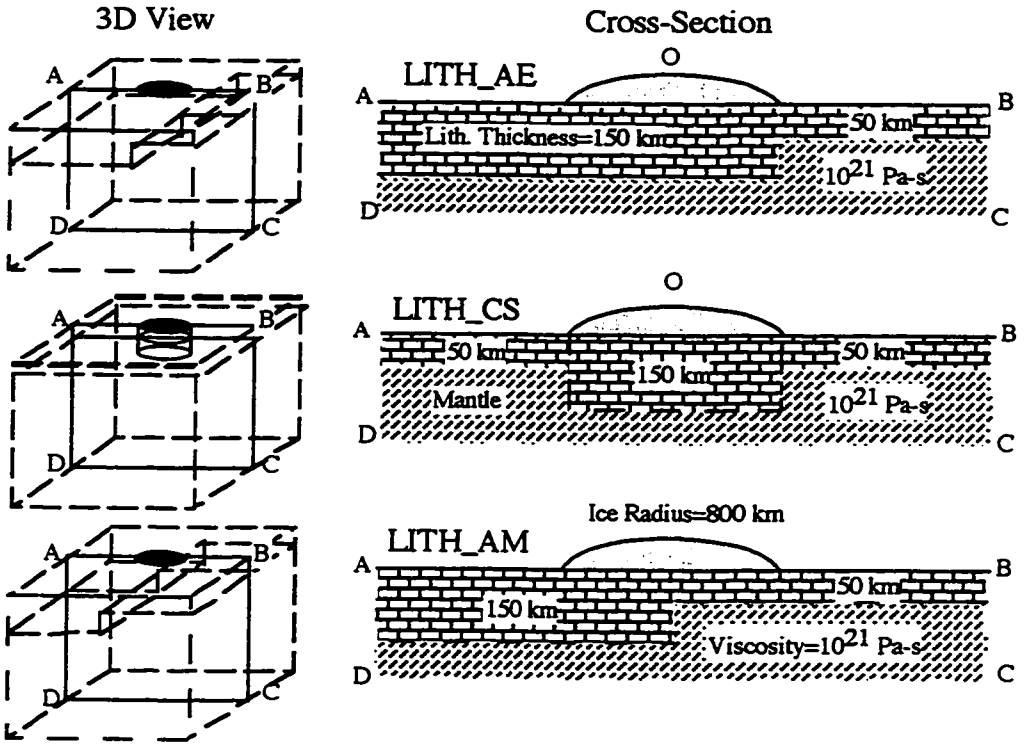

Figure 5.2 Three-dimensional and laterally heterogeneous models with a change in lithospheric thickness: LITH_AE, LITH_CS, and LITH_AM.

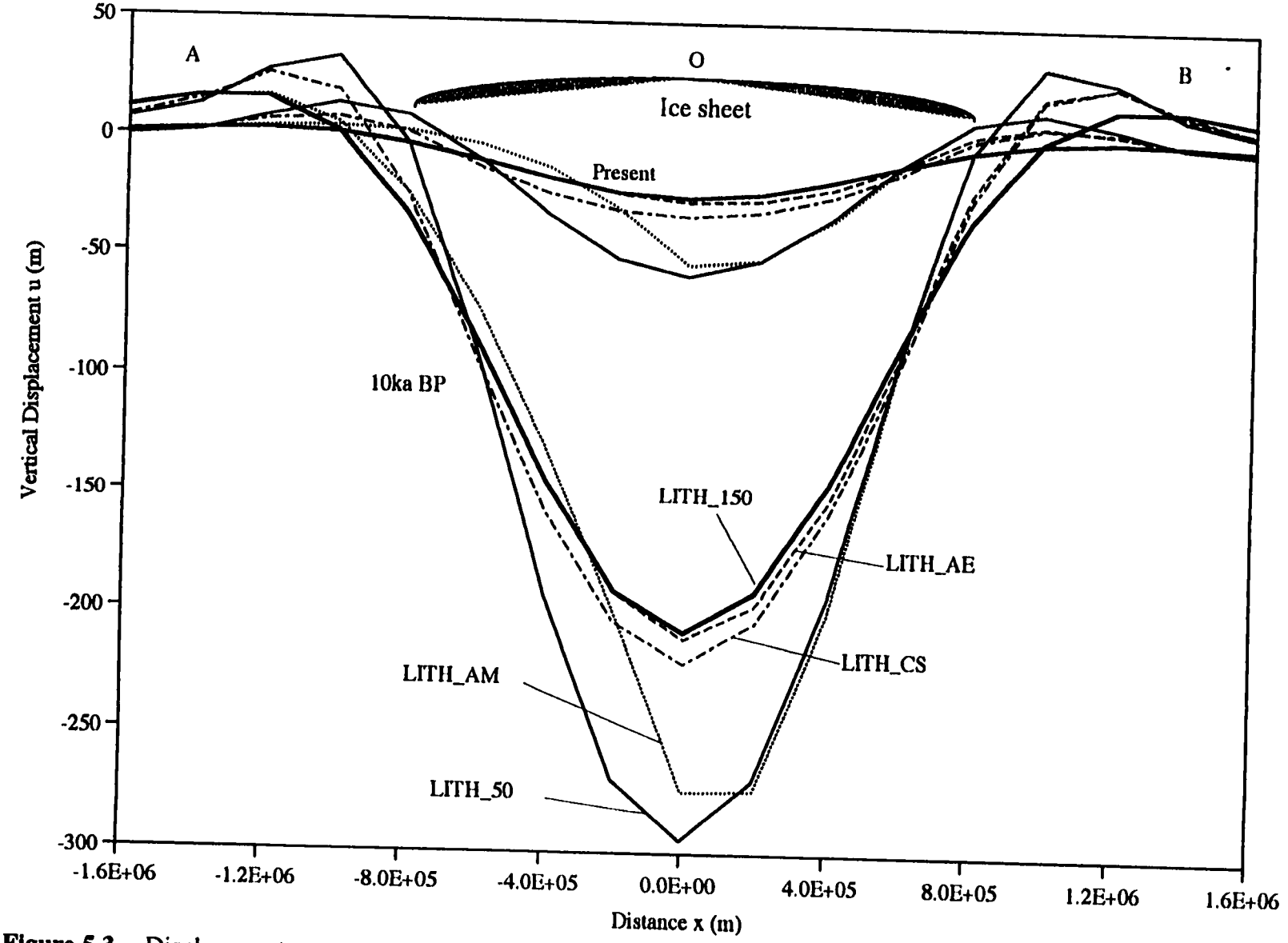

Figure 5.3 Displacement curves at present and 10 ka BP computed for models LITH_AE, LITH_CS, and LITH_AM.

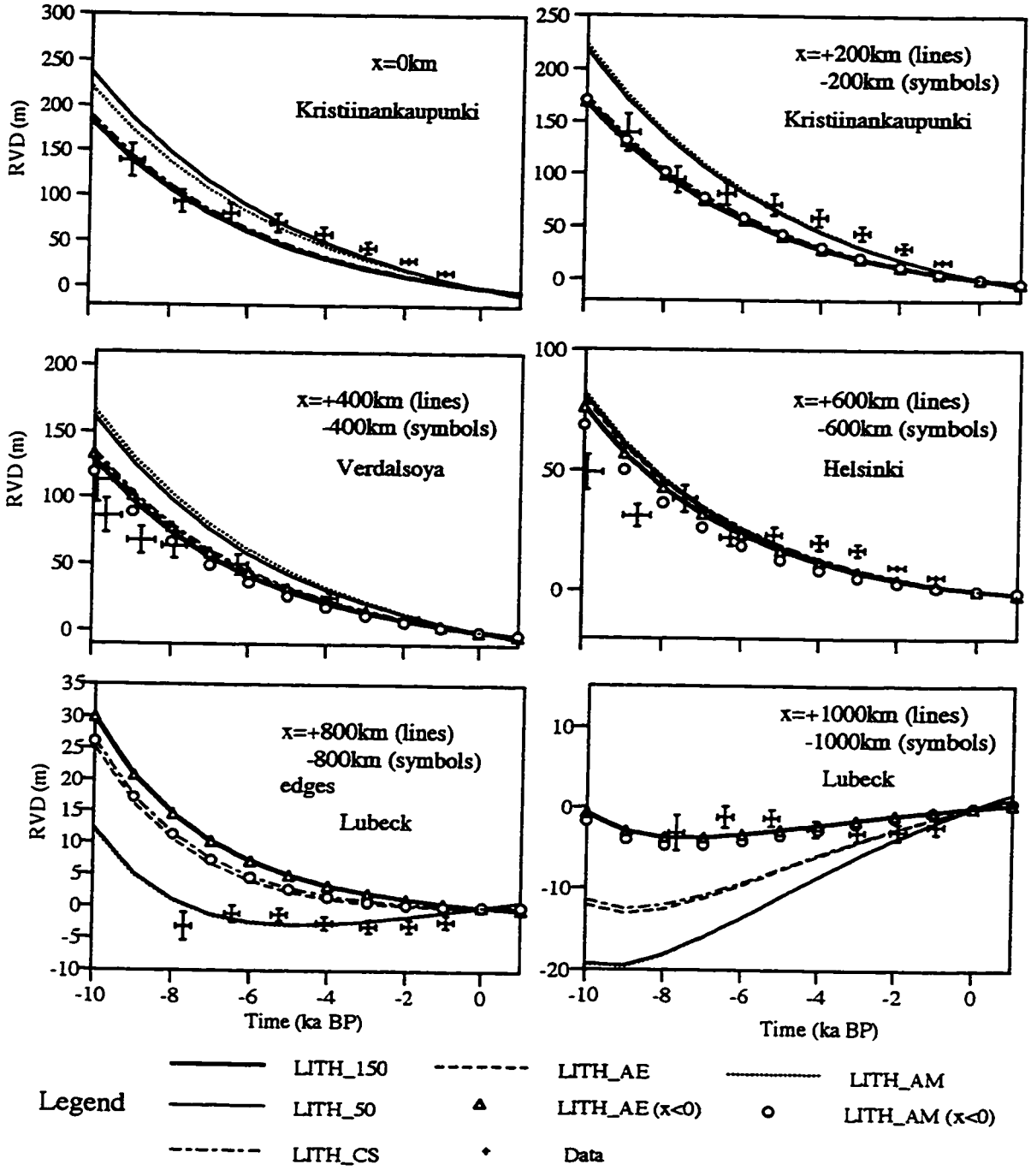

Figure 5.4 Similar to Fig. 3.4 except for models LITH_AE, LITH_CS, and LITH_AMand reference models LITH_150 and LITH_50.

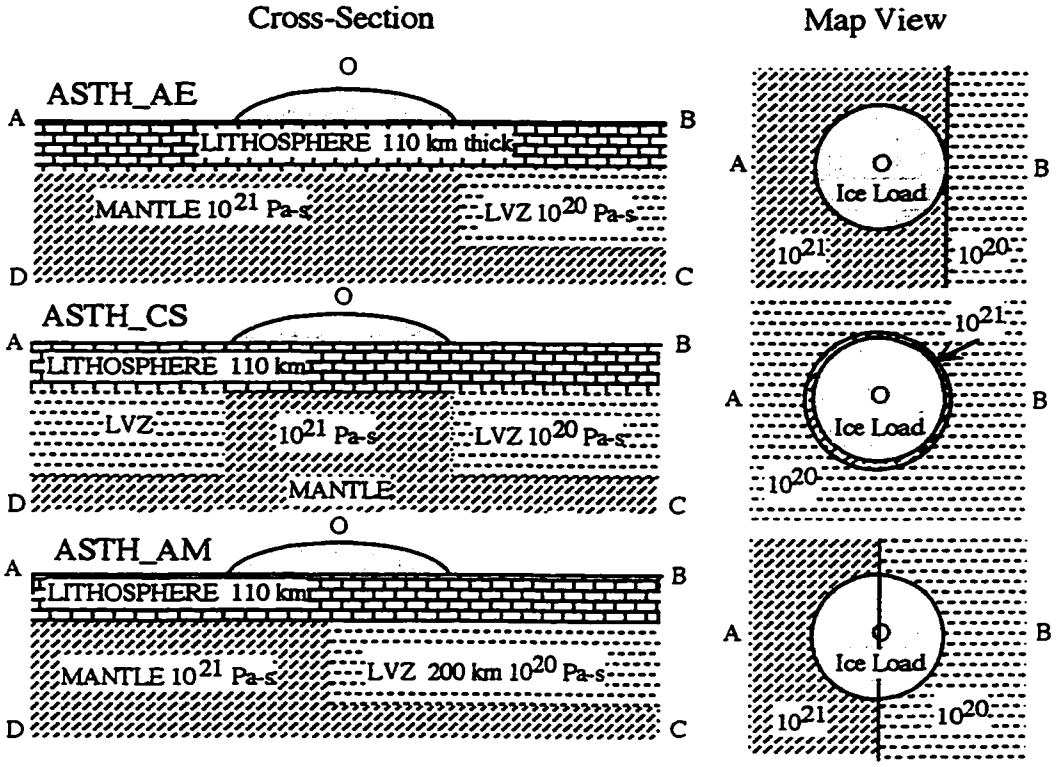

Figure 5.5 Three-dimensional and laterally heterogeneous models with a Low Viscosity Zone (LVZ): ASTH_AE, ASTH_CS, and ASTH_AM.

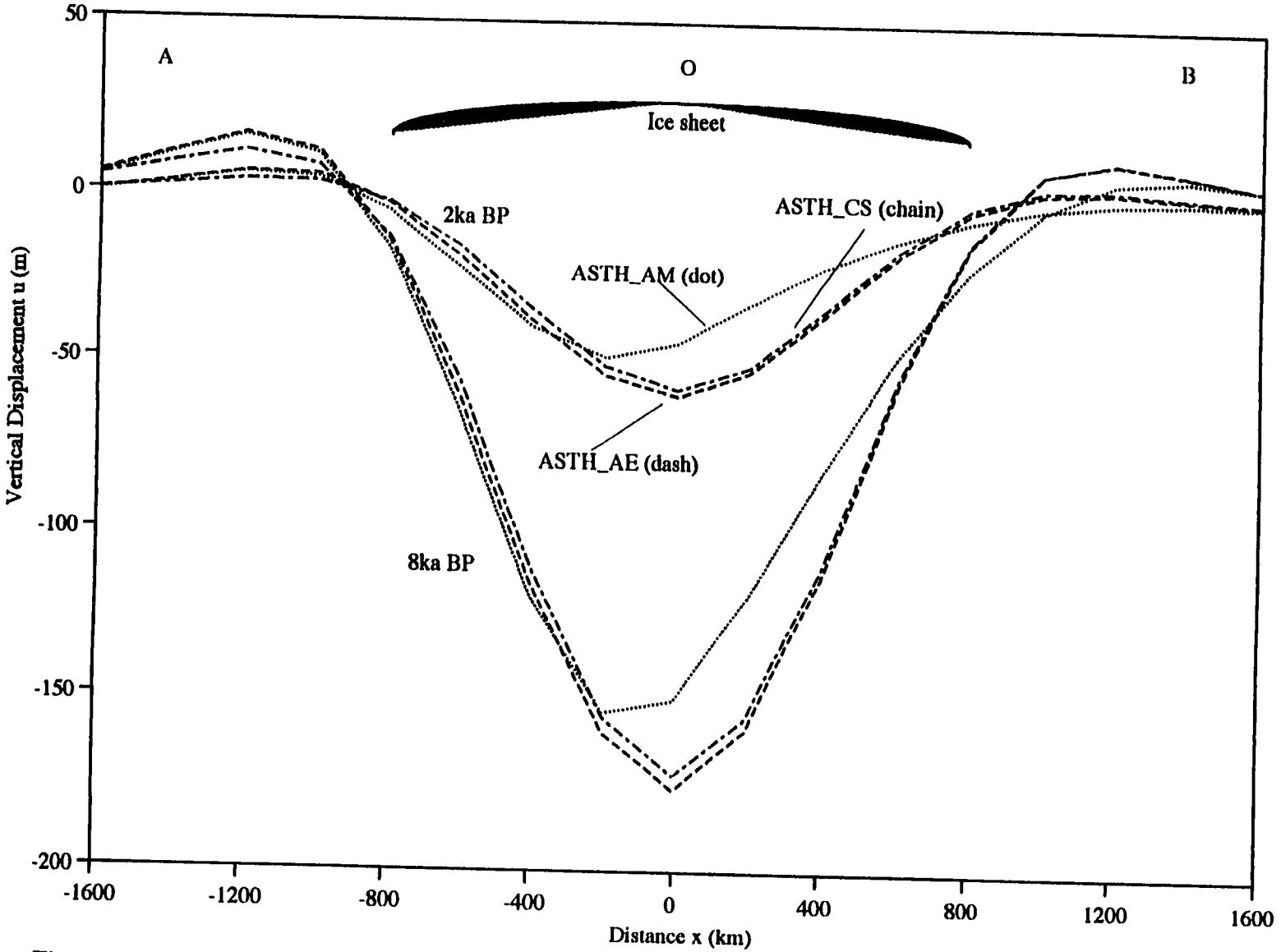

Figure 5.6 Displacement curves at 2 and 10 ka BP for models ASTH_AE, ASTH_CS, and ASTH_AM.

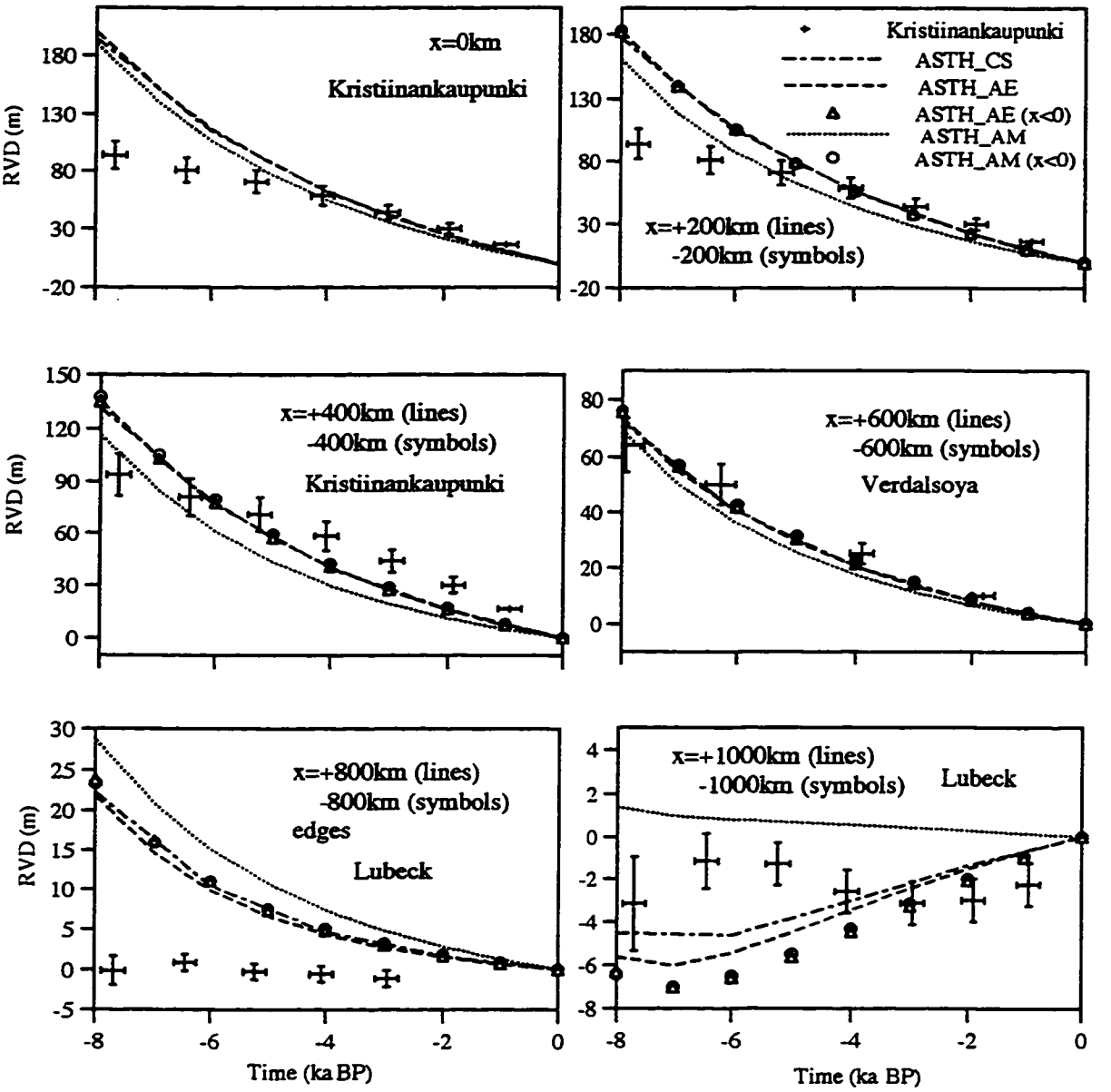

Figure 5.7 Similar to Fig. 3.4 except for models ASTH_AE, ASTH_CS, and ASTH_AM

5.2 EFFECTS OF NON-AXISYMMETRIC LATERAL HETEROGENEITIES

Here, we investigate the effects of non-axisymmetric lateral heterogeneities. This had been a serious test to some previous conclusions from the axisymmetric models. For example, it has been proposed that postglacial rebound at the edge has most resolving power for the lateral heterogeneity (Sabadini et al., 1986; Kaufmann et al., 1997). This may be true for models whose material properties change near or outside the load edge. But what if the properties change laterally under the middle of the disc load with half of the load on one kind of material while the other half on another? Will the edge still be sensitive to the change?

Model LITH_AM is designed to answer these questions. Its lithospheric thickness changes laterally across a vertical plane under the middle of the disc load: half of the load sit on 150 km thick lithosphere while the other half sit on 50 km thick lithosphere (Fig. 5.2). Other aspects of model LITH_AM are the same as that of model LITH_AE. In addition, two laterally homogeneous reference models LITH_150 and LITH_50 are considered. Each of them has a uniform 150 km or 50 km thick lithosphere overlying a Maxwell halfspace of 10^{21} Pa-s.

For $x>0$ where model LITH_AM's lithosphere is 50 km thick, the displacement profiles (Fig. 5.3) for LITH_AM (dot line) are almost the same as those for model LITH_50 (solid line), so are RVD curves (dot line vs. solid line in Fig 5.4). On the other hand, for $x<0$ where LITH_AM's lithosphere is 150 km thick, the displacements (Fig. 5.3) for LITH_AM (dot line) differ from model LITH_150 (thick line). However, the RVD curves (Fig. 5.4) for model LITH_AM (circle) are very close to those for model LITH_150 (thick line) at sites with $x<0$. Thus, as far as RVD are concerned, postglacial rebound of model LITH_AM reflects lithospheric thickness beneath the observation sites, except at $x = \pm 600 km$ where, like the inner peripheral area noticed earlier in chapter 3, RVD curves are not sensitive to differences among the models. Hence, effects of the lateral heterogeneity lies in variations of the rebound from site to site. In this case, spatial variation in RVD due to the lithospheric thickness change beneath the middle of the load is the largest around the central area.

Further, a revisit to results of model LITH_AE (Figs. 5.3 & 5.4) in comparison with the reference models confirms that the change beneath the ice edge mostly affects the area around the edge. The displacement profiles (Fig. 5.3) for LITH_AE (dash line) over most of the thick part of the lithosphere ($x \le 600km$) are almost on top of those for model LITH_150 (thick line); around the edge ($600km \le x \le 1200km$) where the lithospheric thickness changes from 150 km to 50 km at x=800 km, the displacement profiles are moving away from those for LITH_150 to those for LITH_50, and remain lying near those for model LITH_50 (thin line) for x > 1200 km. This is also evident in RVD curves in Fig. 5.4: RVD curves for LITH_AE (triangle and dash line) are almost on top of those for LITH_150 (thick line) at all sites with $x \le 600km$, and RVD curves for LITH_AE (dash line) are closer to those for LITH_50 (thin line) for x>800 km. The main spatial variation of RVD due to the lithospheric thickness change under the edge is around the edge area. Therefore, the area where RSL is most sensitive to lateral variation in lithospheric thickness is the area around where the variations take place. Furthermore, comparison of RVD histories between models LITH_AM and LITH_AE shows that the lateral variation beneath the middle of the load is more detectable by RSL data than that under the edge.

Similar conclusions can be drawn from models with lateral variations in asthenospheric viscosity. Model ASTH_AM is similar to ASTH_AE except that the LVZ extends to the middle of the disk load (Fig. 5.5). Results for model ASTH_AM are shown in Figs. 5.6 and 5.7. Similarly to LITH_AM, ASTH_AM exhibits asymmetric rebound in Fig. 5.6. The displacement profiles (dot lines) are almost on top of those for ASTH_AE (dash line) for x <-200 km. It relaxes faster than ASTH_AE for x>-200 km. This can also be seen in RVD histories in Fig. 5.7: ASTH_AM relaxes faster than model ASTH_AE at sites $x \ge 0$. This is because ASTH_AM has an asthenosphere underneath the area. The difference between the RVD curves of ASTH_AM at x = $\pm 200km$, or $\pm 400km$, or $\pm 800km$, or $\pm 1000km$ indicates the change at x = 0. Again, RVD at $\pm 600km$ are not sensitive to the model property. For ASTH_AE, the RVD only shows small separation between x=1000 km (dash line) and -1000 km (triangles). This is because the change is at x = 800 km.

We have also computed models ASTH_TC and ASTH_TE in which the low viscosity zones are restricted to lie in one quarter of the whole area (Fig. 5.8). In model ASTH_TC, the corner of the LVZ extends to beneath the center of the disk load while in model ASTH_TE the corner only touches the edge of the disk load. The differential RVD between models ASTH_TC and reference model ASTH_21 (same as R110/21 except in the

3D grid) for 8 ka BP and 4 ka BP are contoured in Fig. 5.9. It is obvious that only the quarter of area above the LVZ relax faster. When the LVZ moves out of the load area, differential RVD between ASTH_TE and ASTH_21 are very small and mostly located outside the load area (Fig. 5.10). All these confirm that spatial variation in RVD due to a lateral variation in viscosity is most prominent around where the variation is. And, the property change beneath the load is more detectable than that under the edge, by RSL data.

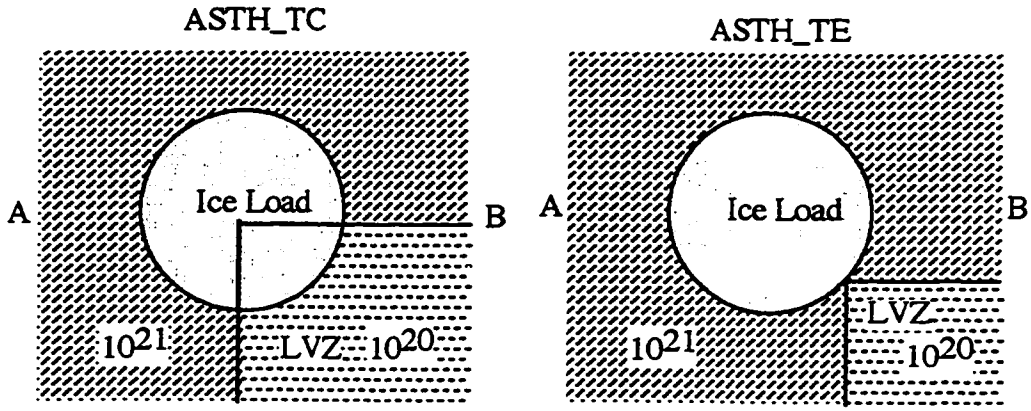

Figure 5.8 Map views of three-dimensional and laterally heterogeneous models with a Lower Viscosity Zone (LVZ): ASTH_TC and ASTH_TE.

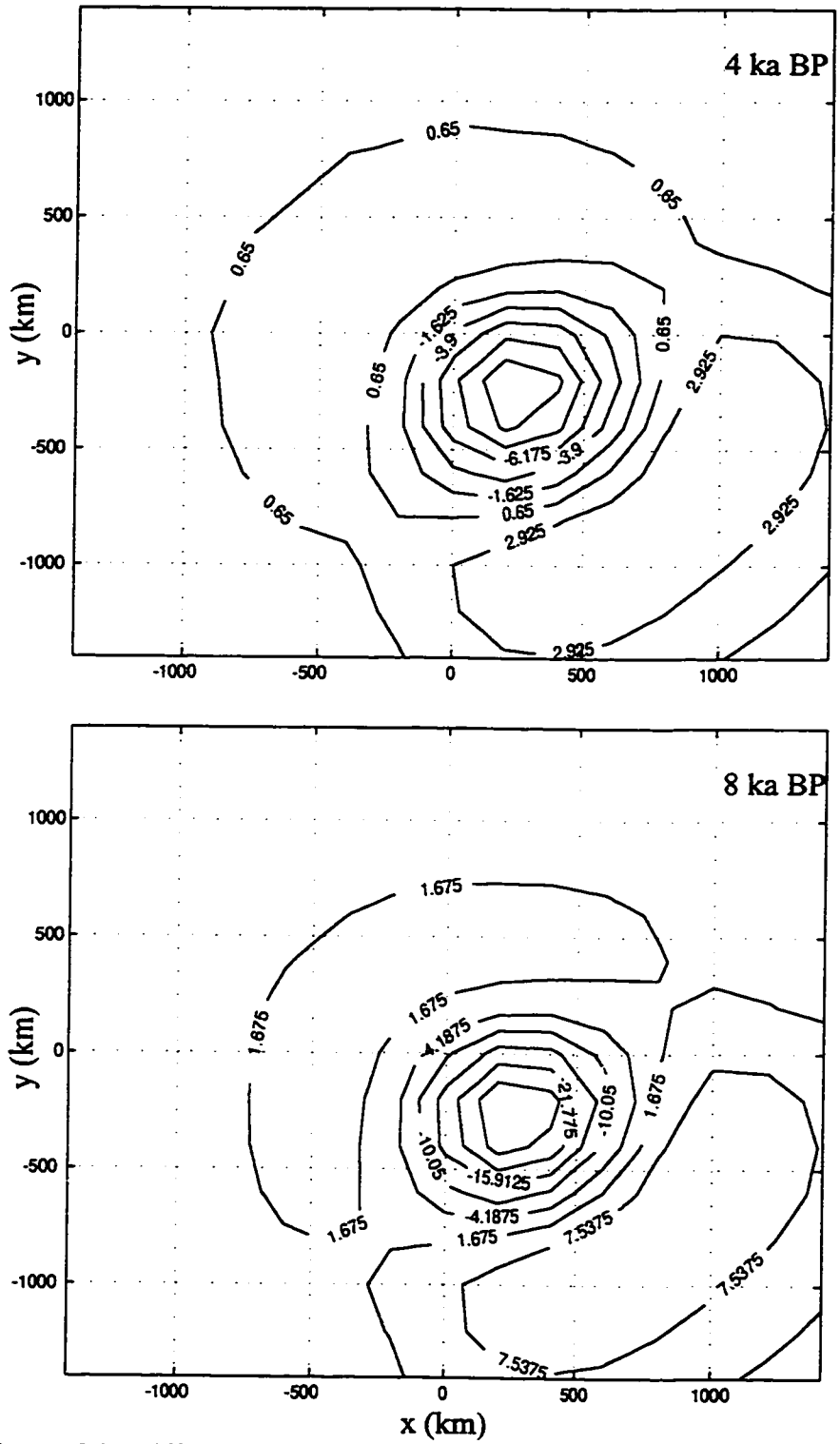

Figure 5.9 Differential RVD (m) between models ASTH_TC and ASTH_21 for times at 8 ka BP (lower panel) and 4 ka BP (upper panel).

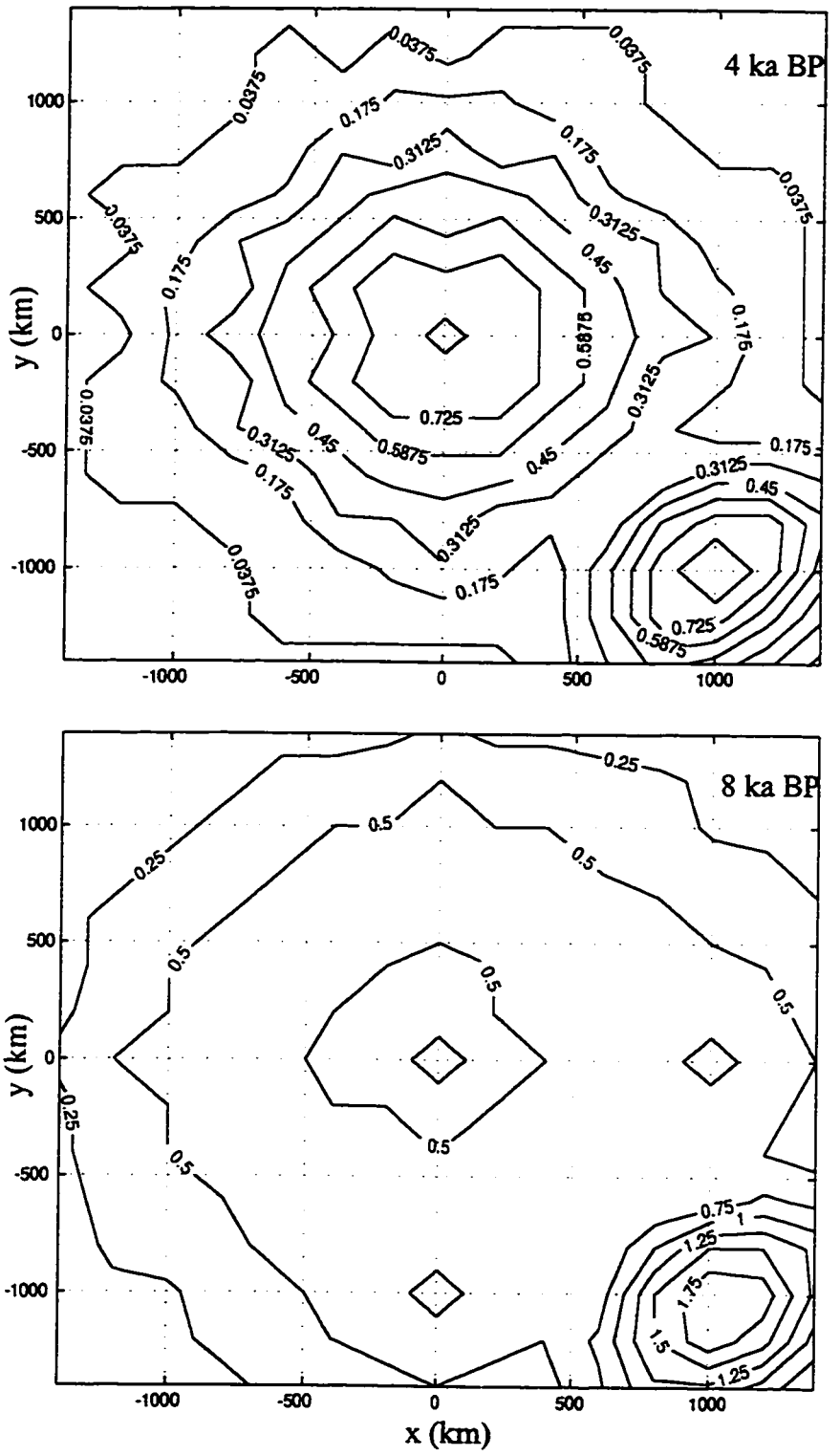

Figure 5.10 Differential RVD (m) between models ASTH_TE and ASTH_21 for times at 8 ka BP (lower panel) and 4 ka BP (upper panel).

5.3 EFFECTS OF MORE REALISTIC LATERAL HETEROGENEITIES - POSTGLACIAL REBOUND IN NORTH AMERICA

Modeling the effects of lateral heterogeneities on postglacial rebound has gone through axisymmetric models (Sabadini et. al, 1986; Gasperini & Sabadini 1989, 1990; Gasperini et al., 1990; 1991; Kaufmann et al., 1997; Chapters 3 & 4) to 3D non-axisymmetric models (Sections 5.1 & 5.2), with simple earth models and hypothetical disk loads. Now, we wish to do a more realistic simulation using a relatively realistic three dimensional laterally heterogeneous earth model and a realistic ice history. The purpose is to test the sensitivity of postglacial rebound to more realistic heterogeneities under a realistic ice load. This will also put previous learning on a test and give some hints to question 3, i.e. how applicable are these simple earth results in a more realistic case?

Postglacial rebound data from sites in eastern Canada and along the Atlantic coast of North America have been extensively used to estimate the rheological structure of the Earth's mantle (e.g. Cathles 1975; Wu & Peltier, 1983; Sabadini et al., 1985; Yuen et al., 1986; Han & Wahr, 1995) and to recover the ice history (Peltier & Andrews, 1976; Wu & Peltier, 1983; Tushingham & Peltier, 1991; Peltier, 1994) since early work on estimating ice volume (e.g. Paterson, 1972) and collecting RSL data (e.g. Walcott, 1972). Here, the postglacial rebound in North America is modeled using a realistic deglaciation history for the Laurentian, Cordillera, Innuition and Greenland Ice Sheets defined in the ice model Ice-3G (Tushingham & Peltier, 1991) for two earth models, a laterally homogeneous reference model LITH_200 and a laterally heterogeneous model LAT_HET.

Model LITH_200 is composed of a 200 km thick lithosphere overlying a Maxwell halfspace of 10^{21} Pa-s. The heterogeneous model LAT_HET mimics the shape of the North American continent, lateral variations of lithospherical thickness, and asthenospheric thickness and viscosity from the continental to oceanic regions (Fig. 5.11). It differs from the reference model within the top 200 km of the model in oceanic areas and areas surrounding the Canadian shield. Under the Canadian shield, rheological structure is the same as the reference model (with a 200 km thick lithosphere overlying a 10^{21} Pa-s visco-elastic mantle). Under the oceans, the 55 km thick oceanic lithosphere overlies a 150 km thick

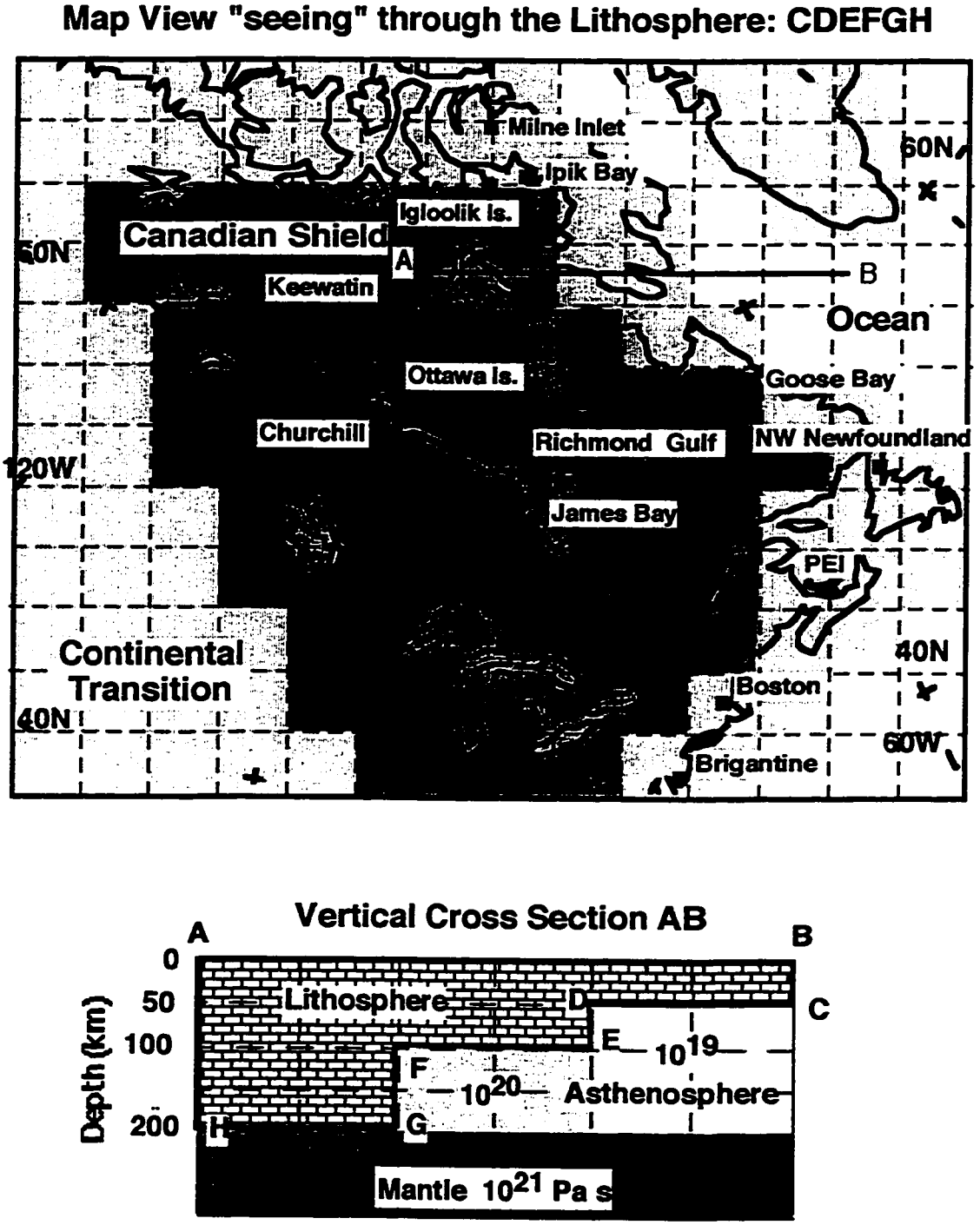

Figure 5.11 Laterally heterogeneous 3D earth model for North America.

10^{19} Pa-s asthenosphere. In the transitional zone between the craton and the ocean, the lithosphere is 100 km thick and overlies a 100 km thick 10^{20} Pa-s asthenosphere. The spatial distribution of these three zones and a schematic cross-section are shown in Fig. 5.11. This laterally heterogeneous model is based on educated guesses, and should be refined in future investigations. All other material property parameters are the same as those in the previous 3D models (e.g. ASTH_AM) except for the Poisson ratio of 0.2854 reflecting compressibility of earth material.

5.3.1 Comparison of RVD with observed RSL

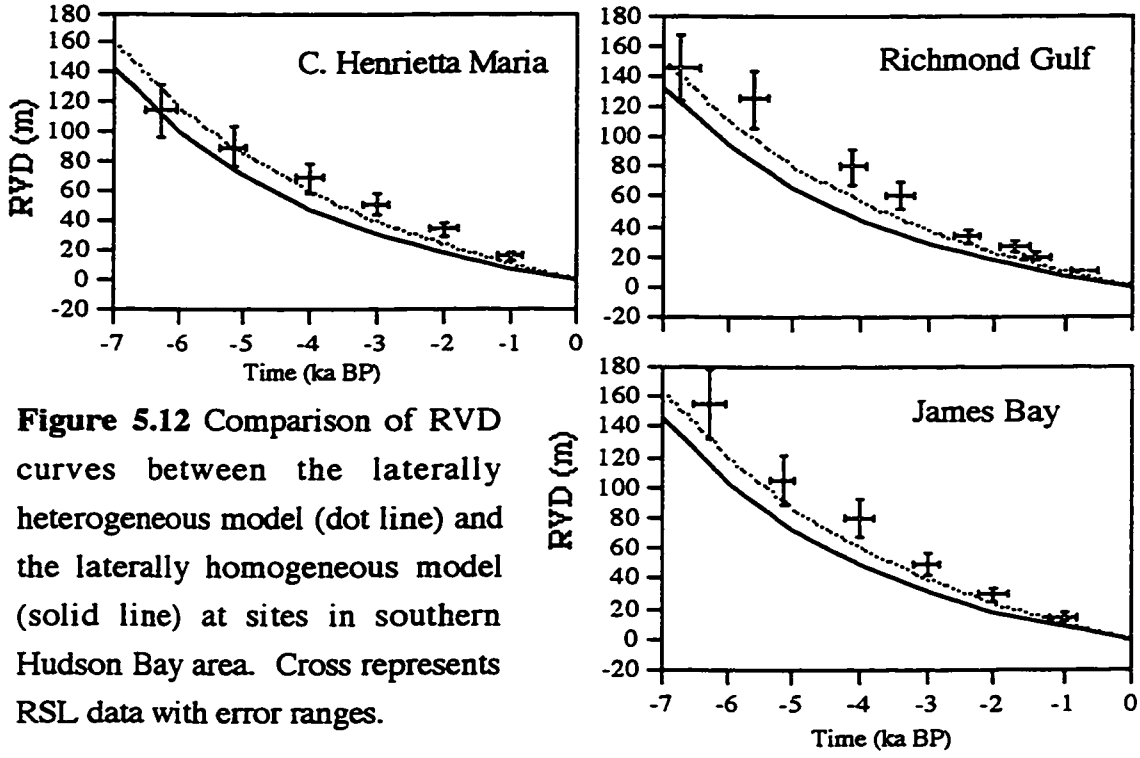

Figure 5.12 Comparison of RVD curves between the laterally heterogeneous model (dot line) and the laterally homogeneous model (solid line) at sites in southern Hudson Bay area. Cross represents RSL data with error ranges.

Our main focus is to compare RVD predictions of models LAT_HET and LITH_200 in order to study the effects of lateral heterogeneities. As always, the observed RSL with error bars are plotted to indicate resolvability of the difference by RSL data. Nevertheless, comparisons of the RVD with the RSL are also documented and discussed for the sake of further improvements of the earth model as well as the ice model. Because RVD is only a valid approximation to RSL during postglacial time, the comparison is limited to the last 7 ka. The plots are gathered according to their geographic locations (see Appendix B for coordinates of the sites, some are also shown in Fig. 2.5) in Figs. 5.12 - 5.18. Sites in

southern Hudson Bay area including Cape Henrietta Maria, Richmond Gulf, James Bay, Que. are gathered in Fig. 5.12. Churchill, Man. and Keewatin, NWT of western Hudson Bay area are in Fig. 5.13. Milne Inlet, Baf., Igloolik Is., and Ipik Bay, Baf. of northern Hudson Bay area are in Fig. 5.14. Ungava Pen., Southampton Is. and Ottawa Is., NWT of the central Hudson Bay area and Cape Tanfield of north-eastern Hudson Bay area are in Fig. 5.15. Goose Bay and NW Newfoundland are in Fig. 5.16. Tignish, PEI, French River, PEI, Cape Breton Is., NS., and Bay of Fundy are in Fig. 5.17. Isles of Shoals, NH, Boston, MA, Clinton, CT, and New York are in Fig. 5.18.

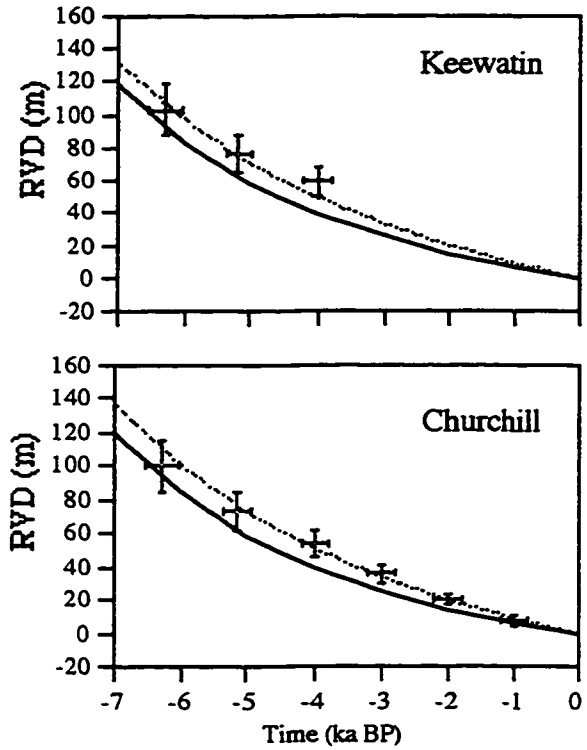

Figure 5.13 Similar to Fig. 5.12 except at sites in western Hudson Bay area.

In general, the comparison of the predicted RVD curves between models LITH_200 (solid line) and LAT_HET (dot line) confirms conclusions drawn from previous simple earth models: effects of lateral heterogeneities are additional spatial variations in postglacial rebound, and land uplift of a laterally heterogeneous model at a site reflects the earth properties underneath. Especially, the spatial trend of land uplift reflects the spatial trend of lateral heterogeneities. For example:

(a) Differences of RVD curves between the two models are small when compared to the uncertainties of the RSL observations, for sites where the two models have same earth properties which happen to be near the center of the rebound (sites in Figs. 5.12, 5.13, and Southampton Is. and Ottawa Is. in Fig. 5.15).

(b) Significant differences are found in areas where the two models have different earth properties which happen to be near and outside the ice margin (sites in Figs. 5.16 and 5.18). These differences are mostly resolvable by RSL data within last 5 or 4 ka BP

because the uncertainties of the height in RSL data are smaller for younger data points than the older ones.

The comparison between the RVD and the RSL date (dot with error bar) divides all sites into four groups: at Group A sites, the predictions of model LAT_HET fit the observed data better or are closer to the data than those of model LITH_200; at Group B sites, model LITH_200 does better than LAT_HET; at the rest of the sites, the predictions of the two models are either too much off the observed data (Group C) or equally close to the data (Group D i.e. Ipik Bay, Baf.).

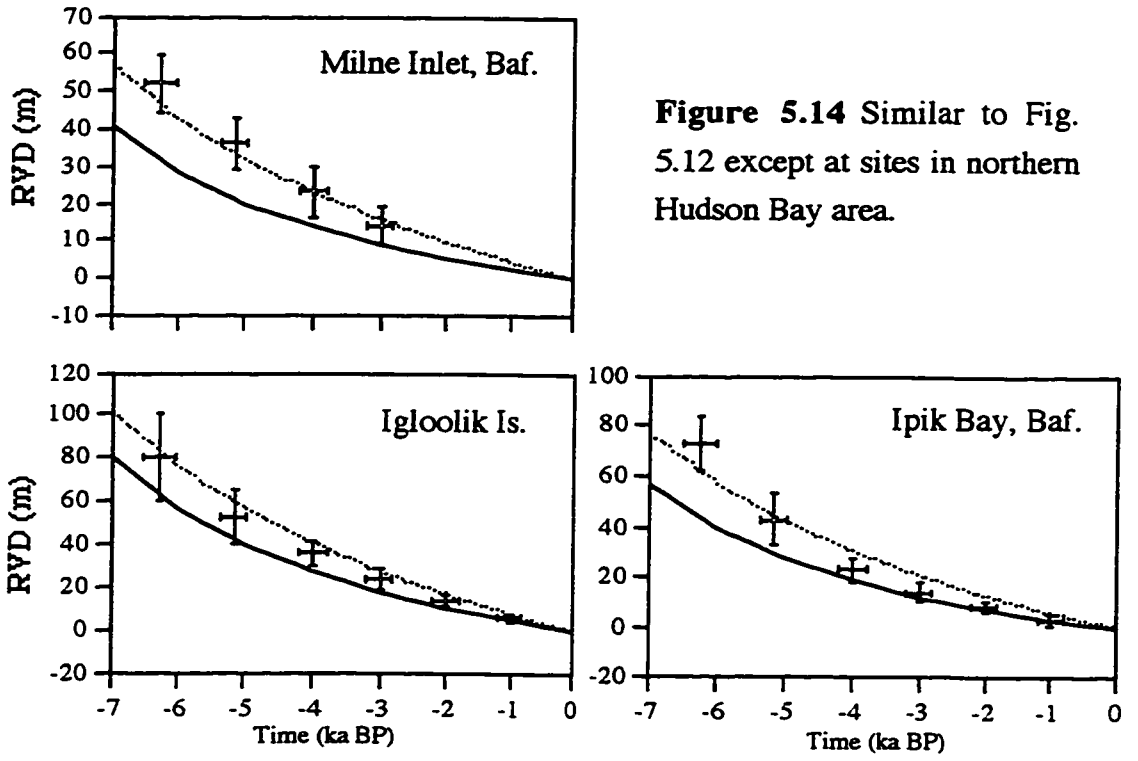

Figure 5.14 Similar to Fig. 5.12 except at sites in northern Hudson Bay area.

Group A sites include Cape Henrietta Maria, Richmond Gulf, and James Bay, Que. in southern Hudson Bay area; Churchill, Man. and Keewatin, NWT in western Hudson Bay area; Milne Inlet, Baf. and Igloolik Is. in northern Hudson Bay area; Clinton, CT. in the periphery area of the Laurentian ice.

Group B sites include Cape Tanfield, Ungava Pen., Southampton Is., and Ottawa Is., NWT in north-eastern and central Hudson Bay area; Goose Bay, NW Newfoundland, Isles of Shoals, NH, Boston, MA, and New York in the periphery area.

Group C sites include Tignish, PEI, French River, PEI, Cape Breton Is., NS., and Bay of Fundy.

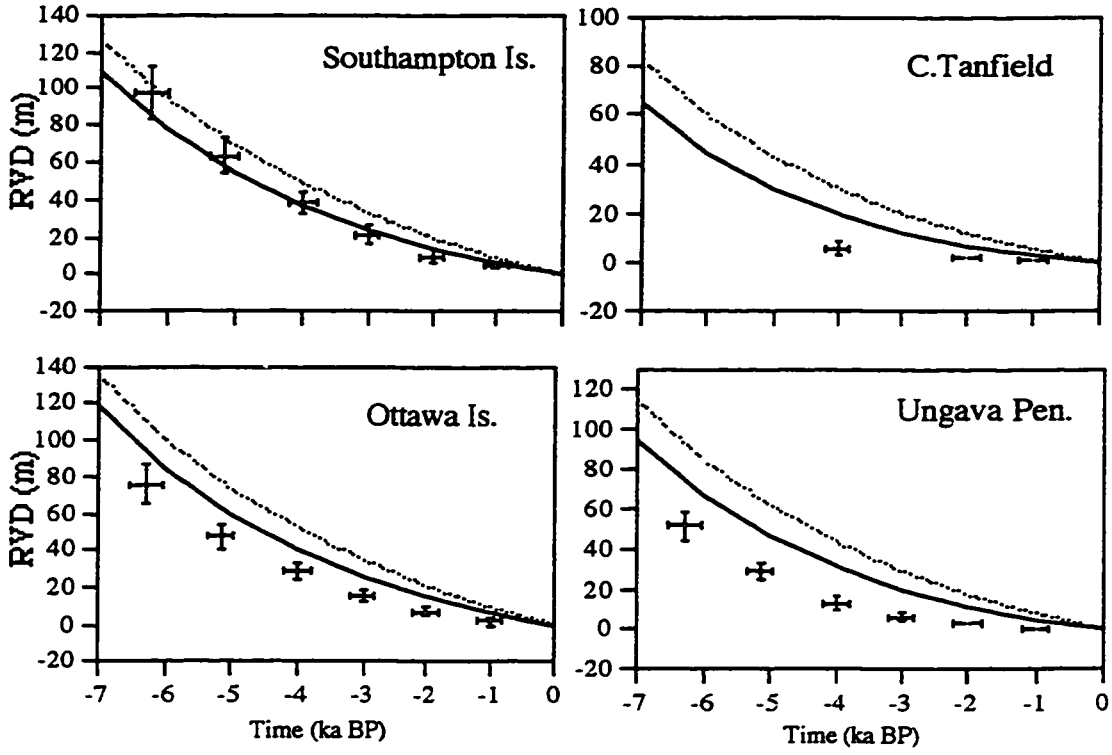

Figure 5.15 Similar to Fig. 5.12 except at sites in central and north-east Hudson Bay area.

5.3.2 Discussion

The misfits between the predicted RVD and observed RSL at Group C sites are no surprise as these sites are "considered ice-marginal or edge sites" (Tushingham & Peltier 1991). The ice history at these edge sites may not be precise enough because the ice history is mainly constrained by RSL data inside the former glaciated areas. Further, the finite element grid is not fine enough to honor Ice-3G in this area. Hence, the misfits may be caused by inaccurate ice model in this area used in the finite element comptuations.

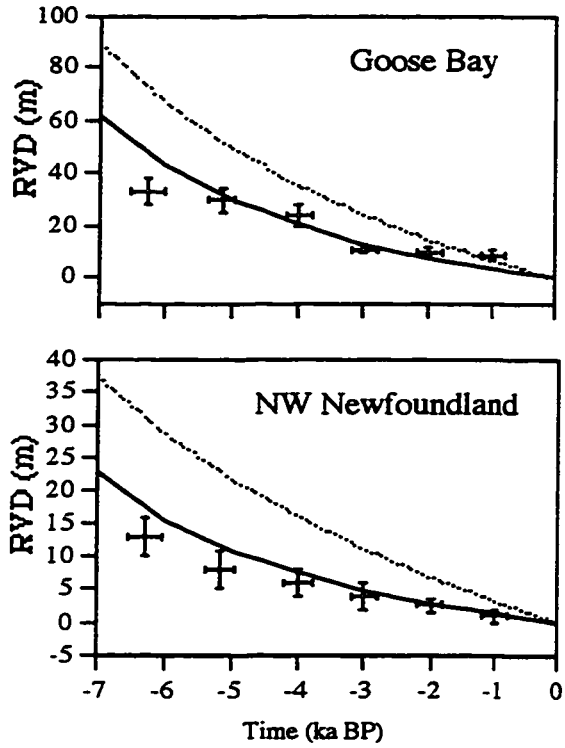

Figure 5.16 Similar to Fig. 5.12 except at sites in Canadian east coast.

The patter that model LAT_HET's predictions are closer to the data than LITH_200's at sites around the Hudson Bay area but are worse at sites in central Hudson Bay area and Hudson Bay strait in the north-east appears to be correlated with the ice history (see the time snap shot of Ice-3G at 8 ka BP in Fig. 9, Tushingham & Peltier, 1991). The ice melted earlier in the central and north-east area than in the area around Hudson Bay. This correlation implies that the ice in the central and north-east area of the Bay could melt even earlier than that prescribed in Ice-3G if model LAT_HET is held to be true.

At sites Cape Tanfield, Ungava Pen., and Ottawa Is., NWT, although model LITH_200's predictions are closer to the data than that predicted by model LAT_HET, data points are still below the predicted curves. This can suggest a thicker lithosphere or/and a lower asthenospheric viscosity. However, RSL data at Cape Tanfield is almost flat, so it is more like a standing point than anything else. A standing point is usually located near the ice margin. It stands almost still and separates the up-going central area from the down-going forebulge area during late postglacial time.

For sites at Goose Bay and NW Newfoundland, the trends of the data are flatter than predictions. If we had thick (200 km) lithosphere over low viscosity asthenosphere in this part of model LAT_HET, model LAT_HET may fit the data better than model LITH_200. However, at Goose Bay, there is a step change in data from 3 to 4 ka BP that may be due to other causes than the earth properties.

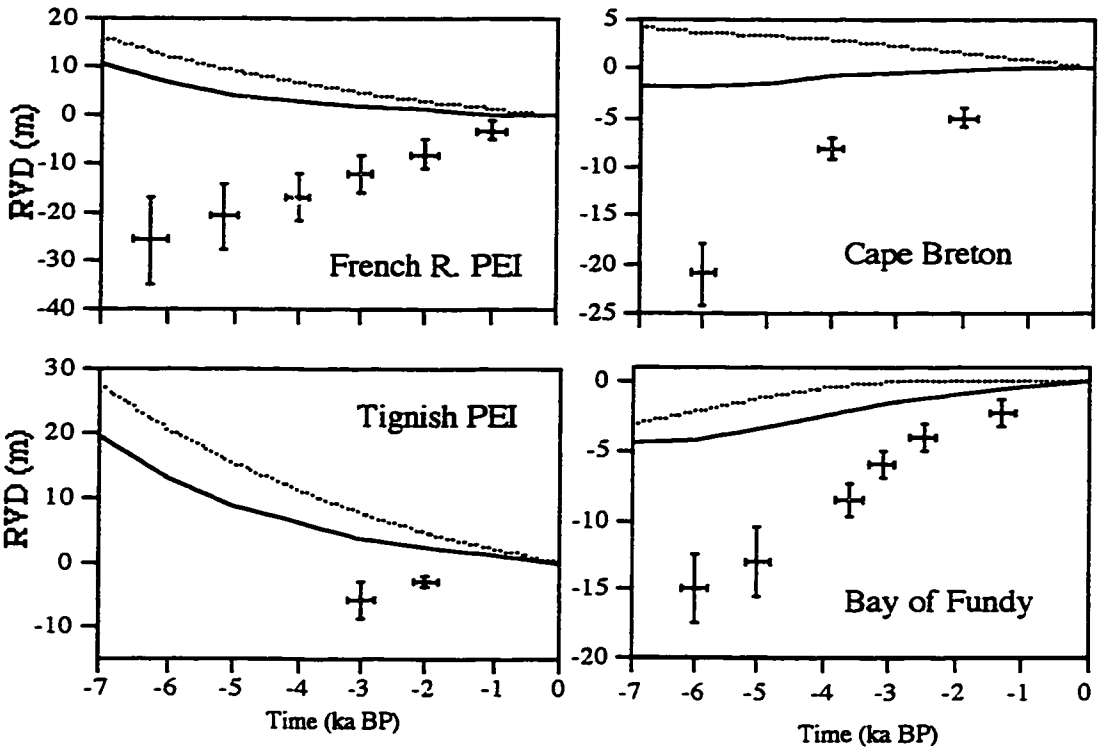

Figure 5.17 Similar to Fig. 5.12 except at different sites as labeled in each panel.

At most sites along North American Atlantic coast, model LITH_200's predictions are closer to RSL data, except at Clinton (Connecticut). The data at Boston and New York suggest larger curvatures than the predicted. This may be indicative of large viscosity and/or thin lithosphere. However, the trend of the data at nearby site Clinton (Connecticut) is quite flat which may suggest low viscosity and/or thick lithosphere. Furthermore, all these sites could be in an area similar to the inner peripheral area discussed in chapter 3 where RSL is least sensitive to an earth model's properties. In this case, the comparison at these sites may not be indicative of earth properties. The RSL data here may also be affected by tectonic movements that are caused by the sediment loading of the glacial outwash (e.g. Newman et al 1980).

In short, the comparison between the two models confirms that postglacial rebound is sensitive to relatively realistic heterogeneities with a realistic ice history. Further, the response of postglacial rebound to the realistic heterogeneities is similar to the simple heterogeneities in previous simple models. Therefore, the conclusions from previous simple models are valid for this more complex model.

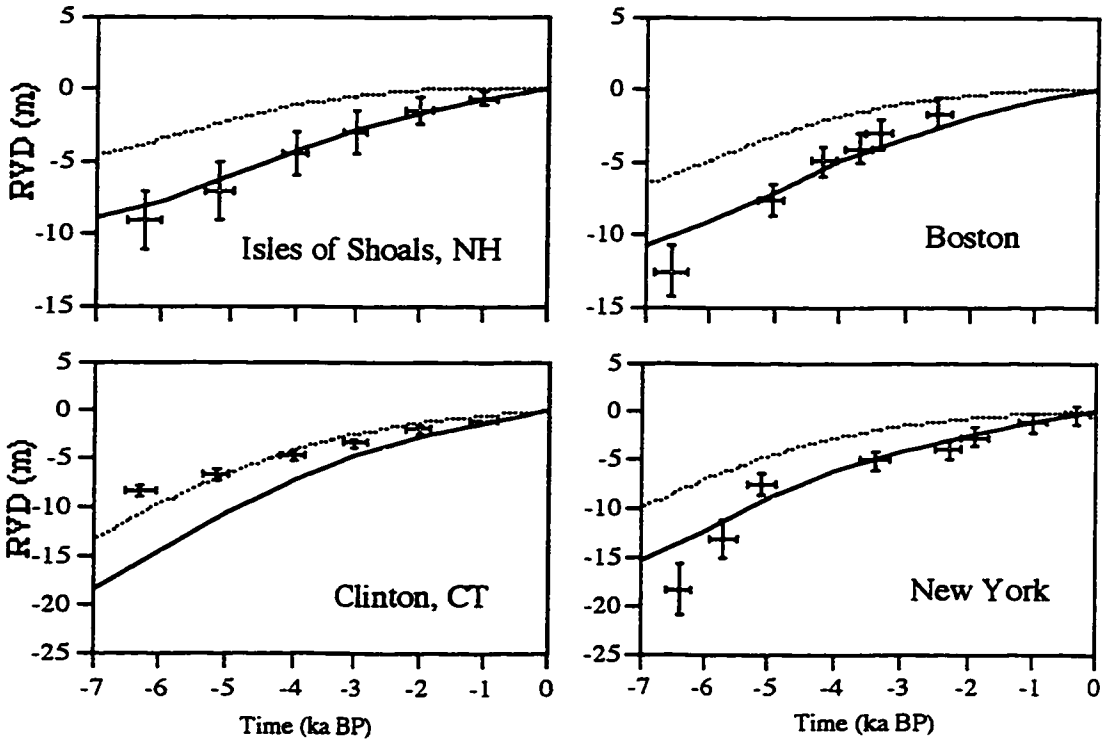

Figure 5.18 Similar to Fig. 5.12 except at sites in the U.S. east coast.

5.4 SUMMARY

We have extended postglacial rebound modeling from 2D to 3D, and from simple earth models to a more realistic model. In doing so, we have answered the three questions listed at the beginning of the chapter:

1) The axisymmetry in the models does not noticeably amplify effects of lateral variation based on 3D model results in this chapter.

2) Non-axisymmetric models have shown that sensitivity of RVD to a lateral heterogeneity depends on the relative location of the observation site with respect to the lateral heterogeneity. When a change in model property takes place under the middle of the load, RVD in the central area is sensitive. Vice versa, RVD around the edge is sensitive to a property change under the edge. Further, no matter how sensitive RSL at a site is, RSL at the single site can not tell the existence of the lateral heterogeneity because the data can also

be sensitive to vertical rheological structure. Therefore, the lateral heterogeneity can only be detected by comparing RSL at sites across a large area, i.e. spatial-temporal pattern of postglacial rebound. Furthermore, the effects are most prominent for the variation (of lithospheric thickness or asthenospheric viscosity) inside the former glaciated area.

3) The realistic modeling of postglacial rebound in North America confirms that simple earth models results are consistent with the response of this more complex earth model to the realistic ice load history.

Although the flat-Earth models have served us well for computing deformation in and near a formerly glaciated area, a self-gravitating spherical earth model is needed for accurate prediction of worldwide relative sea level changes that include effects of glaciation and deglaciation of distant ice sheets and the distribution of melted ice water in oceans. In the next chapter, we will turn our focus to analytical solutions of simple spherical earth models and use the result to calibrate the spherical finite element model in chapter seven.

CHAPTER 6

LAYERED SPHERICAL EARTH MODEL

Although the initial motive for studying laterally homogeneous spherical earth models using the spectral method in this thesis is to calibrate the spherical finite element model, the study has been expanded to include some important issues in modeling postglacial rebound of spherically stratified earth models.

The spectral method is usually implemented numerically (Peltier, 1974; Wu & Peltier, 1982; Mitrovica & Peltier, 1989) for a multi-layer spherical earth model and solutions are usually expressed as the superposition of normal modes of gravitational relaxation (Longman, 1963; Peltier, 1976; Peltier & Andrews, 1976; Wu & Peltier, 1983; Mitrovica & Peltier, 1989; also eq. 6.1.18). The questions of interest are: (1) how many modes can a spherically layered earth model have for each angular order of spherical harmonic deformation? (2) how are the modes related to contrasts in physical properties among the layers? (3) how can singularities in the numerical search for the eigenmodes be removed? and (4) what are the effects of neglecting self-gravitation?

Wu & Peltier (1982) demonstrated numerically that a pure density discontinuity introduces an extra (buoyancy) mode and a finite viscosity jump introduces two extra (viscoelastic) modes (also see Han & Wahr, 1995). The uncertainty here is that these may only represent the minimum number of modes. It has not been theoretically established (except for the inviscid core and the simple lithosphere cases discussed in Amelung & Wolf, 1994) how many modes a certain earth model should have and how they are related to contrasts in material properties. Furthermore, there is the problem of singularities in the characteristic function (i.e. the determinant function, DET(s) whose roots give the eigen-spectrum). These singular points can be easily confused with roots because they appear as zero-crossings of DET(s) (Han & Wahr, 1995; Fang & Hager, 1995). When the number of layers is large, the number of singularities and the number of 'viscoelastic modes' is large and they can be so densely populated that some eigenmodes may be

missed by the numerical root-searching scheme. So it is useful to devise a singularity free approach.

These issues can be best understood in analytical solutions of simple spherically layered earth models in spectral domain. In fact, solving the analytical solution for such earth deformation problem is always appealing. Dragoni et al. (1983) extended the analytical solutions of Wu & Peltier (1982) to the deformation of a two-layer incompressible Maxwell sphere without a core in an attempt to examine whether earthquake-triggered movements of earth material can excite the Chandler wobble. In the study of lithospheric effects on postglacial rebound, Wolf (1984) derived analytical solutions for an incompressible and hydrostatic prestressed Maxwell sphere surrounded by a thick elastic shell under a Heaviside disc load for the non-self-gravitating case. Wu (1990) used the analytical solutions for two-layer earth models to study the deformation of internal boundaries. Spada et al. (1990) solved five-layer earth models with Mathematica, but no solution in closed form was found. This is because the analytical expression is too long to be handled by the symbolic manipulation program thus the advantages of the analytical approach has not been fully utilized. To limit the length of the expression, we explored the solution of a 2-layer non-self-gravitating earth.

In the following sections, we first illustrate the general formalism of solutions to the deformation of a 2-layer spherical earth model under a surface load (section 6.1), then evaluate the effects of neglecting self-gravitation (section 6.2), and finally explore the relationship between eigenmodes and discontinuities in density, viscosity, and shear modulus between the two layers. For simplicity, only incompressible earth models are considered in most cases.

6.1 GENERAL FORMALISM

In this section, unified solutions are presented for both self-gravitation and non-self-gravitation cases. The flag δ_g indicates that the terms are due to self-gravitation and serves as a switch between the two cases, $\delta_g=1$ for self-gravitation case and $\delta_g=0$ for non-self-gravitation case. The switch makes it easy for modifying existing computer programs for computing the self-gravitating case to the non-self-gravitating case. The idea of flagging is

then extended to keep track of the prestress advection term with δ_a, so the effects of the prestress advection can be easily examined.

Take a spherical coordinate system with the origin at the earth center and the z-axis pointing to the North pole. The three coordinates for a point are radius (r), colatitude (θ), and longitude (φ). Let u, v, w represent displacement components on the three base vectors $\mathbf{e}_r$, $\mathbf{e}_\theta$, and $\mathbf{e}_\varphi$, respectively. For a non-rotating spherical earth model, the linearized equation of momentum conservation, Poisson's equation, and the equation for the conservation of mass in the Laplace transformed domain s can be written as (Wu & Peltier, 1982):

$$0 = -\rho_0 \delta_g \nabla\phi_1 - \rho_1 g_0 \mathbf{e}_r - \nabla(\mathbf{u}\cdot\delta_a \rho_0 g_0 \mathbf{e}_r) + \nabla\cdot\boldsymbol{\tau}$$

$$\nabla^2 \phi_1 = 4\pi G \rho_1 \delta_g \qquad (6.1.1)$$

$$\rho_1 = -\rho_0 \nabla\cdot\mathbf{u} - \mathbf{u}\cdot(\partial_r \rho_0)\,\mathbf{e}_r$$

where $\mathbf{u}$, $\boldsymbol{\tau}$, ϕ_1, g_0, ρ_0 and ρ_1 are the displacement vector, the perturbation stress tensor, the perturbed gravitational potential, the unperturbed gravity, and the initial and perturbed density respectively. For simplicity, consider an unit point load at the north pole, so that the deformation is pure spheroidal, and there is no displacement on $\mathbf{e}_\varphi$ (i.e. w=0). Using Legendre polynomial expansion of displacements and perturbation potential

$$u = \sum_{n=0}^{\infty} U_n(r) P_n(\cos(\theta))$$

$$v = \sum_{n=0}^{\infty} V_n(r) \frac{\partial P_n(\cos(\theta))}{\partial\theta} \qquad (6.1.2)$$

$$\phi_1 = \sum_{n=0}^{\infty} \Phi_n(r) P_n(\cos(\theta))$$

the group of second order partial differential equations (eq. 6.1.1) can be written as a set of simultaneous ordinary differential equations for a given layer (Cathles, 1975; Peltier, 1974):

$$\frac{d\mathbf{Y}}{dr} = \mathbf{A}\,\mathbf{Y} \qquad (6.1.3)$$

where the elements of the vector $\mathbf{Y}(r,s) = (U_n, V_n, T_{rn}, T_{\theta n}, \Phi_n, Q_n)^T$ are the spherical harmonic coefficients of radial and tangential displacements, radial and tangential stresses, perturbation in gravitational potential and potential gradient respectively. The potential gradient is defined as

$$Q_n = \frac{d\Phi_n}{dr} + \frac{n+1}{r}\Phi_n + 4\pi G\rho_o U_n \tag{6.1.4}$$

Here the subscript n denotes the angular order. The matrix A for a compressible solid is:

$$a_{1i} = \left\{-2\frac{\lambda}{(\lambda+2\mu)r},\ \frac{n(n+1)\lambda}{(\lambda+2\mu)r},\ \frac{1}{\lambda+2\mu},\ 0,\ 0,\ 0\right\}$$

$$a_{2i} = \left\{-\frac{1}{r},\ \frac{1}{r},\ 0,\ \frac{1}{\mu},\ 0,\ 0\right\} \tag{6.1.5}$$

$$a_{3i} = \left\{4\frac{(2\mu+3\lambda)\mu}{(2\mu+\lambda)r^2} - 4\frac{[(\delta_a+1)\mu+\delta_a\lambda]\rho g}{(2\mu+\lambda)r} - \frac{3(-\delta_a+\delta_g)\rho g}{r},\right.$$

$$n(n+1)\left[-2\frac{(2\mu+3\lambda)\mu}{(2\mu+\lambda)r^2} + \frac{(2\mu+\delta_a\lambda)\rho g}{(2\mu+\lambda)r}\right],\quad -\frac{(-\delta_a+1)\rho g r + 4\mu}{(2\mu+\lambda)r},$$

$$\left.\frac{n(n+1)}{r},\quad -\frac{(n+1)\rho_0\delta_g}{r},\quad \rho\delta_g\right\}$$

$$a_{4i} = \left\{-2\frac{(2\mu+3\lambda)\mu}{(2\mu+\lambda)r^2} + \frac{\rho g\delta_a}{r},\ -2\mu\left(\frac{1}{r^2} - 2\frac{(\mu+\lambda)n(n+1)}{(2\mu+\lambda)r^2}\right),\ -\frac{\lambda}{(2\mu+\lambda)r},\right.$$

$$\left.-3\frac{1}{r},\ \frac{\rho\delta_g}{r},\ 0\right\}$$

$$a_{5i} = \left\{-4\pi G\rho\delta_g,\ 0,\ 0,\ 0,\ -\frac{(n+1)\delta_g}{r},\ \delta_g\right\}$$

$$a_{6i} = \left\{\frac{-4\pi G\rho(n+1)\delta_g}{r},\ \frac{4\pi G\rho n(n+1)\delta_g}{r},\ 0,\ 0,\ 0,\ \frac{(n-1)\delta_g}{r}\right\}$$

where λ and μ are the s dependent Lame parameters, ρ is the ambient density field, g is the unperturbed gravitational acceleration and G is the gravitational constant. For an

incompressible earth, take the limit $\lambda \to \infty$ in matrix **A**. For a non-self-gravitating earth (δ_g =0), the last two rows and columns are identically zero, so **A** reduces to a 4x4 matrix.

For an incompressible uniform spherical solid shell, the generalized six linearly independent solution vectors at radius r are given by (Wu, 1978; 1990; Sabadini et al., 1982):

$$y_1 = \Big(\frac{n\, r^{n+1}}{2(2n+3)}, \frac{(n+3)\, r^{n+1}}{2(2n+3)(n+1)}, \frac{n\rho g r^{n+1}\delta_a + 2\mu(n^2-n-3)\, r^n}{2(2n+3)},$$

$$\frac{2\mu n(n+2) r^n}{2(2n+3)(n+1)}, 0, \frac{4\pi G\rho n r^{n+1}}{2(2n+3)}\delta_g \Big)^T$$

$$y_2 = \Big(r^{n-1}, \frac{r^{n-1}}{n}, \rho g r^{n-1}\delta_a + 2\mu(n-1)\, r^{n-2}, \frac{2\mu(n-1) r^{n-2}}{n}$$

$$0, 4\pi G\rho r^{n-1}\delta_g \Big)^T$$

$$y_3 = \Big(0,\ 0, \rho r^n \delta_g, 0, r^n \delta_g, (2n+1)\, r^{n-1}\delta_g \Big)^T \qquad (6.1.6)$$

$$y_4 = \Big(\frac{(n+1)\, r^{-n}}{2(2n-1)}, \frac{-(n-2)\, r^{-n}}{2n(2n-1)}, \frac{(n+1)\rho g r^{-n}\delta_a - 2\mu(n^2+3n-1) r^{-(n+1)}}{2(2n-1)}$$

$$\frac{2\mu(n+1)(n-1) r^{-(n+1)}}{2n(2n-1)}, 0, \frac{4\pi G\rho(n+1) r^{-n}}{2(2n-1)}\delta_g \Big)^T$$

$$y_5 = \Big(r^{-(n+2)}, \frac{-r^{-(n+2)}}{n+1}, \rho g r^{-(n+2)}\delta_a - 2\mu(n+2) r^{-(n+3)}, \frac{2\mu(n+2)}{n+1} r^{-(n+3)},$$

$$0, 4\pi G\rho r^{-(n+2)}\delta_g \Big)^T$$

$$y_6 = \Big(0,\ 0, \rho r^{-(n+1)}\delta_g, 0, r^{-(n+1)}\delta_g, 0 \Big)^T$$

The last three solution vectors are singular at the earth's center and must be excluded for a uniform sphere (see Wu & Peltier, 1982). Thus, the solution in the inner uniform solid sphere is a linear combination of the first three vectors, or

$$\mathbf{Y}_C(r) = \mathbf{Z}(r)\mathbf{K} \tag{6.1.7}$$

where $\mathbf{Z}(r)$ is the matrix whose column vectors are $\mathbf{y}_1$, $\mathbf{y}_2$,$\mathbf{y}_3$ and

$$\mathbf{K} = (K_1(s), K_2(s), K_3(s))^T \tag{6.1.8}$$

is the coefficient vector. Similarly, the solution for a spherical solid shell is

$$\mathbf{Y}_S(r) = \mathbf{M}(r)\mathbf{C} \tag{6.1.9}$$

where $\mathbf{M}(r)$ is the matrix whose column vectors are the six solution vectors $\mathbf{y}_i$ with the appropriate ρ, g, μ and

$$\mathbf{C} = (C_1(s), C_2(s), C_3(s), C_4(s), C_5(s), C_6(s))^T \tag{6.1.10}$$

is the coefficient vector. Note that $\mathbf{C}$, $\mathbf{K}$, $\mathbf{M}(r)$, $\mathbf{Z}(r)$, $\mathbf{Y}_S(r)$ and $\mathbf{Y}_C(r)$ are all 's' dependent.

For a non-self-gravitating earth, the third and sixth vectors in (6.1.6) and the last two rows in the other vectors are identically zero, thus the matrices $\mathbf{Z}$, $\mathbf{K}$, $\mathbf{M}$ and $\mathbf{C}$ are reduced to 4x2, 2x1, 4x4 and 4x1 matrices respectively.

For a uniform inviscid fluid core, the $\mathbf{Z}$ matrix just above the core at $r = c$ can be expressed as (Wu & Peltier, 1982; Dahlen & Fels, 1978; Chinnery, 1975; Crossley & Gubbins, 1975; Smylie & Mansinha 1971):

$$\mathbf{Z}(c) = \begin{bmatrix} -c^{n}\delta_g/g(c) & 0 & 1 \\ 0 & 1 & 0 \\ 0 & 0 & \rho(c)\, g(c) \\ 0 & 0 & 0 \\ c\,\delta_g & 0 & 0 \\ 2(n-1)c^{n-1}\delta_g & 0 & 4\pi G\, \rho(c)\, \delta_g \end{bmatrix} \tag{6.1.11}$$

and for a non-self-gravitating earth, the first column and the last two rows in **Z** can be dropped.

The coefficients in **K** and **C** are to be determined by the continuity boundary conditions at the interface at r = c and the surface boundary conditions for an impulsive load :

$$\mathbf{B} = \begin{bmatrix} T_{rn}(a) \\ T_{\theta n}(a) \\ Q_n(a) \end{bmatrix} = \begin{bmatrix} \dfrac{-g_0(2n+1)}{4\pi a^2} \\ 0 \\ \dfrac{-G(2n+1)}{a^2}\delta_g \end{bmatrix} \tag{6.1.12}$$

where a is the radius of the earth (Farrell 1972, Longman 1963). For a non-self-gravitating earth, the last row in **B** can be dropped.

For a two-layer earth model that is composed of a viscoelastic shell and an inviscid liquid sphere, the solution in the shell is (Wu 1990):

$$\mathbf{Y_S}(r)=\mathbf{M}(r)\mathbf{M}^{-1}(c)\mathbf{Z}(c)\mathbf{T}^{-1}(a)\mathbf{B} \tag{6.1.13}$$

and the solution within the inner sphere is

$$\mathbf{Y_C}(r) = \mathbf{Z}(r)\mathbf{T}^{-1}(a)\mathbf{B} \tag{6.1.14}$$

where $$\mathbf{T}(a) = \mathbf{M}(a)\mathbf{M}^{-1}(c)\mathbf{Z}(c) \tag{6.1.15}$$

but has rows 1, 2 and 5 deleted.

For a general multi-layer spherical earth model, although the solution **Y** can still be written in terms of **M**(r) at each layer and the boundary condition **B** at the earth surface, it is not practical to actually derive the final solution analytically. The algebraic expressions are too long to manage. So, the $\mathbf{Y_S}$ is usually obtained numerically by propagating the formal solution (the first 3 ones in eq. 6.1.6) of the sphere through the layers to the surface using the Matrix Techniques (Cathles, p30-33) and Runge-Kutta Techniques (Cathles, p33-34). These formal solutions are linearly combined to match the boundary conditions at the surface and to obtain a specific solution in the transformed s and n domains.

Traditionally, the solution at the earth's surface is expressed in terms of the Love Numbers h_n, l_n and k_n which are defined by (Peltier, 1974; Farrell, 1972; Love, 1911):

$$\begin{bmatrix} U_n(a,s) \\ V_n(a,s) \\ \Phi_n(a,s) \end{bmatrix} = \frac{a\, g_0}{M_E} \begin{bmatrix} h_n(a,s)/g_0 \\ l_n(a,s)/g_0 \\ -(1+k_n(a,s)) \end{bmatrix} \tag{6.1.16}$$

where M_E is the mass of the earth and g_0 is the surface gravity.

Following Wu (1990, 1978) and Peltier (1985), the solutions for the impulsive load can be inverted to the time domain: First, express the Love numbers as the ratio of two analytical functions W(s) and D(s), (e.g. $h_n(s)= W(s)/D(s)$) where the determinant function is embedded in the denominator so that the eigenspectrum s_n^i can be obtained from the roots of D(s)=0. From the elastic asymptote h_n^E (which is defined by $h_n^E = \lim_{s\to\infty} h_n(s) = W^E/D^E$) and the viscous part of the Love number $h_n^V(s)$ where

$$h_n^V(s) = h_n(s) - h_n^E = \frac{W(s) - (D(s)\, W^E)/D^E}{D(s)} \tag{6.1.17}$$

the residue for the i^{th} eigenmode r_i^h and the solution in the time domain can be obtained as follows:

$$h_n(t) = h_n^E\, \delta(t) + \sum_{i=1}^{m} r_i^{hn}\, e^{s_n^i t} \tag{6.1.18}$$

$$r_i^{hn} = \frac{W(s_n^i)}{\left[\frac{\partial}{\partial s} D(s)\right]_{s_n^i}} \tag{6.1.19}$$

where m is the number of eigenmodes. Note that $D(s)W^E/D^E$ do not appear in the numerator of the residue since $D(s_n^i)=0$.

For Heaviside loading, the solution can be written as:

$$h_n^H(t) = h_n^E - \sum_{i=1}^{m} \frac{r_i^{hn}}{s_n^i} \left(1 - e^{s_n^i t}\right) \tag{6.1.20}.$$

The ratio r_i^{hn}/s_n^i is called the excitation strength that represents contribution of a mode to the total relaxation.

6.2 EFFECTS OF NON-SELF-GRAVITATION

Non-self-gravitation means that the gravitational potential of the load and gravitational perturbation due to the earth deformation are neglected. This often results in a simplification in formulation and, therefore, is advantageous if we know what are effects of the simplification in final solutions. In this section, the effect of neglecting self-gravitation is explored by comparing results of self and non-self-gravitation for the uniform sphere and the two-layer model of a viscoelastic mantle overlying an inviscid liquid core.

6.2.1 Homogeneous Sphere

Let ρ, ν, μ, a, and g denote density, viscosity, shear modulus, the radius and surface gravity of the uniform earth respectively. The shear modulus in the s domain μ_S is defined as

$$\mu_s = \frac{\mu s}{s + \frac{\mu}{\nu}} \tag{6.2.1}$$

Following Wu & Peltier (1982), the unified expressions for Love numbers (h_n and l_n) in s-domain are derived. Let t be the characteristic relaxation time which is the negative inverse of the eigenvalue (root) s ($t = -1/s$). The residues (r_n^h and r_n^l) and exciting strengths (e_n^l and e_n^h) which are defined as the ratio of the residues over the eigenvalue (for example, $e_n^l = \frac{r_n^l}{s}$), for both the self-gravitating and non-self-gravitating cases, are:

$$l_n(s) = -\frac{1}{\frac{(2n^2 + 4n + 3)\mu_s}{a\rho g_n} + n} \tag{6.2.2}$$

$$t = T_m + T_g \tag{6.2.3}$$

$$r_n^l = \frac{T_g}{n(T_m + T_g)^2} \tag{6.2.4}$$

$$e_n^l = \frac{r_n^l}{s} = -\frac{1}{n\left(1+\frac{T_m}{T_g}\right)} \tag{6.2.5}$$

The radial components, h_n, r_n^h, and e_n^h are related to the tangential components by the following equations.

$$\frac{h_n(s)}{l_n(s)} = \frac{r_n^h}{r_n^l} = \frac{e_n^h}{e_n^l} = \frac{(2n+1)n}{3} \tag{6.2.6}$$

In the above equations from (6.2.2) to (6.2.5),

$$T_m = \frac{\nu}{\mu} \tag{6.2.7}$$

is the Maxwell time,

$$T_g = \frac{\left(2n^2+4n+3\right)\nu}{na\rho g_n} \tag{6.2.8}$$

is a part of the relaxation time that is associated with the buoyancy force, and

$$g_n = \frac{(2n+1)\delta_a - 3\delta_g}{2(n-1)} g \tag{6.2.9}$$

is the only factor that depends on the setting of the switches.

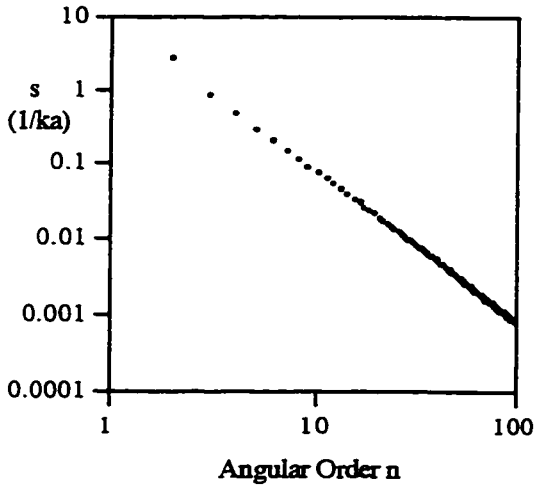

Figure 6.1 Relaxation diagram for the uniform earth Model 1 with self-gravitation but without prestress advection term.

First, let us see what happens if the prestress advection is not included ($\delta_a = 0$). For the self-gravitating case ($\delta_g = 1$),

$$s = \frac{1}{\nu\left[\frac{2(n-1)\left(2n^2+4n+3\right)}{3na\rho g} - \frac{1}{\mu}\right]} \tag{6.2.10}.$$

This is plotted in Fig. 6.1 for the uniform sphere with averaged values of ρ, ν, and μ of the real earth (see Model 1 in Table 6.1). Here s is positive for all n. This means that the relaxation would grow exponentially if the prestress advection term is neglected. This is not physically feasible because observed relaxation is always of exponential decay.

For the non-self-gravitating case ($\delta_g = 0$), $\delta_a = 0$ yields $s = 0$. Mathematically, this is saying that the earth's response to the load does not change with time and there is no relaxation (or the relaxation time is infinite). This is also unrealistic. So, these results support Wu's conclusion (1992b) that prestress advection is necessary for the description of a glacial isostatic process. Therefore, from now on, we set $\delta_a = 1$, and focus on the effects of self-gravitation.

Because g_n is the only factor that contains δ_g, all the differences between self-gravitating and non-self-gravitating cases are due to different expressions of g_n :

For the self-gravitating case ($\delta_g = 1$),

$$g_n = g \qquad (6.2.11),$$

and for the non-self-gravitating case ($\delta_g = 0$),

$$g_n = \frac{2n+1}{2(n-1)} g \qquad (6.2.12).$$

Comparing eqs. 6.2.11 and 6.2.12 implies that neglecting self-gravitation yields a larger and n-dependent gravity g_n (eq. 6.2.12). This larger g_n results in shorter T_g (eq. 6.2.8) and overall relaxation time t (eq. 6.2.3). However, when n approaches infinity, (2n+1)/(2n-2) goes to 1. Therefore, the non-self-gravitation solutions converge to the self-gravitating ones. In practice, the difference between self-gravitation and non-self-gravitation becomes insignificant for n>30. These can also be seen in Fig. 6.2b where the eigenvalues s_i of the uniform earth model (Model 1) for both non-self-gravitating and non-self-gravitating cases are plotted. The eigenvalues s_i for the non-self-gravitating case have a slightly larger magnitude (Fig. 6.2b) than those for the self-gravitating case (see also Amelung & Wolf, 1994) for small n. In the other panels of Fig. 6.2, Love Number spectra for n=5, the residues, and the exciting strengths are also shown.

Further comparison between the self-gravitating (SG) and non-self-gravitation (NSG) solutions of the uniform earth model (Model 1) shows that:

(i) Self-gravitation has no effect on the number of eigenmodes for the uniform earth (see equations from 6.2.2 to 6.2.12).

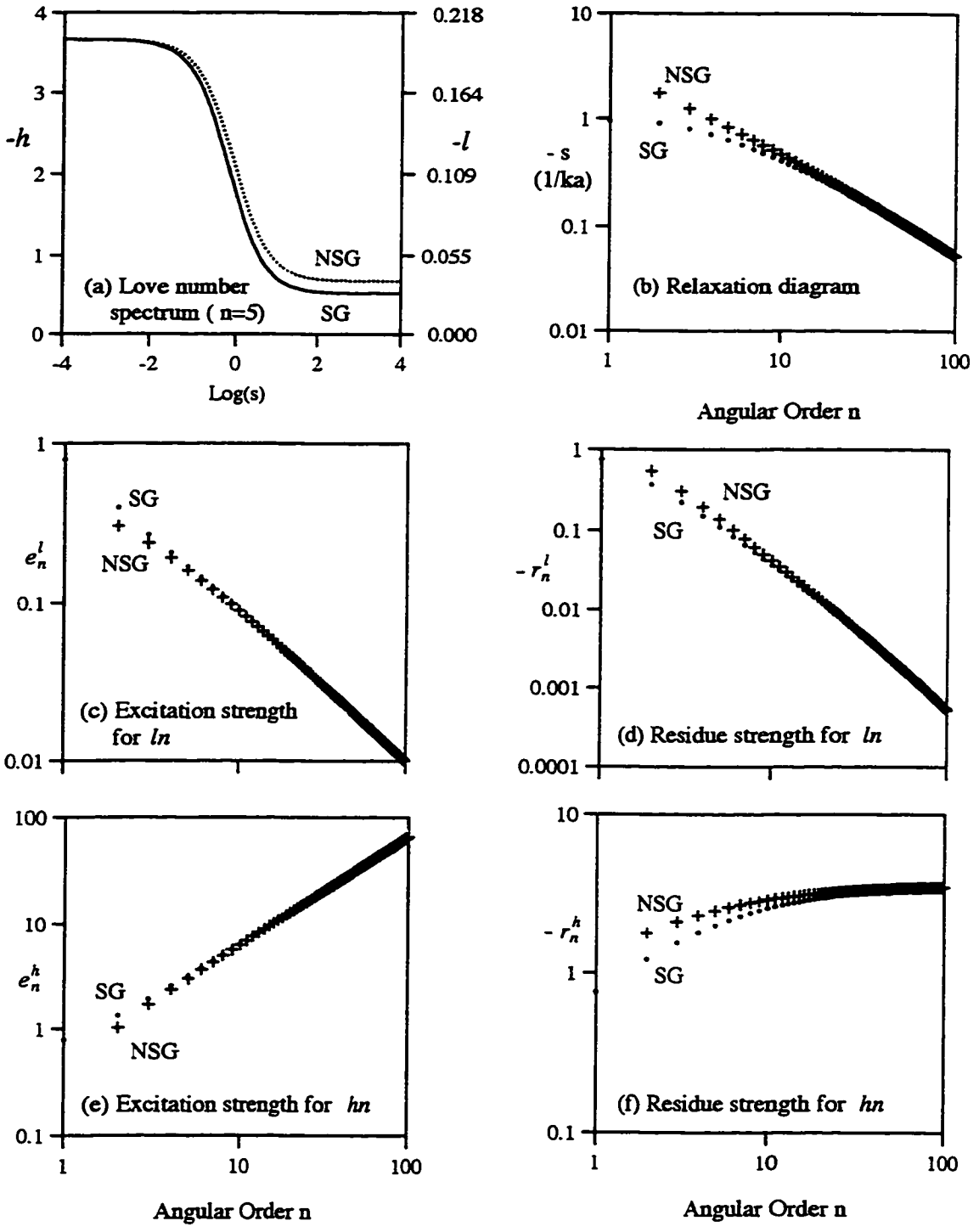

Figure 6.2 Comparison between results of self-gravitation (SG) and non-self-gravitation (NSG) for the uniform earth Model 1 (see Table 6.1 for the physical parameters) with the prestress advection term included.

(ii) For the non-self-gravitating case, the magnitude of the elastic asymptote (i.e. obtained by taking the limit $s \rightarrow \infty$ in eqs. 6.2.2 & 6.2.6, or by taking the large s asymptote in Fig. 6.2a) is greater than that for the self-gravitating case. Physically, this larger amplitude of deformation is due to the larger gravity for the non-self-gravitating earth.

(iii) In both self-gravitating and non-self-gravitating cases, the isostatic asymptotes are the same (i.e. obtained by taking the limit $s \rightarrow 0$ in eqs. 6.2.2 & 6.2.6), so are the small s asymptotes in Fig. 6.2a. For the h_n Love numbers, both approaches $-(2n+1)/3$, whereas for l_n, both approach $-1/n$. Since, the isostatic asymptotes are independent of gravity, self-gravitation has no effect on them.

(iv) The excitation strength for the self-gravitating case has larger amplitude - since excitation strength depends on the difference between the elastic and the isostatic asymptotes. However, this difference falls below 5% for n>5 (see Fig. 6.2c, e).

(v) The residue for the self-gravitating case has smaller amplitude since they are related to the excitation strength and the relaxation time through eq. 6.2.5.

In general, the differences between the two cases increase with decreasing n. This reaches the extreme situation at n = 1: while $g_n = g$ and all other solutions are normal for the self-gravitating case, $g_n = \infty$ and all the other solutions become abnormal for the non-self-gravitating case. This is because neglecting gravity of n=1 load, like that in the non-self-gravitating case, leaves an unbalanced surface force driving the earth to infinite and no regular solution exists. Only when both the surface force and opposing gravity are taken into account, can the total force on the center of mass of the earth remains in balance and regular solutions exist for the self-gravitating case. In contrast, any other harmonic load exerts a total of zero net surface force and zero gravity force on the earth, thus solutions for the non-self-gravitating case exist. In the following, the n=1 mode will not be considered.

6.2.2 Mantle over Inviscid Fluid Core

The previous subsection shows that there is only one single mode for a uniform sphere. What happens if there is an additional layer? Is the number of eigenmodes still the same for both self-gravitation and non-self-gravitation cases? In the following, a two-layer model that is made of a viscoelastic shell overlying an inviscid liquid core is considered. Again, the symbols ρ, ν, μ, a, and g_0 denote density, viscosity, shear modulus, the radius, and

surface gravity of the outer solid shell and ρ_c, c, and g_c denote the density, radius, and surface gravity for the inner fluid core.

Non-Self-Gravitating Case

The Love number spectrum at the surface of the outer shell has been derived using a symbolic manipulation program called Theorist (now called Mathview). They can be expressed explicitly as ratios of polynomials in s:

$$h_n(s) = -\frac{1}{3}\frac{(2n+1)^2 g_0 (\nu s + \mu)(KUA\, s + KUB)}{\zeta (KDA\, s^2 + KDB\, s + KDC)} \tag{6.2.13}$$

where: $d\rho = \rho_c - \rho$, $\zeta = \frac{4\pi G a}{3 g_0}$ is unity when normalized (Wu & Peltier, 1982) and

$$KDA = n(n+1)(2n+1)^2 CAA\, \rho\, d\rho\, g_0\, g_c\, \nu^2 \tag{6.2.14}$$

$$+ 4(n+2)(n-1)(2n+3)(2n-1)\mu^2\nu^2 CAD + 2(2n+1)\mu\nu^2 CGA$$

$$KDB = 2(2n+1)\mu\nu[n(n+1)(2n+1) CAA\, \rho\, d\rho\, g_0\, g_c + \mu\, CGA]$$

$$KDC = n(n+1)(2n+1)^2 \mu^2 \rho\, d\rho\, g_0\, g_c\, CAA$$

$$KUA = \nu[n(n+1)(2n+1)\, d\rho\, g_c\, CAA + 2\mu\, CAC]$$

$$KUB = n(n+1)(2n+1)\mu\, d\rho\, g_c\, CAA$$

$$CGA = CAB\, d\rho\, g_c + CAC\, \rho\, g_0$$

$$CAA = \frac{c^4}{a^4} - a^{-2n-3} c^{2n+3} - a^{2n-1} c^{-2n+1} + 1$$

$$CAB = -\frac{(n^4 + 2n^3 - n^2 - 2n + 3)(2n+1)}{a} + \frac{(n+2)(n+1)(n-1)(2n+1)c^4 n}{a^5}$$

$$-(n+1)(n-1)(2n^2+4n+3)a^{2n-2}c^{-2n+1} + (n+2)(2n^2+1)a^{-2n-4}c^{2n+3}n$$

$$CAC = \frac{(n^4 + 2n^3 - n^2 - 2n + 3)(2n+1)c^3}{a^4}$$

$$- \frac{(n+2)(n+1)(n-1)(2n+1)n}{c} - \frac{(n+2)(2n^2+1)a^{2n-1}n}{c^{2n}}$$

$$+ (n+1)(n-1)(2n^2+4n+3)a^{-2n-3}c^{2n+2}$$

$$CAD = \frac{(a^4+c^4)(n^4+2n^3-n^2-2n+3)(2n+1)^2}{(2n+3)(2n-1)a^5c}$$

$$- \frac{(a^{2n-2}+a^{-2n-4}c^{4n+2})(2n^2+1)(2n^2+4n+3)}{(2n+3)(2n-1)c^{2n}}$$

$$- 2\frac{(n+2)(n+1)(n-1)cn}{a^3}$$

The eigen-spectrum can be determined from the denominator of eq. (6.2.13). Because it is a second order polynomial in "s" (Amelung & Wolf, 1994), there is a maximum of 2 eigenvalues:

$$s_{\pm} = \frac{(2n+1)\mu\{\mu[\pm\sqrt{\Delta a} - CGA] - n(n+1)(2n+1)g_0\rho g_c d\rho\, CAA\}}{\nu\, CAG} \qquad (6.2.15)$$

where

$$\Delta a = g_0^2\rho^2\, CAC^2 + g_c^2\, d\rho^2\, CAB^2$$

$$+ 2\rho\, g_0\, d\rho\, g_c[CAB\ CAC - 2(n+2)(n+1)(n-1)(2n+3)(2n-1)n\, CAA\ CAD]$$

$$CAG = 4(n+2)(n-1)(2n+3)(2n-1)\mu^2\, CAD$$

$$+ (2n+1)\{2\mu g_0\rho\, CAC + g_c([n(n+1)(2n+1)g_0\rho\, CAA + 2\mu\, CAB]\, d\rho)\}$$

The meaning of these eigenmodes becomes obvious for large n. Retaining terms with the highest order in n, the two eigenvalues become:

$$s_1 = -\frac{\rho g_0 a}{2n\nu} \qquad (6.2.16)$$

$$s_2 = -\frac{c(2n\mu + a\rho g_0)\mu\, d\rho\, g_c}{[4n^2\mu^2 + 2n(a\rho g_0 + c\, d\rho\, g_c)\mu + c\rho\, d\rho\, g_0 g_c]\nu} \qquad (6.2.17).$$

Since s_1 has the same large n-limit as that for the uniform sphere (which can be easily verified using eqs. 6.2.3, 6.2.7, 6.2.8, and 6.2.9), it represents the main mode M0 (Wu & Peltier 1982). Because s_2 vanishes when c=0 or dρ=0 (i.e. uniform earth), it represents the core mode C0 (Wu & Peltier 1982) that is due to the buoyancy force at the interface r=c.

Self-Gravitating Case

The self-gravitating case has also been solved. Here, the lengthy expressions (see Amelung & Wolf, 1994 for explicit form) are skipped and only the results are summarized. These results basically confirm that (1) the number of eigenmodes is the same for both self-gravitating and non-self-gravitating cases and (2) the self-gravitating earth behaves like a non-self-gravitating earth at large n (Amelung & Wolf, 1994). The Love number spectrum can also be expressed in a form similar to equation (6.2.13) for the non-self-gravitating case but the definitions of the KUA, KUB, KDA, KDB & KDC are different.

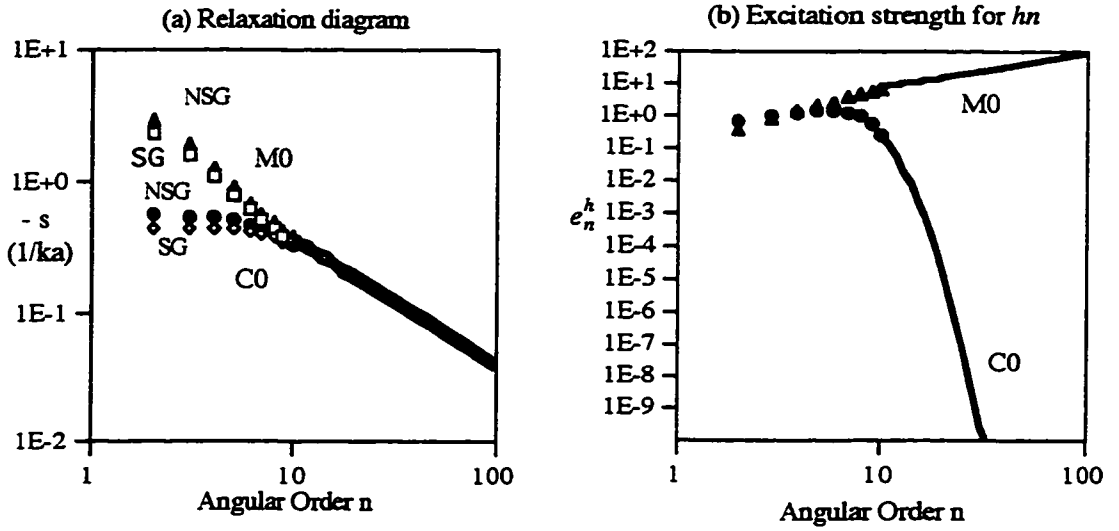

Figure 6.3 Relaxation spectra and excitation strengths for Model 2 (see Table 6.1) which has a solid shell overlying a fluid core. (a) The relaxation spectra for the self-gravitating case (SG) is compared to the non-self-gravitating case (NSG). (b) Excitation strength for the non-self-gravitating case is shown for the two modes.

Fig. 6.3a compares the eigenvalues (i.e. the inverse of the relaxation times) between the two cases for Model 2 (see Table 6.1 for physical parameters). The solid symbols represent the NSG (non-self-gravitating) case and the open symbols represent the SG (self-

gravitating) case. The upper branch in each case is for the M0 mode while the lower branch is for the C0 mode. Once again, like the uniform earth, Fig. 6.3a shows that non-self-gravitation results in faster relaxation times (Amelung & Wolf, 1994). Fig. 6.3b shows that the excitation strengths for the C0 modes become insignificant for n>10.

In summary, self-gravitation has no effect on the number of eigenmodes but the relaxation times for a NSG earth are faster than those for the self-gravitating earth for small n. This difference however decreases with increasing n and finally the two solutions converge at large n.

Table 6.1 Physical Properties of the Incompressible Earth Models

Parameters	Model 1	Model 2	Model 3	Model 4	Model 5	Model 6	Model 7	Model 8	Model 9
Density of outer shell r (kg/m^3)	5517	4448	3572	3572	4448	5517	5517	5517	5517
Shear modulus of outer shell m (10^{11} Pa)	1.4519	1.7364	0.8281	1.4519	1.4519	0.8281	0.8281	1.4519	1.4519
viscosity of outer shell n (10^{21} Pa-s)	1.0	1.0	1.0	1.0	1.0	1.0	1.0	1.0	∞
radius of inner sphere c (10^6 m)	-	3.4855	5.7000	5.7000	3.4855	5.7000	5.7000	5.7000	6.221
Density of inner sphere r_c (kg/m^3)	-	10977	6288	6288	10977	5517	5517	5517	5517
Shear modulus of inner sphere m_c (10^{11} Pa)	-	0	1.7147	1.4519	1.4519	1.7147	1.7147	1.4519	1.4519
viscosity of inner sphere n_c (10^{21} Pa)	-	0	10.0	1.0	1.0	10.0	1.0	10.0	1.0
Number of Eigenmodes	1	2	4	2	2	3	3	3	2

6.3 INTERPRETING GRAVITATIONAL RELAXATION MODES: TWO-LAYER SOLID EARTH MODEL WITH NON-SELF-GRAVITATION

Next, we explore the relationship between eigenmodes and discontinuities in density, viscosity, and shear modulus of a spherically stratified earth model. This is important for interpreting normal modes of gravitational relaxation.

We consider non-self-gravitating earth models with two viscoelastic layers, i.e. a viscoelastic shell overlying a viscoelastic sphere. Analytical solutions are derived and special cases are discussed. These special cases include earth models with discontinuities in any one or two or all of the three physical parameters (density, shear rigidity, and viscosity). Because the difference between self-gravitation and non-self-gravitation becomes insignificant for n>30, these solutions for large n derived for the non-self-gravitating case are also valid for the self-gravitating case.

Through this exercise, the number of eigenmodes for a particular earth model is established, a better understanding of the nature of those modes is achieved, and the residues or excitation strength can be calculated with higher accuracy. Furthermore, insight to solving the dense singularities problem (Wu & Ni, 1996; Han & Wahr, 1995) is gained and a simple way of avoiding the singularities is suggested.

6.3.1 The Singularity Problem

In the following, ρ, ν, μ, a, and g_0 denote density, viscosity, shear modulus, the radius and surface gravity of the outer solid shell and ρ_c, ν_c, μ_c, c, and g_c denote the corresponding parameters for the inner solid sphere. After lengthy algebraic derivations, DET(s) (D(s) in eq. 6.1.17) that is used to find the eigen-spectrum can be simplified and explicitly written out in terms of s to reveal some insights on the singularity problem:

$$\mathrm{DET}(s) = \mathrm{DA}\,\frac{\mu s}{s+\gamma} + \mathrm{DB}\,\frac{\mu_c s}{s+\gamma_c} + \mathrm{DC}\,\frac{\mu_c (s+\gamma)}{\mu (s+\gamma_c)} + \mathrm{DD}\left(\frac{\mu_c s}{s+\gamma_c}\right)^2 + \mathrm{DE}\,\frac{\mu \mu_c s^2}{(s+\gamma)(s+\gamma_c)} + \mathrm{DF}\,\frac{\mu_c^2 (s+\gamma) s}{\mu (s+\gamma_c)^2} + \mathrm{DG}\left(\frac{\mu s}{s+\gamma}\right)^2 + \mathrm{DH} \qquad (6.3.1)$$

where $\gamma = \frac{\mu}{\nu}$, $\gamma_c = \frac{\mu_c}{\nu_c}$ are the inverse of the Maxwell times for the shell and the core, respectively; DA, DB, DC, DD, DE, DF and DG are model-dependent coefficients that are functions of n, a, c, ρ, $d\rho$ ($=\rho_c - \rho$), g_0 and g_c (see Appendix A). It is obvious now that this determinant function (DET(s) in eq. 6.3.1) that is used in the numerical search for the roots is singular at $s = -\gamma$ or $s = -\gamma_c$ (Fang & Hager, 1995; Han & Wahr, 1995; James, 1991). However, this derivation also shows that W(a,s) (in eq. 6.1.17) also contains $(s+\gamma)^2 (s+\gamma_c)^2$ in its denominator, and thus can canceled out those in DET(s). Therefore, there is no real singularity problem. The reason for the problem in the numerical approach is that the cancellation does not happen numerically. To avoid the singularities in the numerical approach, simply use the determinant of the simplified Love number's expression (after the cancellation) as the characteristic function for searching the eigenvalues, in other words, multiply the old Determinant function by $(s+\gamma)^2 (s+\gamma_c)^2$. For a general N-layer earth, the multiplier is $\prod_{i=1}^{N} (s+\gamma_i)^2$ where $\gamma_i = \frac{\mu_i}{\nu_i}$ and the subscript i refers to the i^{th} layer.

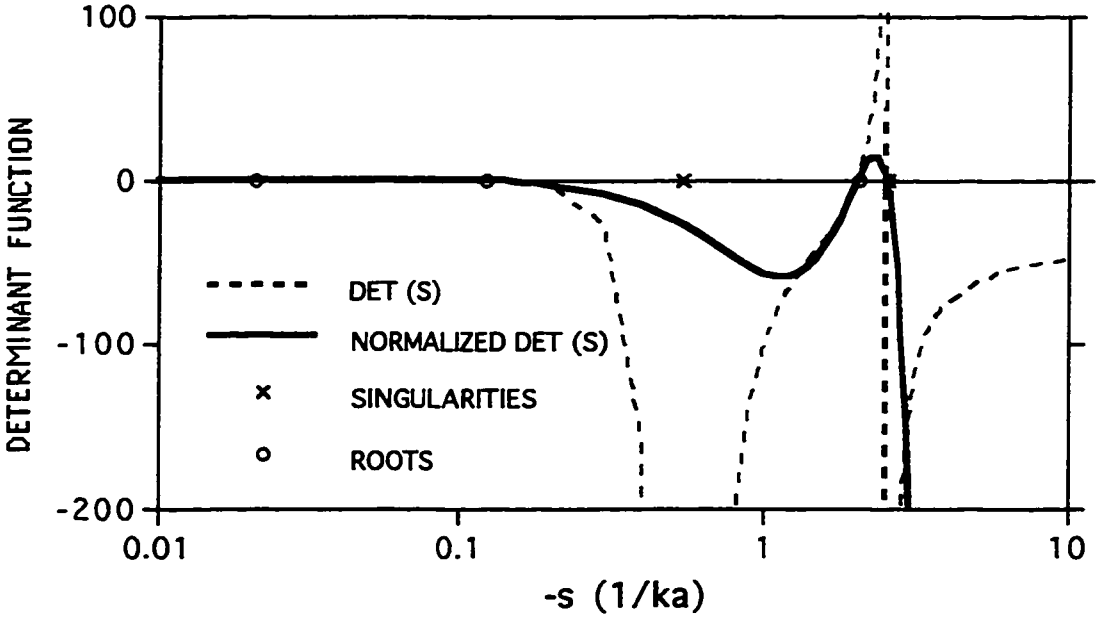

Figure 6.4 Determinant function DET(s) (dashed line) and the normalized DET(s) (solid line) for a solid shell overlying a solid core are plotted as a function of -s.

Fig. 6.4 shows an example: the dashed line, which represents DET(s) for a two-layer earth, has two singularities (represented by the x symbols) - one around s=-0.54 while the other is very close to a root (represented by the circle) near s=-2.56. Unless DET(s) is carefully sampled, the root near s=-2.56 can be easily mistaken as a singularity! This problem can become very severe when the number of layering increases. To remove the singularities, DET(s) has been normalized by multiplying $(s+\gamma)^2 (s+\gamma_c)^2$ to give the solid line which is well behaved and from which the roots can be found numerically without any difficulty.

6.3.2 General Solution for the Two-layer Model

For a general case with discontinuities in density, shear modulus and viscosity across the interface at r = c, the Love numbers in the s-domain can be written as:

$$h_n(s) = \frac{1}{3} \frac{g_0 (\nu s + \mu) (CUA\ s^3 + CUB\ s^2 + CUC\ s - CUD)}{\zeta (CDA\ s^4 + CDB\ s^3 + CDC\ s^2 + CDD\ s + CDE)} \qquad (6.3.2)$$

$$l_n(s) = \frac{2}{3} \frac{g_0 (\nu s + \mu) (CVA\ s^3 + CVB\ s^2 + CVC\ s + CVD)}{\zeta a^4 \mu \nu n (n+1) (CDA\ s^4 + CDB\ s^3 + CDC\ s^2 + CDD\ s + CDE)}$$

where, again, CUA, CUB, CUC, CUD, CVA, CVB, CVC, CVD, CDA, CDB, CDC, CDD and CDE are just model-dependent coefficients and are given in Appendix A. Because the denominator in (eq. 6.3.2) is a 4th order polynomial of "s", there can only be a maximum of 4 eigenvalues associated with the 2-layer incompressible earth.

The residues that are derived from eq. 6.1.19 are given by:

$$r^h_i = \frac{1}{3} \frac{g_0 (\nu s_i + \mu) (CUA\ s_i^3 + CUB\ s_i^2 + CUC\ s_i - CUD)}{\zeta (4\ CDA\ s_i^3 + 3\ CDB\ s_i^2 + 2\ CDC\ s_i + CDD)} \qquad (6.3.3)$$

$$r^l_i = \frac{2}{3} \frac{g_0 (\nu s_i + \mu) (CVA\ s_i^3 + CVB\ s_i^2 + CVC\ s_i + CVD)}{\zeta a^4 \mu \nu n (n+1) (4\ CDA\ s_i^3 + 3\ CDB\ s_i^2 + 2\ CDC\ s_i + CDD)}$$

For large n, the coefficients in eqs. (6.3.2) and (6.3.3) can be greatly simplified and the above expressions also become valid for the self-gravitating case (at large n). The 4 eigenvalues for large n are:

$$s_1 = R_{\mu\nu}\left(R_{\mu\nu} - \tfrac{1}{2}\right) + RSQ\left(-R_{\mu\nu} + \tfrac{1}{2}\right)$$

$$s_2 = -R_{\mu\nu}\left(R_{\mu\nu} + \tfrac{1}{2}\right) + RSQ\left(R_{\mu\nu} + \tfrac{1}{2}\right) \qquad (6.3.4)$$

$$s_3 = -R_{\mu\nu}\left(R_{\mu\nu} + \tfrac{1}{2}\right) + RSQ\left(R_{\mu\nu} - \tfrac{1}{2}\right)$$

$$s_4 = R_{\mu\nu}\left(R_{\mu\nu} - \tfrac{1}{2}\right) - RSQ\left(R_{\mu\nu} + \tfrac{1}{2}\right)$$

where

$$RSQ = \left[\frac{2}{3} R_{\mu\nu}\left\{R_{\mu\nu}^3 - \frac{9}{2}\frac{[(2\nu_c + \nu)\rho g_0 + (\nu_c + \nu) c\, d\rho\, g_c]\,\mu^2\,\mu_c^2}{n\,\nu^2\,\nu_c^2\,(\mu + \mu_c)^2}\right\}^{\frac{1}{3}} + \frac{1}{3} R_{\mu\nu}^2\right]^{\frac{1}{2}}$$

and $R_{\mu\nu} = \dfrac{(\nu + \nu_c)\,\mu\,\mu_c}{(\mu + \mu_c)\,\nu\,\nu_c}$. Since n is large, the terms within the braces remain positive, thus, all the eigenvalues must be real for large n. When $n \to \infty$, $s_1 = s_2 = 0$ and $s_3 = s_4 = -R_{\mu\nu}$. The four modes represented by s_1, s_2, s_3, and s_4 can be denoted as M0, M1, T1 and T2. Their physical origin and meaning are to be discussed in the next paragraph and in the following sections.

Fig. 6.5 shows the relaxation diagram and the excitation strengths for a two-layer model (Model 3 in Table 6.1) that has an interface at 671 km depth. Several observations can be made: (1) T1 and T2 relax much faster than M0 which in turn is faster than M1 (Fig. 6.5a). (2) The excitation strengths for vertical displacement Love number, h_n, (Fig. 6.5b), show that the M0 mode is always the dominant mode and the excitation strengths of the M1 mode decline quickly with increasing n. Similarity between visual pattern of M0 and M1 in Fig. 6.5b and that of M0 and C0 of the 2-layer-solid-liquid model in Fig. 6.3b suggests that the M0 and M1 modes are due to the buoyancy forces at the surface and the interface respectively. (3) For the excitation strengths for horizontal displacement l_n (Fig. 6.5c), the M1 mode is the dominant mode at small n and M0 becomes the dominant mode only for n>7. (4) At small n, the excitation strengths for l_n are just as strong as h_n, or even stronger (compare Fig. 6.5b & c); only when n>10, do the excitation strengths for l_n become weaker. (5) T1 and T2 modes carry excitation strengths that are smaller than that for the M0 mode by two or more orders of magnitude (Fig. 6.5b & c). (6) The excitation strengths for l_n can become negative for the viscoelastic modes T1 & T2, but their magnitude are quite small (Fig. 6.5c).

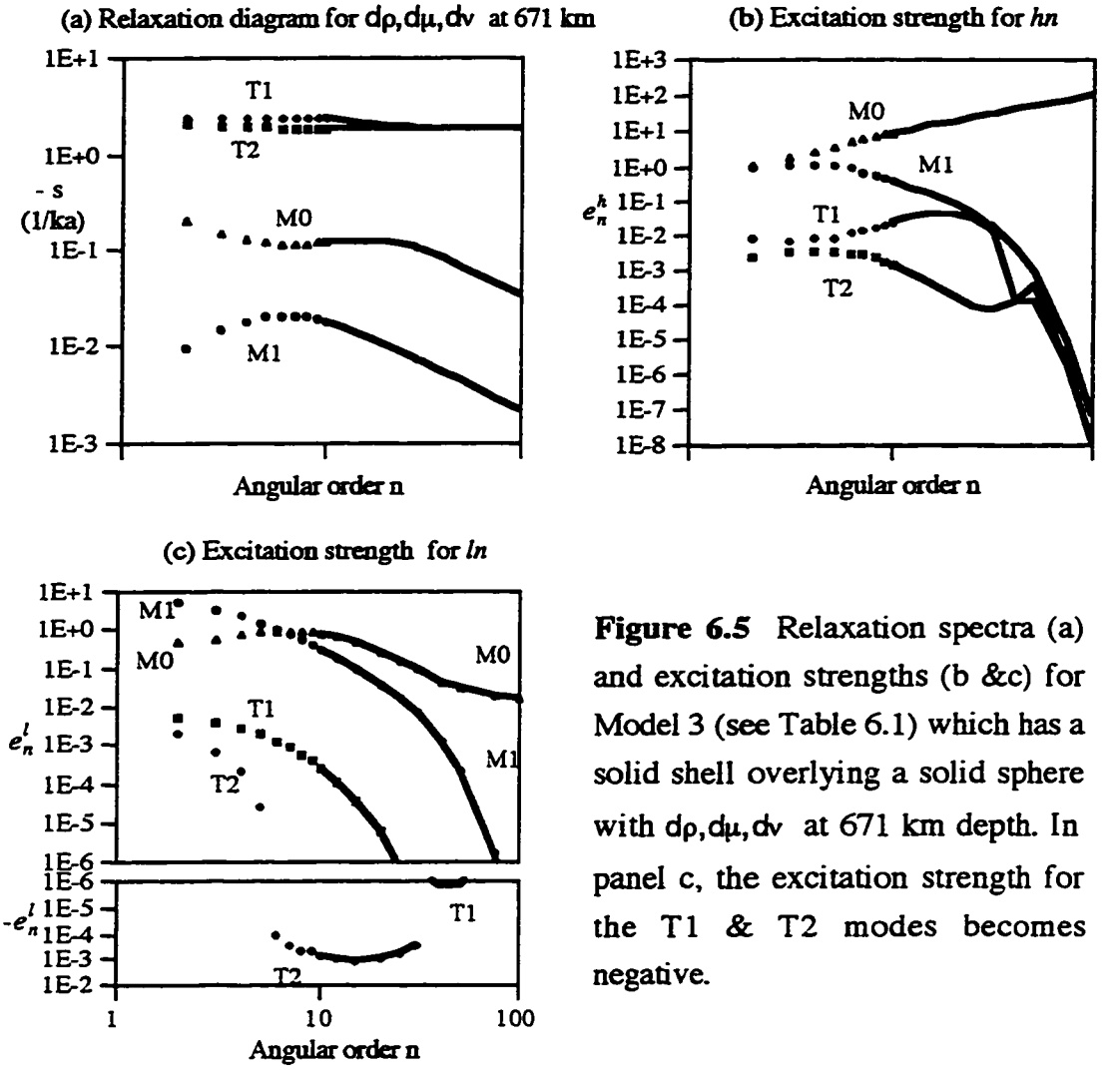

Figure 6.5 Relaxation spectra (a) and excitation strengths (b &c) for Model 3 (see Table 6.1) which has a solid shell overlying a solid sphere with dρ,dμ,dv at 671 km depth. In panel c, the excitation strength for the T1 & T2 modes becomes negative.

6.3.3 Density Change Only

When there is only a density contrast across the interface, i.e. $\mu = \mu_c$ and $\nu = \nu_c$, $(\nu s + \mu)^2$ can be factored out of the numerator and denominator of the love numbers' expressions (eq. 6.3.2), yielding simpler expressions:

$$h_n(s) = \frac{1}{3}\,\frac{g_0\,(\nu s+\mu)^3\,(D s+E)}{\zeta\,(\nu s+\mu)^2\,(A s^2+B s+C)} = \frac{1}{3}\,\frac{g_0\,(\nu s+\mu)\,(D s+E)}{\zeta\,(A s^2+B s+C)}$$

$$l_n(s) = \frac{2}{3} \frac{g_0 (\nu s + \mu)(F s + H)}{\zeta a^4 \mu \nu n (n+1)(A s^2 + B s + C)} \tag{6.3.5}$$

where $A = \frac{CDA}{\nu^2}$, $B = \frac{CDD\,\mu - 2\,CDE\,\nu}{\mu^3}$, $C = \frac{CDE}{\mu^2}$, $D = \frac{CUA}{\nu^2}$, $E = -\frac{CUD}{\mu^2}$,

$F = \frac{CVA}{\nu^2}$, $H = \frac{CVD}{\mu^2}$.

The denominator in eq. (6.3.5) is a second order polynomial of s so that there can only be a maximum of 2 eigenvalues. The eigenvalues of these buoyancy modes can be expressed as:

$$s_i = \frac{-B \pm \sqrt{B^2 - 4AC}}{2A} \tag{6.3.6}$$

The residues are given by:

$$r_i^h = \frac{1}{3} \frac{g_0 (\mu + \nu s_i)(E + D s_i)}{\zeta (B + 2A s_i)} \tag{6.3.7}$$

$$r_i^l = \frac{2}{3} \frac{g_0 (\nu s_i + \mu)(F s_i + H)}{\zeta a^4 \mu \nu n (n+1)(B + 2A s_i)}$$

Again, for large n the two roots are simplified as:

$$s_1 = \frac{-1}{\nu \left[\frac{1}{\mu} + 2 \frac{n}{\rho g_0 a} \right]} \tag{6.3.8}$$

$$s_2 = \frac{-1}{\nu \left(\frac{1}{\mu} + \frac{4n}{d\rho g_c c} \right)} \tag{6.3.9}$$

Eqs. 6.3.8 and 6.3.9 give excellent approximations to the exact eigenvalues (eq. 6.3.6) for n>30. The expression for s_1 (Eq. 6.3.8) explicitly shows its origin, the buoyancy force ρg_0 at the Earth's surface, therefore it is the M0 mode. The expression for s_2 (eq. 6.3.9) explicitly shows that it is due to the buoyancy force $d\rho g_c$ at the interface r = c, therefore it is the M1 mode.

The relaxation diagram and excitation strengths for Model 4 (in Table 6.1) with a pure density discontinuity at 671 km depth are plotted in Fig. 6.6 and those for Model 5 (in Table 6.1) with a density jump at the core-mantle-boundary are in Fig. 6.7. Compare visual patterns of excitation strengths for *hn* of modes M0 and M1 in Fig. 6.6b and Fig. 6.7b with that of M0 and M1 of the general 2-layer-solid-solid Model 3 in Fig. 6.5b, their similarity attests that M0 and M1 of the general Model 3 are indeed buoyancy modes. The absence of the T1 and T2 modes in Fig. 6.6 and Fig. 6.7 (for Models 4 and 5 that have only a density-change) implies that T1 and T2 are due to changes in viscosity and/or shear modulus in Model 3.

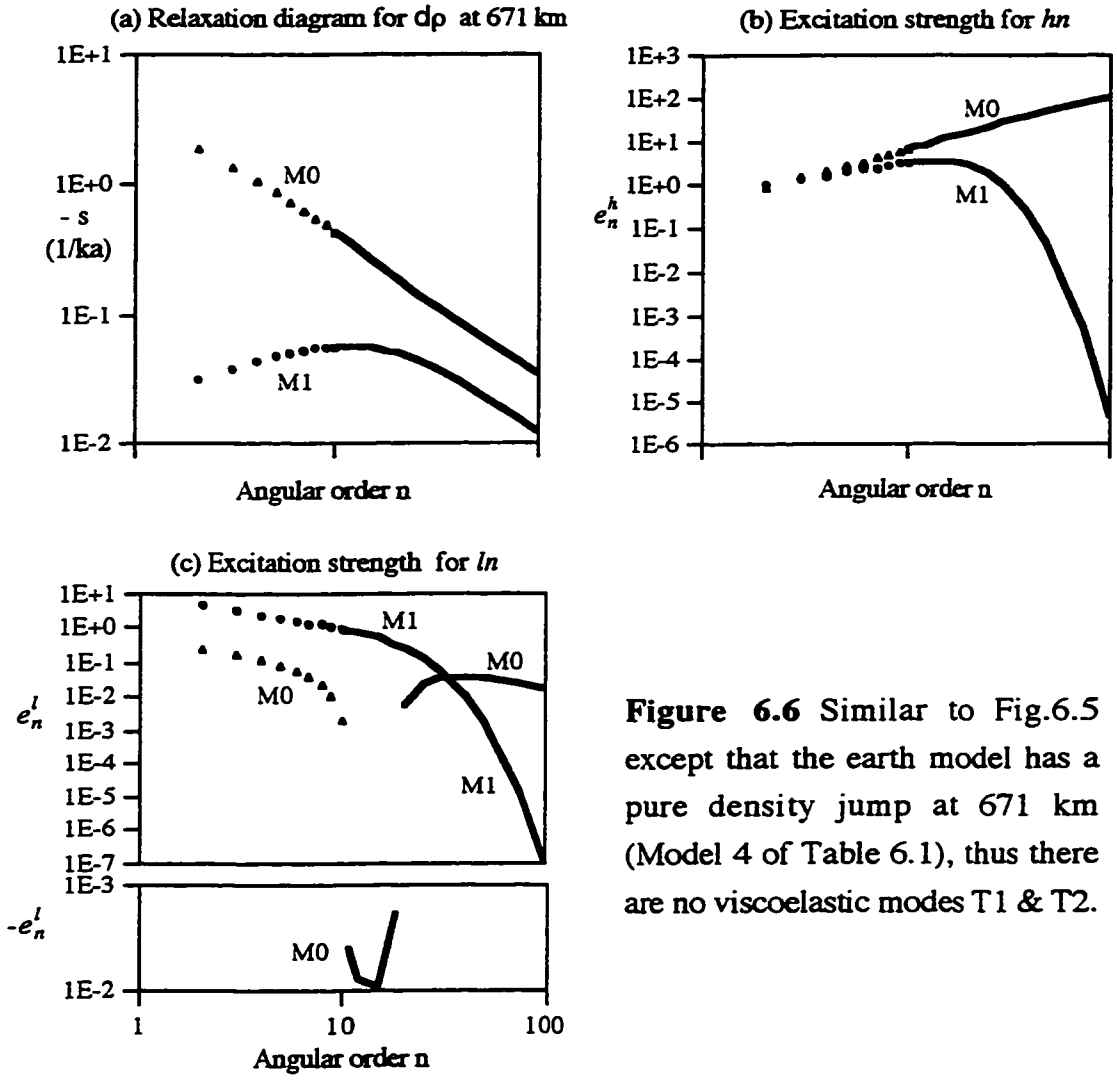

Figure 6.6 Similar to Fig.6.5 except that the earth model has a pure density jump at 671 km (Model 4 of Table 6.1), thus there are no viscoelastic modes T1 & T2.

Other important observations are listed as follows: (1) For h_n, comparison of the excitation strength of M1 mode between Models 4 and 5 (Fig. 6.6b & Fig. 6.7b) shows that M1 mode has larger excitation strength when the interface is shallower. (2) For l_n (Fig. 6.6c), the M1 mode in Model 4 is dominant for n<30 and the excitation strength for the M0 mode can become negative. (3) Comparisons of the relaxation diagrams and excitation strengths of h_n Model 5 (solid core) and Model 2 (liquid core) show that C0 mode of the liquid core (Model 2) relaxes faster (Fig. 6.5a vs. Fig. 6.7a) and carries larger excitation strengths (Fig. 6.5b vs. Fig. 6.7b) than M1 mode of the solid core (Model 5).

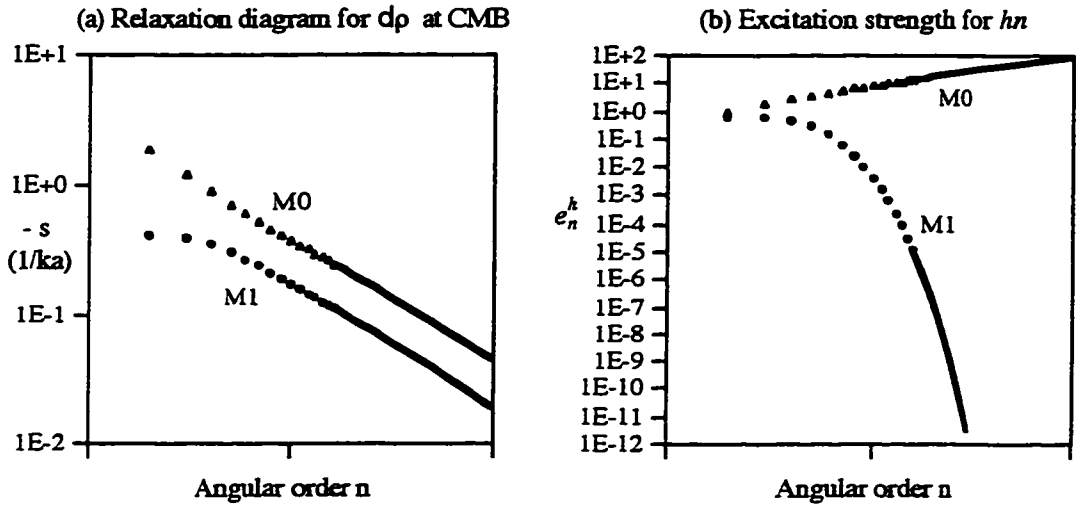

Figure 6.7 Similar to Fig. 6.6 except that the pure density jump is at the core-mantle boundary (CMB) (Model 5 of Table 6.1).

6.3.4 No Density Change

To find exact nature of T1 and T2 modes, set dρ=0 and only allow changes in shear modulus and viscosity. Thus, CDE=CUD=CVD=0 and a "s" can be factored out of the numerator and denominator in the general expressions of the love numbers (eq. 6.3.2). This yields the following simplified expressions:

$$h_n(s) = \frac{1}{3}\,\frac{g_0\,(\nu\, s + \mu)\,(CUA\, s^2 + CUB\, s + CUC)}{\zeta\,(CDA\, s^3 + CDB\, s^2 + CDC\, s + CDD)} \qquad (6.3.11)$$

$$l_n(s) = \frac{2}{3} \frac{g_0 (\mu + \nu s) (CVA\ s^2 + CVB\ s + CVC)}{\zeta a^4 \mu \nu n (n+1) (CDA\ s^3 + CDB\ s^2 + CDC\ s + CDD)}$$

There are a maximum of three eigenvalues:

$$s_1 = -\frac{1}{3} \frac{CDB}{CDA} + CDS + CDT \tag{6.3.12}$$

$$s_2 = -\frac{1}{3} \frac{CDB}{CDA} - \frac{1}{2} (CDS + CDT) + i \frac{1}{2} \sqrt{3} (CDS - CDT)$$

$$s_3 = -\frac{1}{3} \frac{CDB}{CDA} - \frac{1}{2} (CDS + CDT) - i \frac{1}{2} \sqrt{3} (CDS - CDT)$$

where

$$CDS = \left[\frac{1}{54} \left(-2 \left[\frac{CDB}{CDA}\right]^3 - 27 \frac{CDD}{CDA} + 9 \frac{CDB\ CDC}{CDA^2}\right) + \sqrt{\Delta}\right]^{\frac{1}{3}} \tag{6.3.13}$$

$$CDT = \left[\frac{1}{54} \left(-2 \left[\frac{CDB}{CDA}\right]^3 - 27 \frac{CDD}{CDA} + 9 \frac{CDB\ CDC}{CDA^2}\right) - \sqrt{\Delta}\right]^{\frac{1}{3}}$$

and the discriminator is:

$$\Delta = \frac{1}{4} \frac{CDD^2}{CDA^2} + \frac{1}{54} \frac{(2\ CDC^2 - 9\ CDB\ CDD)\ CDC}{CDA^3}$$

$$+ \frac{1}{108} \frac{(4\ CDB\ CDD - CDC^2)\ CDB^2}{CDA^4} \tag{6.3.14}.$$

The residues are:

$$r^h_i = \frac{1}{3} \frac{g_0 (\nu s_i + \mu) (CUA\ s_i^2 + CUB\ s_i + CUC)}{\zeta (3\ CDA\ s_i^2 + 2\ CDB\ s_i + CDC)} \tag{6.3.15}.$$

$$r^l_i = \frac{2}{3} \frac{g_0 (\mu + \nu s_i) (CVA\ s_i^2 + CVB\ s_i + CVC)}{\zeta a^4 \mu \nu n (n+1) (3\ CDA\ s_i^2 + 2\ CDB\ s_i + CDC)}$$

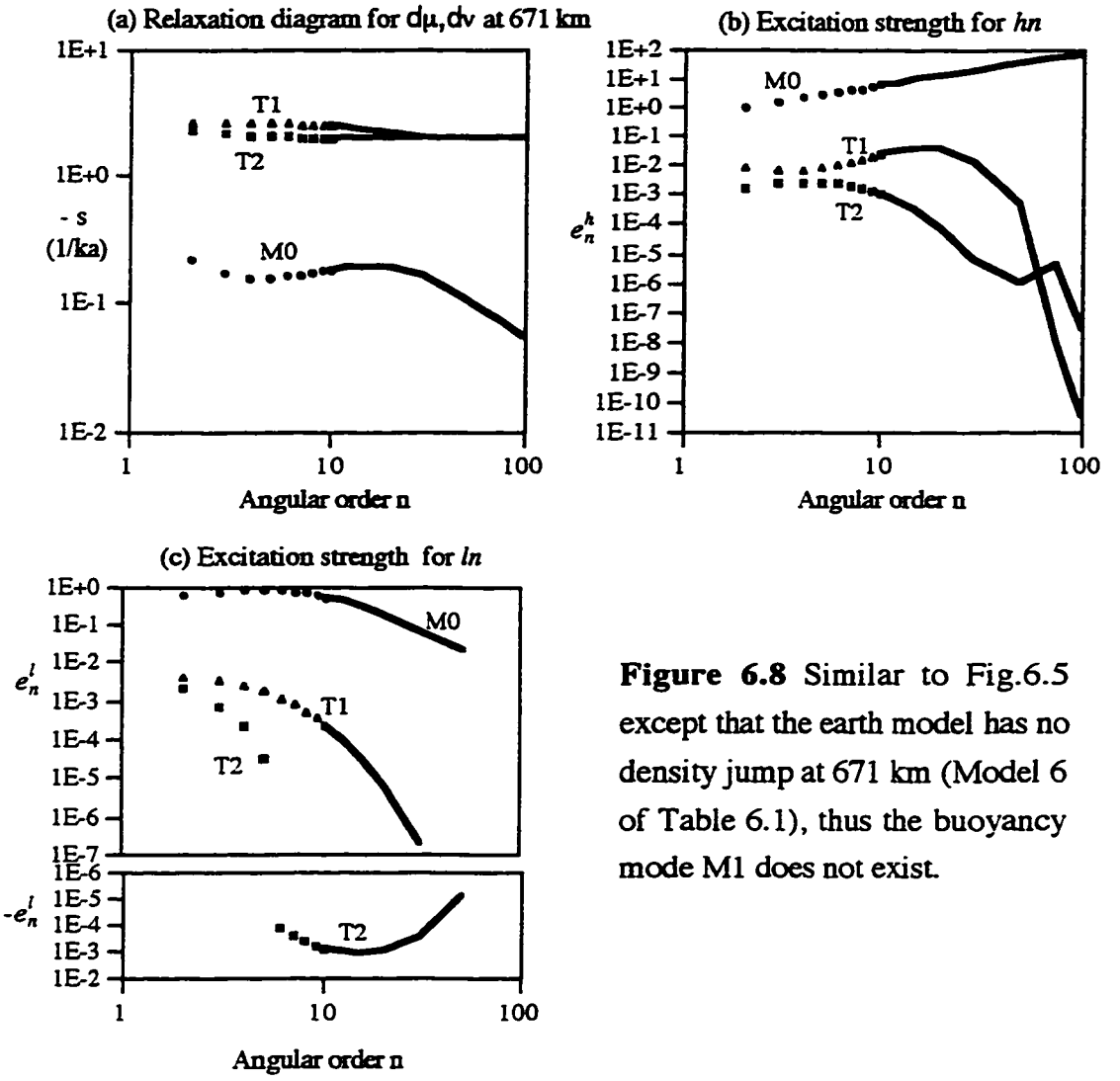

Figure 6.8 Similar to Fig.6.5 except that the earth model has no density jump at 671 km (Model 6 of Table 6.1), thus the buoyancy mode M1 does not exist.

For large n, the discriminator $\Delta = -\frac{1}{54}\frac{(\nu_c+\nu)^5\,\mu^5\,\mu_c^5\,\rho\,g_0}{n\nu^6\nu_c^5(\mu+\mu_c)^5}$ is negative, and the three roots are all real. The two roots, s_2 and s_3, are close together with the same large n limit $-\frac{(\nu+\nu_c)\mu\mu_c}{(\mu+\mu_c)\nu\nu_c}$ that is the same as those for T1 and T2 of the general two-solid-layer model (Model 3) and can be interpreted as negative ratio of the 'effective' viscosity and the 'effective' shear modulus of the model. Therefore the two roots are for the two viscoelastic (or transition) modes. The other root, s_1, has a limit of $-\frac{\rho g_0 a}{2n\nu}$ for large n. This is the same limit as that for the uniform sphere (which can be easily verified using eqs. 6.2.3, 6.2.7, 6.2.8, and 6.2.9 by dropping the Maxwell time term that can be neglected at large n in eq.

6.2.3) and is the same as the limit for s_1 for the general two layer model (Model 3), and that for s_1 mode for the density-change-only two-layer model (dropping the term $1/\mu$). So, s_1 can be identified as the M0 mode.

Fig. 6.8 shows the relaxation diagram and excitation strengths for a two-layer model with changes in viscosity and shear modulus but not in density (Model 6 in Table 6.1). The presence of T1 and T2 confirms that they are caused by the discontinuity in viscosity and shear rigidity. On the other hand, the absence of M1 implies that M1 mode can only be generated by density change in Model 3, not anything else.

6.3.5 A Finite Change in Shear Modulus or/and Viscosity

Success in identifying the origins of the buoyancy mode M1 and viscoelastic modes T1 and T2 in terms of material contrast encouraged attempts to further break down T1 and T2 as a group: Is the T1 mode caused by the discontinuity in shear modulus and the T2 mode by that in viscosity? or vice versa?

Analytical solutions are derived for models with a discontinuity only in shear modulus (Model 7 in Table 1), or only in viscosity (Model 8), or in both shear modulus and viscosity under condition that the ratio of the two is continuous across the boundary. It is found that a change in either shear modulus or viscosity introduces the two transition modes simultaneously. The results for models 7 and 8 are plotted in Figs. 6.9 and 6.10 respectively. Comparing the two figures, the largest difference between the two models is in the behavior of the main mode M0. When the pure change is in shear modulus (Fig. 6.9), the M0 behaves like that of the uniform sphere (Fig. 6.5). When the change is in viscosity (Fig. 6.10), the relaxation time increases at small n which is shown as a decrease of (-s) in the relaxation diagram (Fig. 6.10a).

When the ratio of shear modulus and viscosity μ/ν is kept constant across the interface, i.e. $\mu_c / \nu_c = \mu / \nu$ but allow both of them to change, the discriminator in eq. 6.3.14 becomes zero. Thus, two of three real roots become equal. In fact, the denominator in the expressions (eq. 6.3.11) can be factored into:

$$\mathrm{CDA}\, s^3 + \mathrm{CDB}\, s^2 + \mathrm{CDC}\, s + \mathrm{CDD} = \mathrm{CDA} \left(\frac{\mu}{\nu} + s\right)^2 (s - s_1) \ .$$

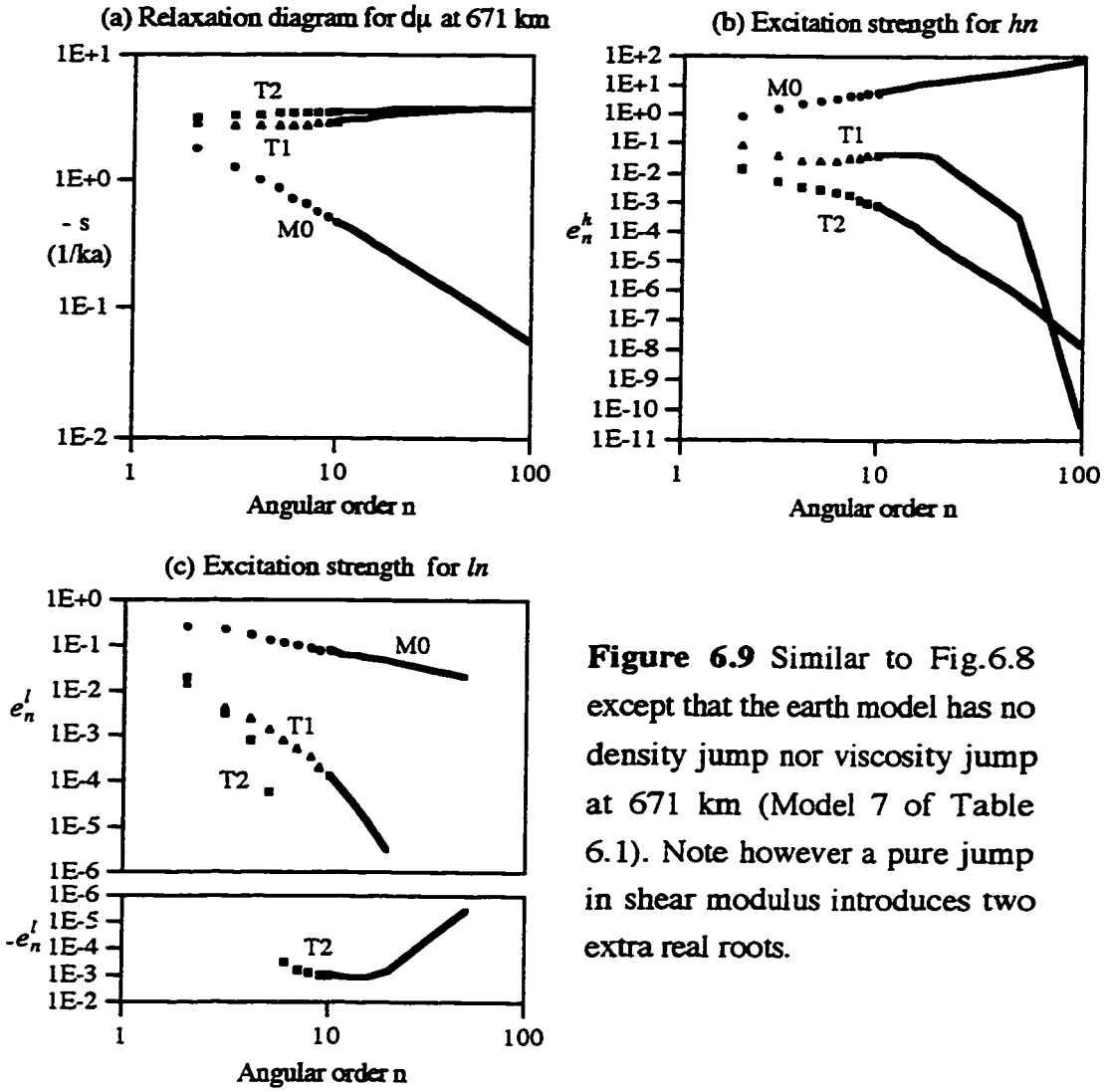

Figure 6.9 Similar to Fig.6.8 except that the earth model has no density jump nor viscosity jump at 671 km (Model 7 of Table 6.1). Note however a pure jump in shear modulus introduces two extra real roots.

Therefore, roots are $s_1 = -\frac{\mu}{\nu} + 3\,CDS$, $s_2 = s_3 = -\frac{\mu}{\nu}$ where CDS is given by eq. 6.3.13 with D=0. The first root, s_1, is for the main mode M0 and the other two are for the viscoelastic modes. However, when one substitutes s_2 or s_3 into the expressions for the residues (eq. 6.3.15), the residues are all exactly zero. In fact, both numerator and denominator of the expressions (eq. 6.3.11) contain the factor $\left(\frac{\mu}{\nu} + s\right)^2$, thus after cancellation, there is the only root for the M0 mode. Hence, there is no viscoelastic mode when the ratio is continuous. The residues for the M0 mode are:

$$r^h_1 = \frac{1}{9}\,\frac{(CUA\ s_1^2 + CUB\ s_1 + CUC)\ \nu\ g_0}{\zeta\ CDA\ \ CDS} \qquad (6.3.16).$$

and $$r^l_1 = \frac{2}{9} \frac{g_0 (CVA\ s_1^2 + CVB\ s_1 + CVC)}{\zeta a^4 \mu n (n+1)\ CDA\ CDS}$$

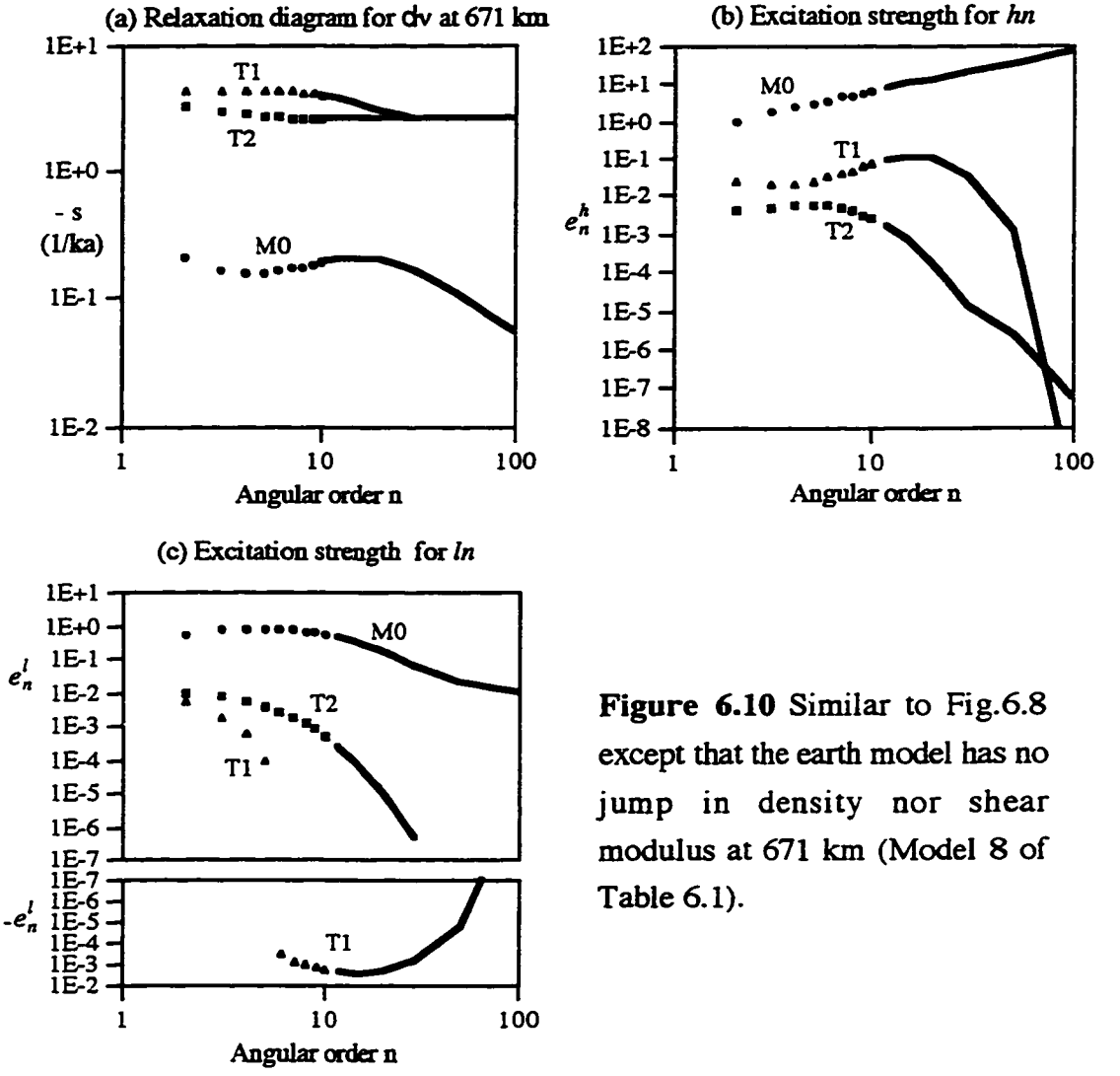

Figure 6.10 Similar to Fig.6.8 except that the earth model has no jump in density nor shear modulus at 671 km (Model 8 of Table 6.1).

6.3.6 Infinite Change in Viscosity - Elastic Lithosphere

Effects of the lithosphere on postglacial rebound have been studied by a number of investigators (Peltier, 1984; Wu & Peltier, 1982). McConnell (1968) argued that a lithosphere is required so that the observed decrease in the relaxation time spectrum at shorter wavelengths could be explained. Peltier (1984) directly inferred lithospheric

thickness from relative sealevel data along the U.S. east coast. Wolf (1984) derived analytical solution for an incompressible and hydrostatically prestressed viscoelastic non-self-gravitating sphere surrounded by a thick elastic shell with uniform density. The solutions here are more generalized than Wolf's (1984) by including discontinuities in density and shear rigidity.

The lithosphere is simulated by setting $\nu = \infty$ in the general two-layer model (Model 3) while keeping $d\rho \neq 0$, $\mu \neq \mu_c$ and finite ν_c. The love numbers can then be simplified from those for the general two-layer model (Model 3, eq. 6.3.2) to the following:

$$h_n(s) = \frac{1}{3}\frac{g_0\,(\mathrm{CLUA}\ s^2 + \mathrm{CLUB}\ s + \mathrm{CLUC})}{\zeta\,(\mathrm{CDLA}\ s^2 + \mathrm{CDLB}\ s + \mathrm{CDLC})} \tag{6.3.17}$$

$$l_n(s) = \frac{2}{3}\frac{g_0\,(\mathrm{CLVA}\ s^2 + \mathrm{CLVB}\ s + \mathrm{CLVC})}{\zeta a^4 \mu\, n(n+1)\,(\mathrm{CDLA}\ s^2 + \mathrm{CDLB}\ s + \mathrm{CDLC})}$$

where $\mathrm{CLUA} = \frac{\mathrm{CUA}}{\nu}$, $\mathrm{CLUB} = \frac{\mathrm{CUB}}{\nu}$, $\mathrm{CLUC} = \frac{\mathrm{CUC}}{\nu}$,

$$\mathrm{CLVA} = \frac{\mathrm{CVA}}{\nu^2}\ ,\ \mathrm{CLVB} = \frac{\mathrm{CVB}}{\nu^2}\ ,\ \mathrm{CLVC} = \frac{\mathrm{CVC}}{\nu^2}\ , \tag{6.3.18}.$$

$$\mathrm{CDLA} = \frac{\mathrm{CDA}}{\nu^2}\ ,\mathrm{CDLB} = \frac{\mathrm{CDB}}{\nu^2}\ ,\mathrm{CDLC} = \frac{\mathrm{CDC}}{\nu^2}\ ,$$

In fact, ν does not actually exist in the expressions of the above coefficients because it factors out with that in the numerators.

The denominator of (6.3.17) shows that there is a maximum of two eigenvalues even when $d\rho \neq 0$ and $\mu \neq \mu_c$: the lithospheric (viscoelastic) mode L0 and the main mode M0. Fig. 6.11 plots the relaxation diagram and excitation strengths for Model 9 (Table 6.1) which has a 150 km thick lithosphere with $d\rho = 0$ and $\mu = \mu_c$. As is well known (e.g. McConnell, 1968; Wu & Peltier, 1982; Wolf, 1984) the lithosphere behaviors like a low pass filter that blocks out the shorter wavelength deformations. This is confirmed in Fig. 6.11 where the excitation strength of the main mode M0 for *hn* is suppressed for large n (Fig. 6.11b) and the relaxation time for the M0 mode decreases with increasing n for n>15 (Fig. 6.11a). At very large n, the relaxation time of both the M0 and L0 modes approaches the viscoelastic asymptote $-\frac{\mu\mu_c}{(\mu+\mu_c)\nu_c}$. The L0 mode itself carries very little strength for *hn* (Fig. 6.11b)

except near n=5 where the L0 and M0 branches crosses in the relaxation diagram. Fig. 6.11c shows that the excitation strength of the M0 mode for l_n, although greater than that for L0 in magnitude, becomes negative for n>10. Thus, large but negative excitation strengths occur when an elastic lithosphere exists.

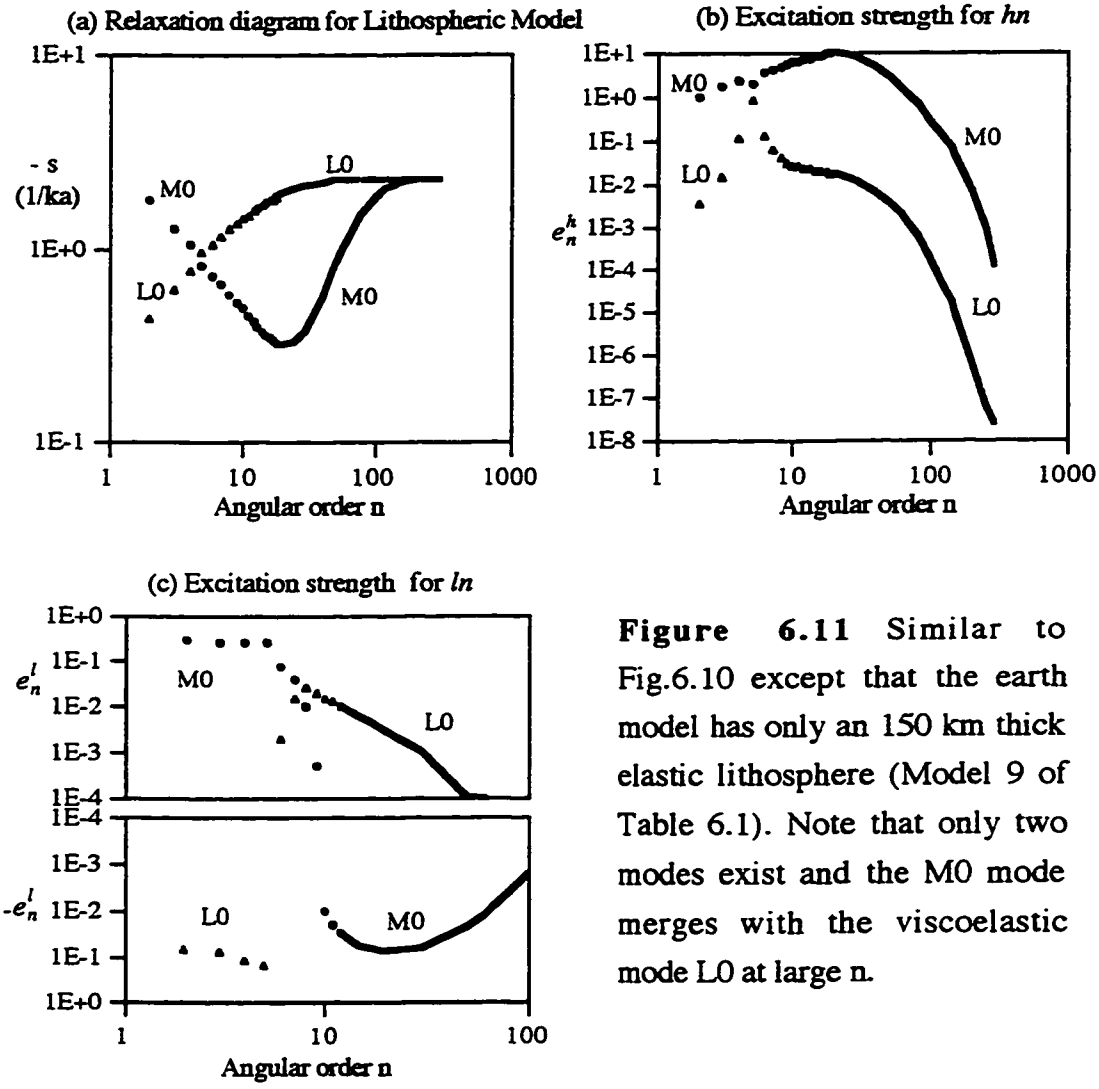

Figure 6.11 Similar to Fig.6.10 except that the earth model has only an 150 km thick elastic lithosphere (Model 9 of Table 6.1). Note that only two modes exist and the M0 mode merges with the viscoelastic mode L0 at large n.

6.3.7 Summary

For incompressible and non-self-gravitating two-layer viscoelastic earth models, analytical solutions derived here established that a pure density jump introduces an extra buoyancy mode and a discontinuity in μ/ν introduces two viscoelastic modes simultaneously. However, an elastic lithosphere of infinitely large viscosity only introduces one extra mode (L0) regardless of density and shear modulus changes.

The viscoelastic modes carry very small excitation strengths that can be negative for the horizontal displacements (l_n). When there is an elastic lithosphere, positive and negative excitation strengths can have comparable magnitude. This may pose a numerical problem in the construction of Green's functions for horizontal displacement, strain or stress because the excitation strengths have to be calculated to high precision otherwise the Green's functions constructed will not be very reliable. Thus, in order to interpret VLBI or strain/stress data, highly accurate numerical schemes, that can reproduce these analytical benchmark results, must be used.

Finally, a way of obtaining a singularity free determinant function has been suggested. This is particularly useful in the numerical search for the eigenspectrum and for accurate determination of the Green's functions for the interpretation of postglacial rebound data when the earth model is composed of a large number of uniform layers.

CHAPTER 7

APPLYING THE FINITE ELEMENT METHOD TO SPHERICAL EARTH

This chapter is concerned with the construction of a finite element spherical earth model for postglacial rebound studies. We shall consider non-self-gravitating case first and calibrate the model with the spectral method using the results derived the previous chapter. Once the spherical finite element model has been demonstrated to work then it can be used to study postglacial isostatic adjustment of a laterally heterogeneous spherical earth.

The spherical finite element model is very computational intensive even for a supercomputer and for calibration purpose we are only interested in simple spherical earth models with long wavelength harmonic loads, therefore we start with coarse grids in the spherical finite element model. To model more realistic loads, refined grids are needed.

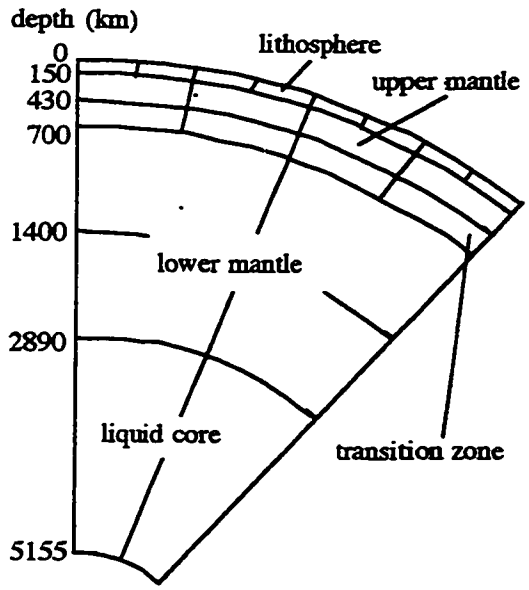

Figure 7.1 A profile of the six-layer finite element mesh

7.1 THE FINITE ELEMENT GRID

The grid consists of thick spherical shells with elements covering from the surface of the earth to the bottom of the outer core at 5155 kilometers depth. The whole three dimensional finite element grid consists of 6 spherical layers of elements. The thickness of the each layer is largely dictated by the well known discontinuities inside the Earth. A

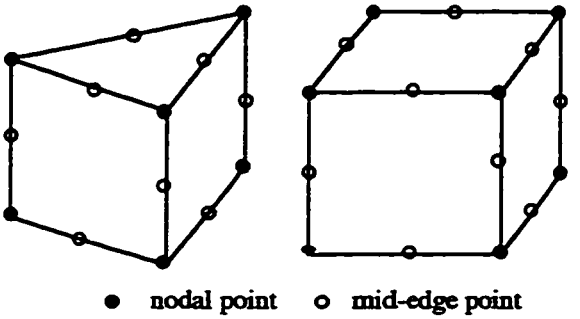

Figure 7.2 Prism and cubic elements.

profile of the layering is shown in figure 7.1. From the surface downwards, the layers consists of a 150 km thick lithosphere, the upper mantle, the transition zone and the lower mantle which is composed of two layers of elements to maintain the aspect ratio between the radial dimension and the tangential dimension of the elements to be close to the ideal ratio of 1. The bottom layer is the liquid core.

To fit the spherical surface, two kind of elements are used: second order prisms and cubes (see Fig. 7.2). Second order element means that between nodes at two neighboring corners there is an extra node along the edge. To mimic a spherical surfaces, the edges that connect the corner nodal points do not have to be straight lines but may be slightly curved. Also a second order shaping function is used to interpolate the displacements and stresses within an element. The prisms are used in the two polar areas whereas the cubes are used everywhere else. To best utilize the computing resources, a fine 5° by 5° grid is assigned to the lithosphere since this is where the load is applied and where displacements are calculated. Below the lithosphere, the grids get coarser with increasing depth: 10° by 10° elements are for the upper mantle (between 150 km depth and 700 km depth), and 20° by 20° elements for the lower mantle and the liquid core. Figure 7.3 shows part of the layout of the three kind of grids covering from the Greenwich Meridian to 20° longitude and from the north pole to 40° colatitude. The rest of the grid can be deduced from symmetry.

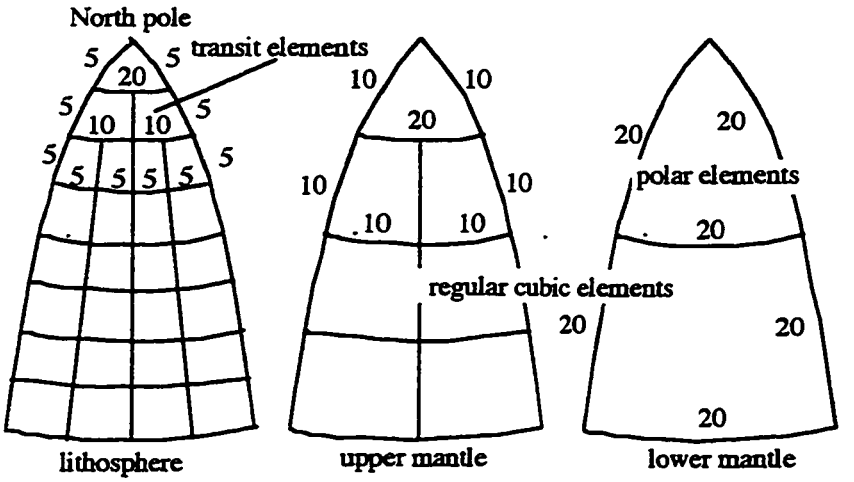

Figure 7.3 Three kinds of grid in the mesh. Numbers are in angular degree.

This spherical grid has 31094 nodes and 4122 elements. It is too large to run on the IBM-RS 6000 servers at University of Calgary. It had to be run on the Fujitsu supercomputer at the High Performance Computing Center. It needs about 2 giga-bytes of swap disk and takes 1753.7 second CPU time to calculate the elastic deformation which only takes one time increment and one iteration. In comparison, a similar computation for a flat-earth model only takes about 50 second.

7.2 BENCHMARKING

For the purpose of calibration, we consider a non-self-gravitating and incompressible uniform earth model (Model 1 in Table 6.1) under an n=2 harmonic load which is left on the earth's surface at t=0. The spatial distribution of the n = 2 harmonic load is shown in figure 7.4 along with its discrete form for the finite element computation. The load only varies with colatitude and is the same for all elements along the same parallel.

Figure 7.5 compares the elastic and viscoelastic radial displacements computed for the spherical finite element model with the analytical solution of spectral method from the previous chapter. The viscoelastic displacement is computed at two thousand years (t=2 ka) after application of the load. The difference between the results computed by the two methods is around 1 or 2% for the most part. The exceptions are in the two polar areas and around colatitude 55 and 125 degree. In the polar areas, the larger differences may be attributed to the coarse elements there. On the other hand, large percentage differences around colatitude 55 and 125 degree are due to the fact that the displacements are close to zero there. The difference is smaller for t=2 ka than the elastic ones at t=0. In general, the comparison shows that the finite element calculation is acceptable. Better agreement with the analytical results can be expected with a finer grid.

It is unfortunate that the Fujitsu supercomputer was shut down permanently after the above calibrations. But, we have already shown that our spherical finite element model can be used to calculate elastic and viscoelastic deformation of non-self-gravitating earth. Given that more powerful supercomputers are available, we can design finite element grids with finer spatial resolution that can handle higher harmonic loads and use it to study postglacial rebound in laterally heterogeneous spherical non-self-gravitating earth.

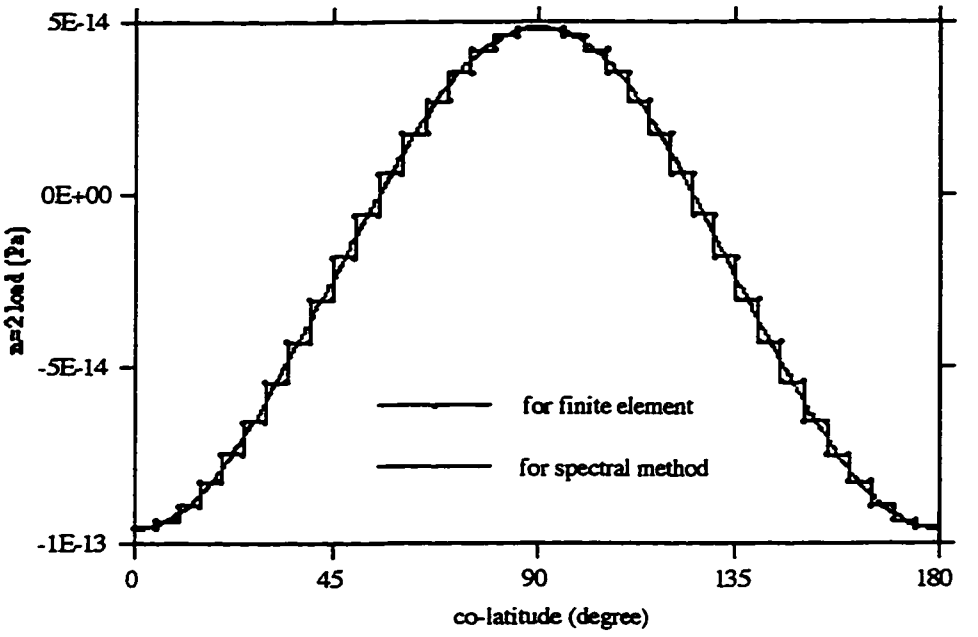

Figure 7.4 The discrete n=2 load for the finite element method vs. the continuous load for the spectrum method.

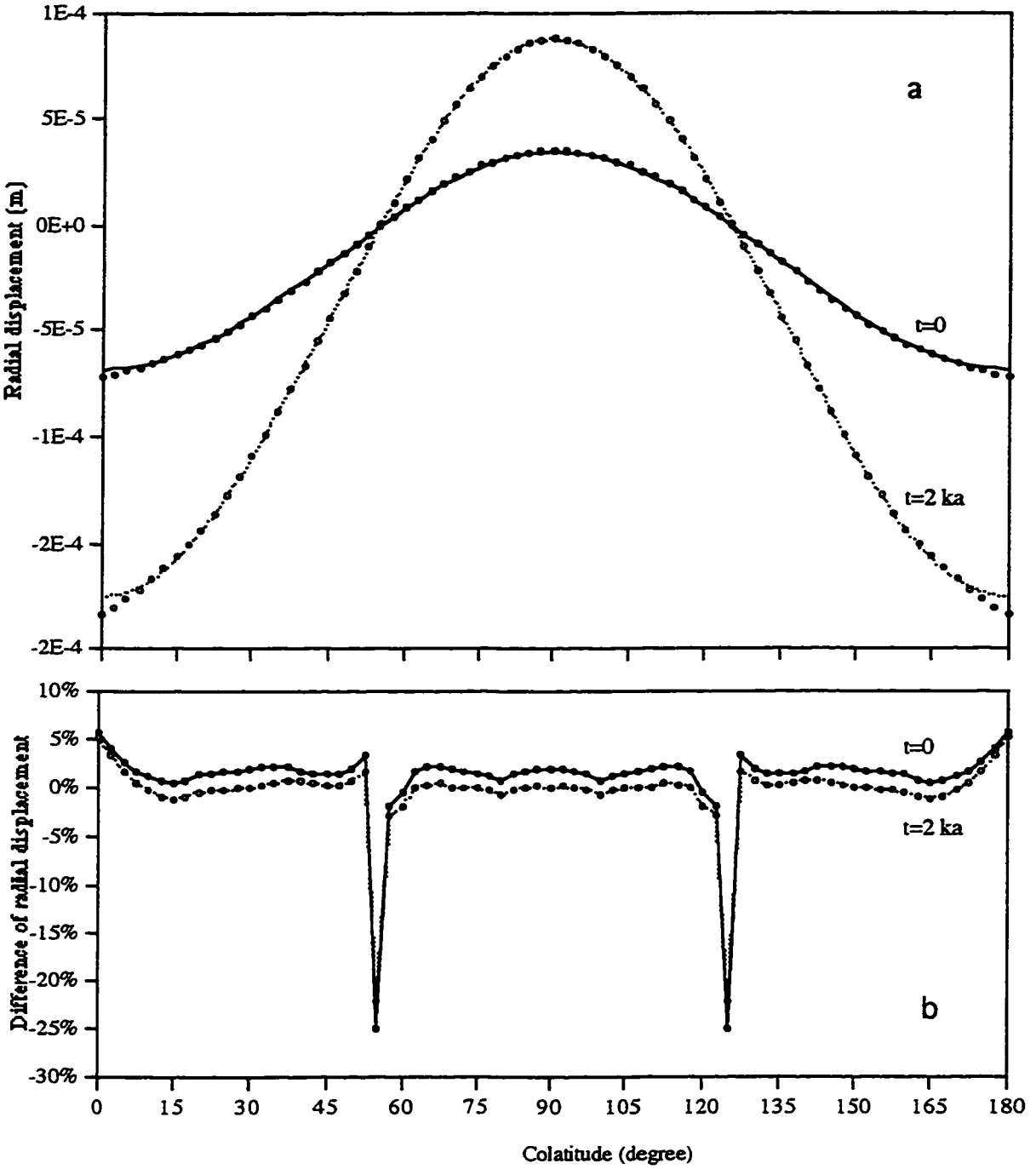

Figure 7.5 Comparison between radial displacements computed with the finite element method (circles in panel a) and the spectral method (lines in panel a) for a non-self gravitating and incompressible uniform spherical earth model under an n=2 load. The load history is a Heaviside loading event at t=0. Panel b displays difference of the displacements between the methods in percentage.

CHAPTER 8

CONCLUSIONS

While the main focus of this dissertation is on the effects of lateral heterogeneities on postglacial rebound, a by-product of this study is that new insight on the origin of the normal modes of viscoelastic-gravitational relaxation for a laterally homogeneous spherical earth is gained.

For laterally homogeneous spherical earth models, analytical solutions for simple incompressible earth models have been derived. Effects of self-gravitation, density contrast, viscosity contrast, and shear modulus contrast on postglacial rebound have been evaluated based on these analytical solutions. It is found that self-gravitation generally does not affect the number of normal modes. Neglecting self-gravitation results in slightly faster relaxation for loads with long wavelength (small n harmonics) but the difference approaches zero at large n.

The problem of singularities and false modes has been solved by the analytical derivation. A very simple way to avoid these artificial singularities has been suggested. Concerning the effects of the radial structure of the earth on postglacial rebound, our analytical solutions demonstrate that the maximum number of modes can be determined: A density contrast between two solid layers introduces a buoyancy mode and a contrast in the ratio of viscosity/(shear modulus) introduces two insignificant transitional modes. As for the interface between a solid mantle and an inviscid fluid core, there is only one extra buoyancy mode. It is confirmed that an elastic lithosphere introduces only one additional mode but it generally has very little strength of excitation. More significantly, the lithosphere causes a shortening of the relaxation time of the main mode at large n (also see McConnell, 1968).

In the study of lateral heterogeneities, two dimensional axisymmetric models have been extended to three dimensional non-axisymmetric models. The effects of lateral variation in lithospheric thickness, asthenospheric viscosity, and asthenospheric thickness have

been extended to other geodetic signatures other than relative sea levels. Also, the effect of lateral variation in density and deep mantle viscosity have been investigated. The followings are conclusions:

(1) The removal of axisymmetry does not significantly affect the validity of our 2D results. Further, the realistic modeling of postglacial rebound in North America confirms that simple earth models' results are consistent with the response of this more complex earth model to the realistic ice load history.

(2) The sensitivity of RVD to a lateral heterogeneity depends on the location of the observation site relative to the location of lateral heterogeneity and the load. When a change in model property takes place under the middle of the load, RVD in the central area is sensitive. Conversely, RVD around the edge is sensitive to a property change under the edge. Further, the effects are most prominent for the variation (of lithospheric thickness or asthenospheric viscosity) inside the former glaciated area.

(4) However, it is found that the vertical motion (measured by RVD and gravity) is least sensitive to earth properties in the inner peripheral area of the load whereas the horizontal motion is most sensitive there. The gravity (or vertical displacement) in the central area can be affected by low-viscosity asthenosphere outside the load area whereas the RVD is mainly affected by the rheology in an small area beneath an observation site.

(5) Further, no matter how sensitive RVD is at a site, RVD at the single site can not tell the existence of lateral heterogeneity because RVD at the site can also be sensitive to vertical rheological structure. Lateral heterogeneities can only be detected by comparing RSL at sites across a large area, i.e. spatial-temporal pattern of postglacial rebound.

(6) When comparing RVD of laterally homogeneous models with RSL observations to detect lateral heterogeneities, the inferred viscosity may not be exact but its spatial trend of variation is usually indicative, excluding the inner peripheral area. This comparative method works better where there is only lateral variation in lithospheric thickness.

(7) The effects on RSL are also dependent on the nature of the lateral heterogeneities and size of the ice sheet. In general, the effects of lateral variations in the asthenosphere are larger than that in the lithosphere. Furthermore, there is trade-off between effects of

asthenospheric viscosity and asthenospheric thickness which can not be uniquely resolved by RSL data.

(8) The effects of lateral viscosity variations in the lower mantle are significant for large ice loads with size comparable to the Laurentide Ice Sheet, but are small for small ice loads with size comparable to or smaller than the Fennoscandia Ice Sheet.

(9) For lateral density variations, a low density continental root generally has little effect on RSL and horizontal motions. However its effect on gravity is detectable given that the Pleistocene ice history is known.

The following are some suggestions for future studies on glacial isostatic adjustment:

1) Inversion of 3D rheological structure of the upper part of the mantle using RSL and other geophysical data. Right now there are only inversions done for the radial profile of viscosity in mantle (Mitrovica & Forte, 1997; Mitrovica & Peltier, 1995).

2) Develop a global geodynamic modeling software package that can solve both the equation of motion and Poisson's equation for a self-gravitating 3D heterogeneous spherical earth.

3) With more powerful supercomputers, the 3D spherical finite element grid can be improved to model glacial isostatic adjustment of realistic ice sheets and realistic earth models. Different kinds of observations besides RSL (e.g. gravity, horizontal displacement and velocities, earth rotation, etc.) can be computed and the earth model as well as ice history can be improved by comparing with the observations.

BIBLIOGRAPHY

Abaqus/Standard User's Manual, Hibbitt, Karlsson and Sorensen, Inc., Version 5.6, 1996. Pawtucket, RI, USA.

Amelung, F. & Wolf, D., 1994. Viscoelastic perturbations of the Earth: significance of the incremental gravitational force in models of glacial isostasy, *Geophys. J. Int.*, **117**, 864-879.

Anderson, D. L, 1989. *Theory of the Earth*, Blackwell Scientific Publications, Boston.

Barrell, J., 1914. The strength of the Earth's crust; Part VI relations of isostatic movements to a sphere of weakness. *J. Geol.* **22**, 655-683.

Breuer, D. & Wolf, D, 1995. Deglacial land emergence and lateral upper-mantle heterogeneity in the Svalbard Archipelago - I. First results for simple load models, *Geophys. J. Int.*, **121**, 775-788.

Cathles, L. M., 1975. *The Viscosity of the Earth's Mantle*. Princeton University Press, New Jersey.

Chinnery, M. A., 1975. The static deformation of an earth with a fluid core: a physical approach, *Geophys. J. R. astr. Soc.*, **42**, 461-475.

Clark, J. A., Farrell, W. E. & Peltier, W. R., 1978. Global changes in postglacial sea level: a numerical calculation, *Quat. Res.*, **9**, 265-287.

Crossley, D. J. & Gubbins, D., 1975. Static deformation of the Earth's liquid core, *Geophys. Res. Lett.*, **2**, 1-4.

D'Agostino, Gabriella, Spada, Giorgio, & Sabadini, R., 1997. Postglacial rebound and lateral viscosity variations: a semi-analytical approach based on a spherical model with Maxwell rheology, *Geophys. J. Int.*, **129**, F9-F13.

Dahlen, F. A. & Fels, S. B., 1978. A physical explanation of the static core paradox, *Geophys. J. R. astr. Soc.*, **55**, 317-332.

Dragoni, M., Yuen, D. A., Boschi, E., 1983. Global postseismic deformation in a stratified viscoelastic Earth: effects on Chandler wobble excitation, *J. Geophys. Res.*, **88**, 2240-2250.

Durek, J. J., Ritzwoller, M., & Woodhouse, J. H., 1993. Constraining upper mantle anelasticity using surface wave amplitude anomalies, *Geophys. J. Int.*, **114**, 249-272.

Dziewonski, A. M. & Anderson, D. L., 1981. Preliminary reference Earth model, *Phys. Earth Planet. Inter.*, **25**, 197-356.

Dziewonski, A. M., 1984. Mapping the lower mantle: determination of lateral heterogeneity in P velocity up to degree and order 6, *J. Geophys. Res.*, **89**, 5929-5952.

Ekman, Martin, Mäkinen, Jaakko, 1996. Recent Postglacial Rebound, Gravity Change and Mantle Flow in Fennoscandia, *Geophys. J. Int.*, **126**, 229-234.

Estey, L. H. and Douglas, B. J., 1986. Upper mantle anisotropy: A preliminary model, *J. Geophys. Res.*, **91**, 11,393-11406.

Fang, M. & Hager, B. H., 1995. The Singularity Mystery associated with a radially continuous Maxwell viscoelastic structure, *Geophys. J. Int.*, **123**, 849-865.

Farrell, W. E. & Clark, J. A., 1976. On postglacial sea level, *Geophys. J. R. astr. Soc.*, **46**, 647.

Farrell, W. E., 1972. Deformation of the Earth by surface loads, *Rev. Geophys. Space Phys.*, **10**, 761-797.

Fjeldskaar, W., 1994. Viscosity and thickness of the asthenosphere detected from the Fenno-scandian uplift, *Earth Plant. Sci. Lett.*, **126**, 399-410.

Gasperini, P. & Sabadini, R., 1989. Lateral heterogeneities in mantle viscosity and post-glacial rebound. *Geophys. J. Int.*, **98**, 413-428.

Gasperini, P. & Sabadini, R., 1990. Finite element modeling of lateral viscosity heterogeneities and post-glacial rebound, *Tectonophysics*, **179**, 141-149.

Gasperini, P., Sabadini, R., & Yuen, D. A., 1991. Deep continental roots: the effects of lateral variations of viscosity on post-glacial rebound, in *Glacial isostasy, Sea-Level, and Mantle Rheology*, eds. Sabadini, R., Lambeck, K., & Boschi, E., Kluwer Academic Publishers, Netherlands, 21-32.

Gasperini, P., Yuen, D. A., & Sabadini, R., 1990. Effects of lateral viscosity variations on postglacial rebound: implications for recent sea-level trends, *Geophys. Res. Lett.*, **17**, 5-8.

Han, D. & Wahr, J. M., 1989. The Post-Glacial Rebound Constraint on Deep Mantle Viscosity: A new Analysis for a Rotating Earth, in *Slow Deformation and Transmission of Stress in the Earth*, AGU Monograph Series, ed., Cohen, S. and Vanicek, P., 1-6.

Han, D. & Wahr, J. M., 1995. The viscoelastic relaxation of a realistically stratified earth, and a further analysis of postglacial rebound, *Geophys. J. Int.*, **120**, 287-311.

Han, D. & Wahr, J. M., 1997. An Analysis of Anisotropic Mantle Viscosity, and its Possible Effects on Post Glacial Rebound, *Phys. Earth and Planet. Int.*, **102**, 33-50.

Haskell, N. A., 1935. The motion of a viscous fluid under a surface load, *Physics* , **6**, 265-269.

James, T. S., 1991. Post-glacial deformation, Ph.D. thesis, Princeton Univ., Princeton, N.J.

Jiang, X. & Peltier, W. R., 1994. The procession constant of the Earth: Variations through the ice-age, *Geophys. Res. Lett.* **21**, 2299-2302.

Karato, S., & Wu, P., 1993. Rheology of the Upper Mantle: A Synthesis, *Science*, **260**, 771-778.

Kaufmann, G. & Wolf, D., 1996. Deglacial land emergence and lateral upper-mantle heterogeneity in the Svalbard Archipelago - II. Extended results for high-resolution load models, *Geophys. J. Int.*, **127**, 125-140.

Kaufmann, G., Wu, P., & Wolf, D., 1997. Some effects of lateral heterogeneities in the upper mantle on postglacial land uplift close to continental margins, *Geophys. J. Int.*, **128**, 175-187.

Li, X. D. & Romanowicz, B., 1996. Global Mantle Shear-Velocity Model Developed Using Nonlinear Asymptotic Coupling Theory, *J. Geophys. Res.*, **101**, 22,245-22,272.

Longman, I. M., 1963. A Green's function for determining the deformation of the earth under surface mass loads, 2, Computations and numerical results, *J. Geophys. Res.*, 68, 485.

Love, A. E. H., 1911. *Some Problems of Geodynamics*, Dover, New York.

McConnell, R. K., 1968. Viscosity of the mantle from relaxation time spectra of isostatic adjustment, *J. Geophys. Res.*, **73**,7089-7105.

Minster, J. B. & Anderson, D. L., 1981. A model of dislocation-controlled rheology for the mantle, *Phil. Trans. R. Soc. London*, **A299**, 319-356.

Mitrovica, J .X. & Peltier, W. R., 1993. The inference of mantle viscosity from an inversion of the Fennoscandian relaxation spectrum, *Geophys. J. Int.*, **114**,45-62.

Mitrovica, J. X. & Davis, J. L., 1995. Present-day post-glacial sea level change far from the Late Pleistocene ice sheets: Implications for recent analyses of tide gauge records, *Geophys. Res. Lett.* **22**, 2529-2532.

Mitrovica, J. X. & Forte, A. M., 1995. Pleistocene glaciation and the Earth's precession constant, *Geophys. J. Int.*, **121**, 21-32.

Mitrovica, J. X. & Forte, A. M., 1997. Radial profile of mantle viscosity: Results from the joint inversion of convection and postglacial rebound observables, *J. Geophys. Res.*, **102**, 2751-2769.

Mitrovica, J. X. & Forte, A. M., Pan, R., 1997. Glaciation-induced variations in the Earth's precession frequency, obliquity and insolation over the last 2.6 Ma, *Geophys. J. Int.*, **128**, 270-284.

Mitrovica, J. X. & Peltier, W. R., 1989. Pleistocene Deglaciation and the Global Gravity Field, *J. Geophys. Res.*, **94**, 13651-13671.

Mitrovica, J. X. & Peltier, W. R., 1991. On postglacial geoid subsidence over the equatorial oceans, *J. Geophys. Res.*, **96**, 20,053-20,071.

Mitrovica, J. X. & Peltier, W. R., 1995. Constraints on mantle viscosity based upon the inversion of post-glacial uplift data from the Hudson Bay region, *Geophys. J. Int.*, **122**, 353-377.

Mitrovica, J. X., 1996. Haskell [1935] revisited, *J. Geophys. Res.*, **101**, 555-569.

Mitrovica, J. X., Davis, J. L., & Shapiro, I. I., 1993. Constraining Proposed Combinations of Ice History and Earth Rheology using VLBI-Determined Baseline Length Rates in North America, *Geophys. Res. Lett.*, **20**, 2387-2390.

Montagner, J. P. & Tanimoto, T., 1990. Global anisotropy in the upper mantle inferred from the regionalization of the phase velocities, *J. Geophys. Res.*, **95**, 4797-4819.

Montagner, J. P. & Tanimoto, T., 1991. Global upper mantle tomography of seismic velocities and anisotropies, *J. Geophys. Res.*, **96**, 20,337-20,351.

Nakada, M. & Lambeck, K., 1989. Late Pleistocene and Holocene sea-level changes in the Australian region and mantle rheology, *Geophys. J. Int.*, **96**, 497-517.

Nakada, M., 1983. Rheological structure of the earth's mantle derived from glacial rebound in Laurentide, *J. Phys. Earth*, **31**, 349-386.

Nataf, H. C., Nakanishi, I., & Anderson, D. L., 1986. Measurements of mantle wave velocities and inversion for lateral heterogeneities and anisotropy, III, Inversion, *J. Geophys. Res.*, **91**, 7261-7307.

Newman, W. S., Cinquemani, L. J., Pardi, R. R. & Marcus, L. F., 1980. Holocene delevelling of the United States' east coast, in *Earth Rheology, Isostasy and Eustasy*, ed. Morner, N., Wiley, New York.

O'Connell, R. J., 1971. Pleistocene glaciation and the viscosity of the lower mantle, *Geophys. J.*, **23**, 299-327.

Oxburgh, E. R., 1980. Mantle Mineralogy and Dynamics, in *Physics of the Earth's Interior*, eds. Dziewonski, A. M. & Boschi, E., North-Holland Publishing Company, New York.

Paterson, W. S. B., 1972. Laurentide ice sheet: estimated volumes during late Wisconsin, *Rev. Geophys. Space Phys.*, **10**, 885-917.

Paterson, W. S. B., 1981. *The Physics of Glaciers, 2nd edition*, Pergamon Press, New York.

Peltier, W. R. & Andrews, J. T., 1976. Glacial-Isostatic Adjustment - I. the forward problem, *Geophys. J. R. astr. Soc.*, **46**, 605-646.

Peltier, W. R. & Tushingham, A. M., 1989. Global sea level rise and the Greenhouse Effect: Might they be connected? *Science*, **244**, 806-810.

Peltier, W. R. & Tushingham, A. M., 1991. Influence of glacial isostatic adjustment on tide gauge measurements of secular see level change, *J. Geophys. Res.*, **96**, 6779-6796.

Peltier, W. R. & Wu, P., 1982. Mantle phase transitions and the free air gravity anomalies over Fennoscandia and Laurentia, *Geophys. Res. Lett.*, **9**, 731-734.

Peltier, W. R. & Wu, P., 1983. Continental Lithospheric thickness and deglaciation induced true polar wander, *Geophys. Res. Lett.*, **10**, 181-184.

Peltier, W. R., 1974. The impulse response of a Maxwell earth, *Rev. Geophys. and Space Phys.*, **12**, 649-669.

Peltier, W. R., 1976. Glacial isostatic adjustment - II: the inverse problem, *Geophys. J. R. astr. Soc.*, **46**, 669-705.

Peltier, W. R., 1982. Dynamics of the Ice Age Earth, *Advance in Geophysics*, **24**, 1-146.

Peltier, W. R., 1984. The thickness of the continental lithosphere, *J. Geophys. Res.*, **89**, 11,303-11,316.

Peltier, W. R., 1985. The LAGEOS constraint on deep mantle viscosity: Results from a new normal mode method for the inversion of viscoelastic relaxation spectra, *J. Geophys. Res.*, **90**, 9411-9421.

Peltier, W. R., 1986. Deglaciation-Induced Vertical Motion of the North American Continent and Transient Lower Mantle Rheology, *J. Geophys. Res.*, **91**, 9099-9123.

Peltier, W. R., 1988. Global sea level and Earth rotation, *Science*, **240**, 895-901.

Peltier, W. R., 1994. Ice Age Paleotopography. *Science*, **265**, 195-201.

Peltier, W. R., Drummond, R. A. and Tushingham, A. M., 1986. Post-glacial rebound and transient lower mantle rheology, *Geophys. J. R. astr. Soc.*, **87**, 79-116.

Peltier, W. R., Farrell, W. E. & Clark, J. A., 1978. Glacial isostasy and relative sea level: a global finite element model, *Tectonophys.*, **50**, 81-110.

Peltier, W. R., Yuen, D. A. & Wu, P., 1980. Postglacial rebound and transient rheology, *Geophys. Res. Lett.*, **7**, 733-736.

Pirazzoli, P. A., 1991. *World atlas of Holocene sea-level changes*, Elsevier, New York.

Poirier, J. P., 1985. *Creep of crystals*, Cambridge University Press, Cambridge.

Post, R., & Griggs, D., 1973. The earth's mantle: evidence of non-Newtonian flow, *Science*, **181**, 1242-1244.

Ranalli, G., & Fischer, B., 1984. Diffusion creep, dislocation creep, and mantel rheology, *Phys. Earth Planet Inter.*, **34**, 77-84.

Ranalli, G., 1987. *Rheology of the Earth*, Allen & Unwin, London.

Ricard, Y., Sabadini, R. & Spada, G., 1992. Isostatic deformations and polar wander induced by redistribution of mass within the Earth, *J. Geophys. Res.*, **97**, 14,223-14236.

Richards, M. A. & Hager, B. H., 1989. Effects of lateral viscosity variations on long-wavelength geoid anomalies and topography, *J. Geophys. Res.*, **94**, 10,299-10,313.

Romanowicz, B., 1990. The upper mantle degree 2: Constraints and inferences on attenuation tomography from global mantle wave measurements, *J. Geophys. Res.*, **95**, 11,051-11,071.

Roult, G., Romanowicz, B., and Montagner J. P., 1990. 3D upper mantle shear velocity and attenuation from fundamental mode free oscillation data, *Geophys. J. Int.*, **101**, 61-80.

Rümpker, G. & Wolf, D., 1996. Viscoelastic relaxation of a Burgers half-space: implications for the interpretation of the Fennoscandian uplift, *Geophys. J. Int.*, **124**, 541-555.

Sabadini, R. & Peltier, W. R., 1981. Pleistocene deglaciation and the Earth's rotation: Implications for mantle viscosity, *Geophys. J. R. astr. Soc.*, **66**, 553-578.

Sabadini, R., Yuen, D. A. & Portney,. M., 1986. The effects of upper-mantle lateral heterogeneities on postglacial rebound, *Geophys. Res. Lett.*, **13**, 337-340.

Sabadini, R., Yuen, D. A., Boschi, E., 1982. Polar Wandering and the Forced Responses of a Rotating, Multilayered, Viscoelastic Planet, *J. Geophys. Res.*, **87**, 2885-2903.

Sabadini, R., Yuen, D. A., Gasperini, P., 1985. The effects of transient rheology on the interpretation of lower mantle viscosity, *Geophys. Res. Lett.*, **12**, 361-364.

Smylie, D. E. & Mansinha, L., 1971. The elasticity theory of dislocations in real earth models and changes in the rotation of the Earth, *Geophys. J. R. astr. Soc.*, **23**, 329-354.

Spada, Giorgio, Yuen, D. A., Sabadini, R., Morin, Paul J., and Gasperini, P., 1990. A computer-aided, algebraic approach to the post-glacial rebound problem, *The mathematica Journal*, **1**, 65-69.

Su, W. J. and Dziewonski, A. M., 1991. Predominance of long-wavelength heterogeneity in the mantle, *Nature*, **352**, 121-126.

Su, W. J. and Dziewonski, A. M., 1992. On the scale of mantle heterogeneity, *Phys. Earth Planet. Inter.*, **74**, 29-54..

Su, W. J., Woodward, R. L., & Dziewonski, A. M., 1992. Deep origin of mid-ocean-ridge seismic velocity anomalies, *Nature*, **360**, 149-152.

Su, W. J., Woodward, R. L., & Dziewonski, A. M., 1994. Degree 12 model of shear velocity heterogeneity in the mantle, *J. Geophys. Res.*, **99**, 6945-6980.

Tanimoto, T., 1986a. The Backus-Gilbert approach to the 3-D structure in the upper mantle, I, Lateral variation of surface wave phase velocity with its error and resolution, *Geophys. J. R. astr. Soc.*, **82**, 105-123.

Tanimoto, T., 1986b. The Backus-Gilbert approach to the 3-D structure in the upper mantle, II, SH and SV velocity, *Geophys. J. R. astr. Soc.*, **84**, 49-69.

Tanimoto, T., 1990a. Long wavelength S-wave velocity structure throughout the mantel, *Geophys. J. Int.*, **100**, 327-336.

Tanimoto, T., 1990b. Predominance of large-scale heterogeneity and the shift of velocity anomalies between the upper and lower mantle, *J. Phys. Earth*, **38**, 493-509.

Tralli, D. M. & Ita, Joel J., 1994. Regionalized variations in upper mantle temperature, SEDI 94, S8 Global Seismology and Large Scale Dynamics, Whistler Mountain, British Columbia, Canada, Aug. 7-12, 1994.

Trupin, A. S. and Wahr, J. M., 1991. Constraints on Long-Period Sea Level Variations from Global Tide Gauge Data, in *Glacial isostasy, Sea-Level, and Mantle Rheology*, eds. Sabadini, R., Lambeck, K., & Boschi, E., Kluwer Academic Publishers, Netherlands, 271-284.

Trupin, A. S., 1993. Effect of polar ice on the Earth's rotation and gravitational potential, *Geophys. J. Int.*, **113**, 273-283.

Trupin, A. S., Meier, M. F. & Wahr, J. M., 1992. The Effect of Melting Glaciers on the Earth's Rotation and Gravitational Field: 1965-1984, *Geophys J. Int.*, **108**, 1-15.

Turcotte, D. L. & Schubert, G., 1982. *Geodynamics: Applications of Continuum Physics to Geological Problems*, John Wiley & Sons, Toronto.

Tushingham, A. M. & Peltier, W. R., 1991. ICE-3G: A new global model of late Pleistocene deglaciation based upon geophysical predictions of postglacial relative sea level change, *J. Geophys. Res.*, **96**, 4497-4523.

Van Bemmelen, R. W. & Berlage, H. P., 1935. Versuch einer mathematischen Behandlung geotektonischer Bewegung unter besonderer Berucksichtegung der Undationstheorie, *Gerland Beitr Geophys.*, **43**, 19-55.

Wahr, J. M., Han, D. & Trupin, A., 1995. Predictions of Vertical Uplift Caused by Changing Polar Ice Volumes on a Visco-Elastic Earth, *Geophys. Res. Lett.*, **22**, 977-980.

Wahr, J. M., Han, D., Trupin, A. & Lindqvist, V., 1993. Secular Changes in Gravity and Rotation: Evidence of post glacial rebound or changes in polar ice? *Advances in Space Research*, **13**, 11,257-11,269.

Walcott, R. I., 1970a. Flexural rigidity, thickness and viscosity of the lithosphere, *J. Geophys. Res.*, **75**, 3941.

Walcott, R. I., 1970b. Flexure of the lithosphere at Hawaii, *Tectonophysics*, **9**, 435.

Wolf, D., 1984. The relaxation of spherical and flat Maxwell Earth models and effects due to the presence of the lithosphere, *J. Geophys.*, **56**, 24-33.

Wolf, D., 1987. An upper bound on lithosphere thickness from glacio-isostatic adjustment in Fennoscandia, *J. Geophys.*, **61**, 141-149.

Wong, Y. K., 1989. Upper mantle heterogeneity from phase and amplitude data of mantle waves, Ph.D. thesis, Harvard Univ., Cambridge, Mass.

Woodhouse, J. H. & Dziewonski, A. M., 1984. Mapping the upper mantle: three-dimensional modeling of Earth structure by inversion of seismic waveforms, *J. Geophys. Res.*, **89**, 5953-5986.

Woodward, R. & Masters, G., 1991a. Global upper mantle structure from long period differential travel times, *J. Geophys. Res.*, **96**, 6351-6377.

Woodward, R. & Masters, G., 1991b. Lower-mantle structure from long period differential travel times, *Nature*, **352**, 231-233.

Wu, P. & Hasegawa, H. S., 1996a. Induced stresses and fault potential in Eastern Canada due to a disc load: a preliminary analysis, *Geophys. J. Int.*, **125**, 415-430.

Wu, P. & Hasegawa, H. S., 1996b. Induced stresses and fault potential in Eastern Canada due to a realistic load: a preliminary analysis, *Geophys. J. Int.*, **127**, 215-229.

Wu, P. & Johnston, P., 1998. Validity of using flat-earth finite element models in the study of postglacial rebound, in *Dynamics of the Ice Age Earth: a modern perspective*, ed. Wu, P.

Wu, P. & Ni, Z., 1996. Some Analytical Solutions for the Visco-elastic Gravitational Relaxation of a Two-Layer Non-Self-Gravitating Incompressible Spherical Earth, *Geophys. J. Int.*, **126**, 413-436.

Wu, P. & Peltier, W. R., 1982. Viscous gravitational relaxation, *Geophys. J. R. astr. Soc.*, **70**, 434-486.

Wu, P. & Peltier, W. R.,1983. Glacial isostatic adjustment and the free air gravity anomaly as a constraint on deep mantle viscosity, *Geophys. J. R. astr. Soc.*, **74**, 377-450.

Wu, P. & Peltier, W. R.,1984. Pleistocene deglaciation and the Earth's rotation: a new analysis, *Geophys. J. R. astr. Soc.*, **76**, 753-792.

Wu, P., 1978. The response of a Maxwell earth to applied surface mass loads: Glacial Isostatic Adjustment, MSc Thesis, University of Toronto.

Wu, P., 1990. Deformation of internal boundaries in a viscoelastic earth and topographic coupling between the mantle and core, *Geophys. J. Int.*, **101**, 213-231.

Wu, P., 1992a. Deformation of an incompressible viscoelastic flat earth with power law creep: a finite element approach, *Geophys. J. Int.*, **108**, 35-51.

Wu, P., 1992b. Viscoelastic vs. Viscous deformation and the advection of prestress, *Geophys. J. Int.*, **108**, 35-51.

Wu, P., 1993. Postglacial rebound in a power-law medium with axial symmetry and the existence of the transition zone in relative sea-level data, *Geophys. J. Int.*, **114**, 417-432.

Wu, P., 1995. Can observations of postglacial rebound tell whether the rheology of the mantle is linear or nonlinear? *Geophys. Res. Lett.*, **22**, 1645-1648.

Wu, P., 1997. Effect of viscosity structure of fault potential and stress orientations in eastern Canada, *Geophys. J. Int.*, **130**, 365-382.

Wu, P., Ni, Z., & Kaufmann, G., 1998. Postglacial rebound with lateral heterogeneities: from 2D to 3D modeling, in *Dynamics of the Ice Age Earth: a modern perspective*, ed. Wu, P.

Yuen, D. A., Sabadini, R. C. A., Gasperini, P., & Boschi, E., 1986. On transient rheology and glacial isostasy, *J. Geophys. Res.*, **91**, 11420-11438.

Zhang, Y. & Tanimoto, T., 1993. High-resolution global upper mantle structure, plate tectonics, *J. Geophys. Res.*, **98**, 9793-9823.

Zienkiewicz, O. C. & Taylor, R. L., 1989. *The finite element method*, Fourth Edition, V. 1 and 2, McGraw-Hill Book Company, London.

APPENDIX A. ANALYTICAL EXPRESSIONS FOR THE LOVE NUMBERS $h_n(s)$ AND $l_n(s)$ FOR A 2-LAYER INCOMPRESSIBLE, NON-SELF-GRAVITATING SPHERICAL EARTH

The solution in the transformed domain, which has been derived with the THEORIST symbolic manipulation software, can be expressed in terms of the transform variable s:

$$h_n(s) = \frac{1}{3}\,\frac{g_0\,(\nu\, s+\mu)\,(CUA\, s^3 + CUB\, s^2 + CUC\, s - CUD)}{(CDA\, s^4 + CDB\, s^3 + CDC\, s^2 + CDD\, s + CDE)}$$

$$l_n(s) = \frac{2}{3}\,\frac{g_0\,(\nu\, s+\mu)\,(CVA\, s^3 + CVB\, s^2 + CVC\, s + CVD)}{a^4\,\mu\,\nu\, n\,(n+1)\,(CDA\, s^4 + CDB\, s^3 + CDC\, s^2 + CDD\, s + CDE)}$$

where the variables CUA, CUB, CUC, CUD appear in the numerator of $h_n(s)$; CVA, CVB, CVC, CVD appear in the numerator of $l_n(s)$ and CDA, CDB, CDC, CDD, CDE appear in the denominators of $h_n(s)$ and $l_n(s)$. They are defined by:

$$CUA = -2\,\nu\,\nu_c^2\left(\frac{TC\,\mu + TF\,\mu_c}{n+1} + n\,(2n+1)\,TAA\,d\rho\,g_c\right)$$
$$- TGA\left[2\,(n-1)\,(2n^2+4n+3)\,\frac{\mu_c}{c} + n\,(2n+1)\,d\rho\,g_c\right]\frac{\mu_c}{\mu}\nu\,\nu_c^2$$

$$CUB = -2\,\nu_c\left[\frac{TF\,(\mu_c\,\nu + \mu\,\nu_c)\,\mu_c}{n+1} + 2\,\frac{TC\,\mu\,\mu_c\,\nu}{n+1} + n\,(2n+1)\,TAA\,(2\,\mu_c\,\nu + \mu\,\nu_c)\,d\rho\,g_c\right]$$
$$- \frac{2\,TGA\,\nu_c^2\,\mu_c}{c}\left\{2\,(n-1)\,(2n^2+4n+3)\,\mu_c + n\,(2n+1)\,c\,d\rho\,g_c\right\}$$
$$- n\,(2n+1)\,TGA\,\nu_c\,\mu_c^2\,\nu\,d\rho\,g_c / \mu$$

$$CUC = -\frac{2\,(TC\,\nu + TF\,\nu_c)\,\mu\,\mu_c^2}{n+1}$$
$$- 2\,n\,(2n+1)\,(TAA\,\mu_c\,\nu + 2\,TAA\,\mu\,\nu_c + TGA\,\mu_c\,\nu_c)\,\mu_c\,d\rho\,g_c$$

$$- \frac{TGA\ \mu\ \mu_c\ \nu_c^2}{c\ \nu} [2\ (n - 1)\ (2\ n^2 + 4n + 3)\ \mu_c + n\ (2\ n + 1)\ c\ d\rho\ g_c]$$

$$CUD = \frac{n\ (2\ n + 1)\ (2TAA\ \nu + TGA\ \nu_d)\ \mu\ \mu_c^2\ d\rho\ g_c}{\nu}$$

$$CDA = 2\ \frac{(ZA\ \mu + ZB\ \mu_d)\ \nu^2\ \nu_c^2}{(n + 1)\ (2\ n + 1)}$$

$$+ 4\ \frac{(n - 1)\ [n\ (n + 2)\ TD\ \mu^2 + TI\ \mu_c^2 + TH\ \mu\ \mu_c]\ \nu^2\ \nu_c^2}{(n + 1)\ 2\ n + 1^2\ n}$$

$$+ \frac{TGA\ [2\ (n - 1)\ (2\ n^2 + 4\ n + 3)\ \mu_c + n\ (2\ n + 1)\ c\ d\rho\ g_c]\ \rho\ \mu_c\ \nu^2\ \nu_c^2\ g_0}{(2\ n + 1)\ c\ \mu}$$

$$+ 2\ TAA\ n\ \rho\ \nu^2\ \nu_c^2\ d\rho\ g_0\ g_c$$

$$CDB = 2\ \frac{ZA\ (2\ \mu_c\ \nu + \mu\ \nu_d)\ \mu + ZB\ (\mu_c\ \nu + 2\ \mu\ \nu_d)\ \mu_c\ \nu\ \nu_c}{(n + 1)\ (2\ n + 1)}$$

$$+ 4\ \frac{(n - 1)\ (2\ [\{n + 2\}\ TD\ n\ \mu\ \nu + TI\ \mu_c\ \nu_d] + TH\ [\mu_c\ \nu + \mu\ \nu_d])\ \mu\ \mu_c\ \nu\ \nu_c}{n\ (n + 1)\ (2\ n + 1)^2}$$

$$+ \frac{TGA\ \{6\ (n - 1)\ (2\ n^2 + 4n + 3)\ \mu\ \mu_c\ \nu_c + n\ (2\ n + 1)\ (\mu_c\ \nu + 3\ \mu\ \nu_d)\ c\ d\rho\ g_c\}\ \rho\ \mu_c\ \nu\ \nu_c\ g_0}{(2\ n + 1)\ c\ \mu}$$

$$+ 4\ TAA\ n\ (\mu_c\ \nu + \mu\ \nu_d)\ \rho\ \nu\ \nu_c\ d\rho\ g_0\ g_c$$

$$CDC = 2\ \frac{ZA\ (\mu_c\ \nu + 2\ \mu\ \nu_d)\ \mu\ \mu_c\ \nu + ZB\ (2\ \mu_c\ \nu + \mu\ \nu_d)\ \mu\ \mu_c\ \nu_c}{(n + 1)\ (2\ n + 1)}$$

$$+ 4\ \frac{[n - 1]\ [(n + 2)\ TD\ n\ \nu^2 + TI\ \nu_c^2 + TH\ \nu\ \nu_d]\ \mu^2\ \mu_c^2}{n\ (n + 1)\ (2\ n + 1)^2}$$

$$+ 6\ \frac{(n - 1)\ (2\ n^2 + 4\ n + 3)\ TGA\ \rho\ \mu\ \mu_c^2\ \nu_c^2\ g_0}{(2\ n + 1)\ c}$$

$$+ n\ [2\ TAA\ (\mu_c^2\ \nu^2 + \mu^2\ \nu_c^2 + 4\ \mu\ \mu_c\ \nu\ \nu_d) + 3\ TGA\ (\mu_c\ \nu + \mu\ \nu_d)\ \mu_c\ \nu_d]\ \rho\ d\rho\ g_0\ g_c$$

$$CDD = 2\ \frac{(ZA\ \nu + ZB\ \nu_d)\ \mu^2\ \mu_c^2}{(n + 1)\ (2\ n + 1)}$$

$$+ \frac{TGA\ [2\ (n - 1)\ (2\ n^2 + 4\ n + 3)\ \mu_c + n\ (2\ n + 1)\ c\ d\rho\ g_c]\ \rho\ \mu^2\ \mu_c\ \nu_c^2\ g_0}{(2\ n + 1)\ c\ \nu}$$

$$+ 4\ TAA\ n\ (\mu_c\ \nu + \mu\ \nu_d)\ \rho\ \mu\ \mu_c\ d\rho\ g_0\ g_c + 3\ TGA\ n\ \rho\ \mu\ \mu_c^2\ \nu_c\ d\rho\ g_0\ g_c$$

$$CDE = \frac{n\ (2\ TAA\ \nu + TGA\ \nu_d)\ d\rho\ g_0\ g_c\ \rho\ \mu^2\ \mu_c^2}{\nu}$$

$$CVA = 2\,VD\,a^4 n\,\mu^2 \nu^2 \nu_c^2$$
$$+ (n-1)(2n+3)(2n-1)[3\,VB\,\mu + n(n+1)(2n^2+4n+3)\,VC\,\mu_c]\,a^4 \mu_c \nu^2 \nu_c^2$$
$$+ n[VE\,\mu + (n+1)(2n+3)(2n-1)\,VA\,a^4 \mu_c]\,\nu^2 \nu_c^2\,d\rho\,g_c$$

$$CVB = 4\,VD\,a^4 n\,\mu^2 \mu_c \nu^2 \nu_c$$
$$+ 2n(n+1)(n-1)(2n+3)(2n-1)(2n^2+4n+3)\,VC\,a^4 \mu\,\mu_c^2 \nu\,\nu_c^2$$
$$+ 3(n-1)(2n+3)(2n-1)\,VB\,a^4(\mu_c \nu + \mu \nu_c)\,\mu\,\mu_c \nu \nu_c$$
$$+ VE\,n(2\mu_c \nu + \mu \nu_c)\,\mu \nu \nu_c\,d\rho\,g_c$$
$$+ n(n+1)(2n+3)(2n-1)\,VA\,a^4(\mu_c \nu + 2\mu \nu_c)\,\mu_c \nu \nu_c\,d\rho\,g_c$$

$$CVC = 2\,VD\,a^4 n\,\mu^2 \mu_c^2 \nu^2$$
$$+ (n-1)(2n+3)(2n-1)\,a^4[3\,VB\,\nu + n(n+1)(2n^2+4n+3)\,VC\,\nu_c]\,\mu^2 \mu_c^2 \nu_c$$
$$+ VE\,n(\mu_c \nu + 2\mu \nu_c)\,\mu\,\mu_c \nu\,d\rho\,g_c$$
$$+ n(n+1)(2n+3)(2n-1)\,VA\,a^4(2\mu_c \nu + \mu \nu_c)\,\mu\,\mu_c \nu_c\,d\rho\,g_c$$

$$CVD = n[VE\,\nu + (n+1)(2n+3)(2n-1)\,VA\,a^4 \nu_c]\,\mu^2 \mu_c^2\,d\rho\,g_c$$

$$ZA = TBA\,g_c\,d\rho + TC\,g_0\,\rho$$

$$ZB = TEA\,g_c\,d\rho + TF\,g_0\,\rho$$

and the variables TC, TD, TF, TH, TI, TAA, TBA, TEA, TGA, VA, VB, VC, VD, VE are only functions of the radius of the earth (a), the radius of the interface (c) and angular order (n):

$$TC = 2\,\frac{(n^4+2n^3-n^2-2n+3)(2n+1)\,c^{2n+3}}{a^4}$$
$$+ 2(n+1)(n-1)(2n^2+4n+3)\,a^{-2n-3}\,c^{4n+2}$$
$$- 2n(n+2)(2n^2+1)\,a^{2n-1}$$
$$- 2n(n+2)(n+1)(n-1)(2n+1)\,c^{2n-1}$$

$$TD = 2\,\frac{(c^{2n+3}+a^4 c^{2n-1})(n^4+2n^3-n^2-2n+3)(2n+1)^2}{a^5}$$
$$- 4\,\frac{n(n+2)(n+1)(n-1)(2n+3)(2n-1)\,c^{2n+1}}{a^3}$$
$$- 2(a^{2n-2}+a^{-2n-4}\,c^{4n+2})(2n^2+1)(2n^2+4n+3)$$

$$TF = 3\,\frac{(n^2-3)(2n+1)\,c^{2n+3}}{a^4} - (8n^4+16n^3+4n^2-4n+3)\,a^{2n-1}$$
$$- 4(n+1)(n-1)(2n^2+4n+3)\,a^{-2n-3}\,c^{4n+2}$$

$$- 3\,(n+1)\,(n-1)\,(2n+1)\,c^{2n-1}$$

$$TH = 3\,\frac{(n^4+2n^3-n^2-2n+3)\,2n+1^2\,c^{2n-1}}{a} + 3\,\frac{n\,(n+2)\,(n^2-3)\,2n+1^2\,c^{2n+3}}{a^5}$$

$$- 6\,\frac{n\,(n+2)\,(n+1)\,(n-1)\,(2n+3)\,(2n-1)\,c^{2n+1}}{a^3}$$

$$- (8n^4+16n^3+4n^2-4n+3)\,(2n^2+4n+3)\,a^{2n-2}$$
$$+ 4n\,(n+2)\,(2n^2+1)\,(2n^2+4n+3)\,a^{-2n-4}c^{4n+2}$$

$$TI = -\frac{\{(n^4+2n^3-n^2-2n+3)a^4c^{2n-1}+n(n+2)(n+1)(n-1)c^{2n+3}\}(2n+1)^2(2n^2+4n+3)}{a^5}$$

$$+ 2\,\frac{n\,(n+2)\,(n+1)\,(n-1)\,(2n+3)\,(4n^3+6n^2+2n-3)\,c^{2n+1}}{a^3}$$

$$- 2\,(n+1)\,(n-1)\,(2n^2+4n+3)^2\,a^{2n-2}$$
$$- 2n\,(n+2)\,(2n^2+1)\,(2n^2+4n+3)\,a^{-2n-4}c^{4n+2}$$

$$TAA = \frac{c^{2n+4}}{a^4} - c\,a^{2n-1} - c^{4n+3}a^{-2n-3} + c^{2n}$$

$$TBA = -\frac{(n^4+2n^3-n^2-2n+3)\,(2n+1)\,c^{2n}}{a}$$

$$+ \frac{n\,(n+2)\,(n+1)\,(n-1)\,(2n+1)\,c^{2n+4}}{a^5}$$

$$- (n+1)\,(n-1)\,(2n^2+4n+3)\,a^{2n-2}c$$
$$+ n\,(n+2)\,(2n^2+1)\,a^{-2n-4}c^{4n+3}$$

$$TEA = -\frac{(n^4+2n^3-n^2-2n+3)\,(2n+1)^2c^{2n}}{a}$$

$$+ \frac{\{2\,(2n+3)\,(2n-1)\,a^2\,c^{2n+2} - (2n+1)^2\,c^{2n+4}\}\,(n+2)\,(n+1)\,(n-1)\,n}{a^5}$$

$$- 2\,(n+1)\,(n-1)\,(2n^2+4n+3)\,a^{2n-2}c$$
$$- 2n\,(n+2)\,(2n^2+1)\,a^{-2n-4}c^{4n+3}$$

$$TGA = -\frac{(2n+1)\,c^{2n+4}}{a^4} + 2\,a^{-2n-3}c^{4n+3} + (2n+1)\,c^{2n} - 2\,a^{2n-1}c$$

$$VA = 3\,\frac{a^{2n-1}\,c}{(2n+3)\,(2n-1)} - \frac{1}{2}\,\frac{(2n^2+2n-1)\,c^{2n+2}}{(n+1)\,a^2}$$

$$+\frac{1}{2}\frac{(n^2+n-3)(2n+1)^2c^{2n}}{(n+1)(2n+3)(2n-1)}-3\frac{na^{-2n-3}c^{4n+3}}{(n+1)(2n+3)(2n-1)}$$
$$+\frac{1}{2}\frac{n(2n+1)^2c^{2n+4}}{(2n+3)(2n-1)a^4}$$

$$VB=\frac{(8n^4+16n^3+4n^2-4n+3)a^{2n-1}}{(n-1)(2n+3)(2n+1)(2n-1)}+\frac{(2n^2+2n-1)c^{2n+1}}{(2n+1)a^2}$$
$$-\frac{(n^2+n-3)(2n+1)c^{2n-1}}{(2n+3)(2n-1)}+4\frac{n(2n^2+4n+3)a^{-2n-3}c^{4n+2}}{(2n+3)(2n+1)(2n-1)}$$
$$-\frac{n(n^2-3)(2n+1)c^{2n+3}}{(n-1)(2n+3)(2n-1)a^4}$$

$$VC=6\frac{(n+1)a^{2n-1}-na^{-2n-3}c^{4n+2}}{n(n+1)(2n+3)(2n+1)(2n-1)}+\frac{(2n+1)c^{2n+3}}{(2n+3)(2n-1)a^4}$$
$$-\frac{(2n^2+2n-1)c^{2n+1}}{n(n+1)(2n+1)a^2}+\frac{(n^2+n-3)(2n+1)c^{2n-1}}{n(n+1)(2n+3)(2n-1)}$$

$$VD=3\frac{(n+2)(2n^2+1)a^{2n-1}-(n-1)(2n^2+4n+3)a^{-2n-3}c^{4n+2}}{2n+1}$$
$$+\frac{(n+2)(n-1)(2n+3)(2n-1)(2n^2+2n-1)c^{2n+1}}{(2n+1)a^2}$$
$$-\frac{(n^4+2n^3-n^2-2n+3)(2n+1)c^{2n+3}}{a^4}$$
$$-(n+2)(n-1)(n^2+n-3)(2n+1)c^{2n-1}$$

$$VE=(n^2+n-3)(2n+1)a^4c^{2n}+3(n+1)a^{2n+3}c$$
$$+3na^{-2n+1}c^{4n+3}-n(n+1)(2n+1)c^{2n+4}$$

APPENDIX B. LIST OF RSL SITES IN NORTH AMERICA

Latitude and longitude of RSL sites in North America that are used in the dissertation:

Latitude	Longitude	Site Name
55.00	-82.50	C. HENRIETTA MARIA
57.00	-77.00	RICHMOND GULF
53.00	-79.00	JAMES BAY, QUE.
58.00	-94.00	CHURCHILL, MAN.
64.50	-95.00	KEEWATIN, NWT
72.00	-80.00	MILNE INLET, BAF.
69.00	-82.00	IGLOOLIK IS.
69.00	-75.50	IPIK BAY BAF.
63.00	-70.00	C. TANFIELD
62.00	-75.00	UNGAVA PEN.
64.50	-84.00	SOUTHAMPTON IS.
59.80	-80.30	OTTAWA IS., NWT
53.00	-60.00	GOOSE BAY
51.50	-56.50	NW. NEWFOUNDLAND
47.00	-64.00	TIGNISH PEI
46.50	-63.50	FRENCH R. PEI
46.00	-60.00	CAPE BRETON IS., NS.
45.00	-65.00	BAY OF FUNDY
43.10	-70.70	ISLES OF SHOALS, NH.
42.80	-70.80	BOSTON, MA
41.20	-72.50	CLINTON, CT.
41.00	-74.00	NEW YORK

IMAGE EVALUATION TEST TARGET (QA-3)

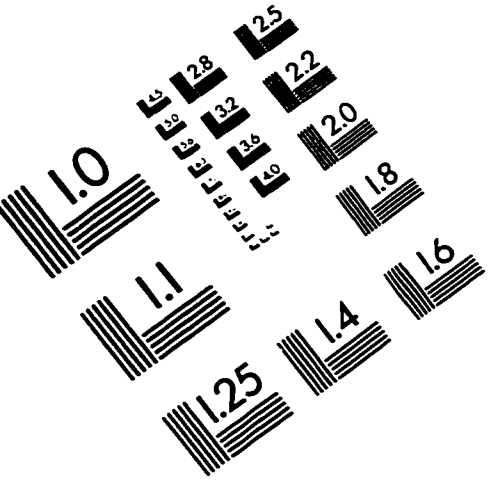

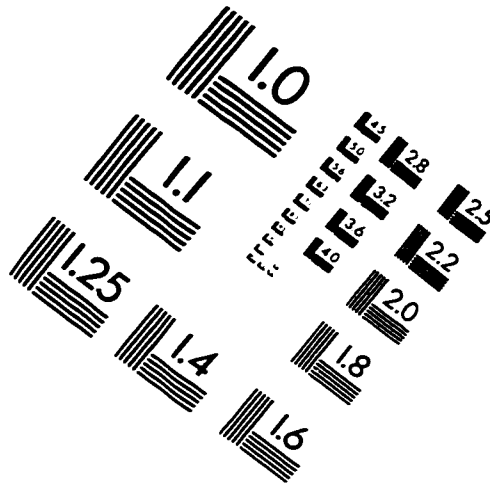

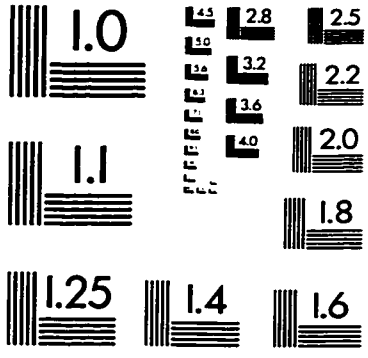

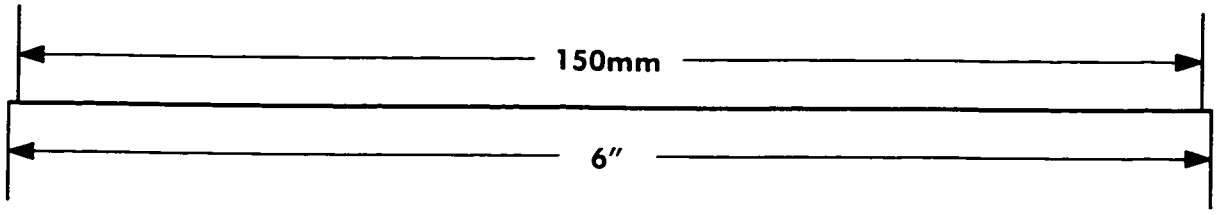

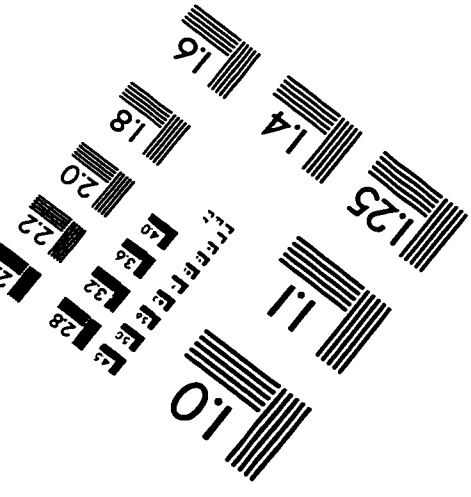

APPLIED IMAGE . Inc
1653 East Main Street
Rochester, NY 14609 USA
Phone: 716/482-0300
Fax: 716/288-5989